ANALYSIS OF VERTICAL VELOCITIES AND ELEVATED INSTABILITY IN THE COMMA-HEAD OF CONTINENTAL WINTER CYCLONES

BY

ANDREW ROSENOW

DISSERTATION

Submitted in partial fulfillment of the requirements
for the degree of Doctor of Philosophy in Atmospheric Sciences
in the Graduate College of the
University of Illinois at Urbana-Champaign, 2016

Urbana, Illinois

Doctoral Committee:

Professor Robert Rauber, Chair
Professor Greg McFarquhar
Associate Professor Stephen Nesbitt
Dr. Brian Jewett
Dr. Dave Leon, University of Wyoming

Abstract

The vertical motion and physical structure of elevated convection and generating cells within the comma heads of three continental winter cyclones are investigated using the Wyoming W-band Cloud Radar mounted on the NSF/NCAR C-130, supplemented by analyses from the Rapid Update Cycle model and WSR-88D data. The cyclones followed three distinct archetypical tracks and were typical of those producing winter weather in the Midwestern United States. In two of the cyclones, dry air in the middle and upper troposphere behind the Pacific cold front intruded over moist Gulf of Mexico air at lower altitudes within the comma head, separating the comma head into two zones. Elevated convection in the southern zone extended from the cold frontal surface to the tropopause. The stronger convective updrafts ranged from 2 to 7 m s^{-1} and downdrafts from -2 to -6 m s^{-1}. The horizontal scale of the convective cells was ~5 km. The poleward zone of the comma head was characterized by deep stratiform clouds topped by cloud top generating cells that reached the tropopause. Updrafts and downdrafts within the generating cells ranged from 1-2 m s^{-1}, with the horizontal scale of the cells ~1-2 km. Precipitation on the poleward side of the comma head conformed to a seeder-feeder process, the generating cells seeding the stratiform cloud, which was forced by synoptic scale ascent. In one case, shallow clouds behind the cyclone's cold front were also topped by cloud top generating cells, with vertical motions ranging from 1-2 m s^{-1}.

The development and distribution of potential instability in the elevated convective region of one of these cyclones is examined using a Weather Research and Forecasting (WRF) model simulation. The strong 8-9 December 2009 cyclone is simulated with a large outer domain and convection-allowing nest to simulate the convective region of the cyclone. The distribution of Most Unstable Convective Available Potential Energy (MUCAPE) is presented, with

MUCAPE values up to 93 J kg^{-1} produced in the simulation. The region with positive MUCAPE was based from 2-4 km altitude, located above an elevated frontal boundary as seen in the observations. Backwards trajectories were calculated in the convective region to show how potential instability formed. These trajectories showed that the potentially unstable layer consisted of five distinct layers, and that the air in the lowest layer, the source air for convective cells, originated near Baja California at low elevation, 5000 km away from the source region for air at the top of the potentially unstable layer, which originated in the Arctic at high altitude. Almost all of the trajectories in the potentially unstable region originated over the Pacific coast of Mexico, the Pacific Ocean, or the arctic regions of Canada. Notably absent in the potentially unstable layer was air originating over the Gulf of Mexico. Over the length of the trajectories, air consistently underwent radiational cooling, and was also affected by orographic forcing as it passed over mountains, mixed, and interacted with clouds and precipitation. Notably, no trajectory moved on isentropic surfaces. The constant changes in thermodynamic properties along trajectories also showed that it is the arrangement of airmasses in the comma-head that is responsible for the formation of potential instability, and not the initial thermodynamic properties of the air that eventually arrives at the comma head.

Acknowledgements

The author would like to acknowledge the vital efforts of staff at the National Center for Atmospheric Research Environmental Observing Laboratory, particularly Alan Schanot and the Research Aviation Facility staff for their efforts with the C-130 and the staff of the University of Wyoming King Air facility for their support of the WCR deployment, as well as thank Major Donald K. Carpenter and the U.S. Air Force Peoria National Guard for housing the C-130 during the Project. The composite radar analyses appearing in Figs. 2.5, 2.7, 2.15, 2.17, 2.22, 2.23, and 3.5 were provided by the Iowa Environmental Mesonet maintained by the Iowa State University Department of Agronomy. This work was funded under National Science Foundation Grants ATM-0833828 and AGS-1247404 to the University of Illinois and AGS-1247473 to the University of Wyoming. RUC data was provided by the National Climatic Data Center's NOMADS. The author acknowledges the Texas Advanced Computing Center (TACC) at The University of Texas at Austin for providing HPC resources that have contributed to the research results reported within this dissertation.

TABLE OF CONTENTS

Variables and Definitions for Chapter 2

Variable	Definition
θ_{ei}	Equivalent potential temperature with respect to ice
b_x, b_y, b_z	Unit vector components of radar beam
D	Maximum particle dimension
$\overline{D}$	Median reflectivity-weighted particle diameter
RH	Relative humidity with respect to liquid water
RH_i	Relative humidity with respect to ice
V_{Dop}	Radial velocity
V_T	Reflectivity weighted particle terminal velocity
v_x, v_y	Horizontal particle velocity components
W	Vertical total particle velocity
$\overline{W}$	Mean vertical total particle velocity
$\overline{w}$	Large scale vertical air motion
w'	Convective scale vertical air motion
Z_e	Equivalent radar reflectivity factor

1) Introduction

Severe winter weather has major impacts to life and property. Because of this, it has been an area of active study within the meteorological community. Large continental cyclones regularly impact the Midwestern US during the cold season, bringing with them snow, sleet, freezing rain, strong winds, and cold temperatures, including blizzard conditions within stronger storms.

The region northwest of the cyclone center, often referred to as the comma-head region, produces the heaviest snow and most severe winter weather in a cyclone due to the combination of heavy precipitation, cold air at the surface, and the tight surface pressure gradient driving strong winds (e.g. Rauber et al. 2014). Because of the importance of this region of the storm, the Profiling of Winter Storms (PLOWS) field campaign was carried out in 2009-2010 to understand precipitation substructures, instabilities, fronts, and microphysical processes in the comma-head. This field campaign collected a large amount of unique data in the comma-head region, making the dataset useful for studying the fine scale structures and dynamics of winter cyclones.

The work presented herein explores the structures of the comma-head region during major snowfall events, focusing on the forcing and structure of precipitation. The overarching goal of this work has two main components: the first to provide a better understanding of the distribution of vertical air velocities in the comma-head, and the second to provide a better understanding of the location, evolution, and development of elevated potential instability in the comma-head region.

Chapter 2 explores the vertical velocities observed in the comma-head region of three cyclones. Vertical air velocity is an important quantity directly affection precipitation

development. Specifically, this work seeks to identify regions of the comma-head with vertical air velocities of magnitudes exceeding 1 m s^{-1}, and to definitively show which precipitation structures are convective. The goal of this chapter is to establish the locations where convective cells of all spatial scales are located, quantify the magnitudes of the updrafts within convection, and place these vertical air motion measurements in the context of the comma head of the larger cyclone. In this chapter, a method of deriving vertical air motions will be presented. Then, the values of vertical air motions derived using this method will be shown using both case study and statistical approaches. The implications of these vertical motions on precipitation will be discussed.

The development of potential instability in the comma-head is explored in Chapter 3. The observation of convective air velocities in Chapter 2, combined with the presence of potential instability diagnosed by the operational Rapid Update Cycle (RUC) model, shows that deep convection occurs in the southern sector of the comma-head region. The goal of this section is to understand why potential instability is located in the comma-head location in a significant cyclone by ascertaining how this potential instability forms in space and time. Results from a high-resolution Weather Research and Forecasting model simulation are presented. Its performance, relative to the observed weather, is first evaluated to show that potential instability develops in the comma-head of the simulated storm. The simulation is then used to examine trajectories of air in the unstable region of the comma-head. The trajectories are used to understand the source regions of the potentially unstable air layer entering the comma-head. This study focuses on the role of diabatic processes in modifying air parcel properties on their transit to the comma-head region.

Chapter 4 will presents conclusions based on of the findings from both Chapter 2 and Chapter 3.

2) Vertical Velocities in the Comma-Head

2.1. Introduction

The comma head of wintertime cyclones is often associated with blizzards, heavy snow, and even occasional lightning (Rauber et al. 2014). Because of these hazards, the processes by which snow forms and develops within the comma head have been investigated for many years. Vertically pointing radar measurements from the 1950s consistently showed "generating cells" to be present at the top of otherwise stratiform warm frontal and comma head clouds of extratropical cyclones[1]. Marshall (1953) first reported that precipitation formed within these cells near cloud top at an altitude he termed the "generating level," and subsequently fell to the surface in virga-like slanted streaks. The cells formed above fronts (Douglas et al. 1957), were ~1 mile (1.6 km) in horizontal extent (Langleben 1956), had updrafts ranging from 0.75 to 3 m s^{-1} (Wexler and Atlas 1959, see also Carbone and Bohne 1975), produced streamers of precipitation that merged as they fell to produce the stratiform radar echo (Gunn et al. 1954), and were organized by shear into linear bands (Wexler 1955). Douglas et al. (1957) found that generating cells formed in a stable layer, as deduced from rawinsonde data, but hypothesized that latent heat release due to deposition could lead to the observed convection. Alternatively, Wexler and Atlas (1959) showed that lifting the moist-dry interface at the top of a stable cloud layer at a rate of less than 10 cm s^{-1} could trigger convection through release of potential instability, the favored location being the moist-dry interface ahead of an upper-level trough and west of the surface cyclone. The dry air source aloft was hypothesized to be the airmass of

[1] In this dissertation, the term "generating cell" is used to mean a small region of locally high reflectivity at cloud top from which a reflectivity trail characteristic of falling snow particles originates (American Meteorological Society 2013a).

This chapter has previously been published in the Journal of the Atmospheric Sciences (Rosenow et al. 2014, full citation in references section). Used with permission. Coauthors of that journal article contributed several ideas, figures, and portions of the text.

upper-tropospheric and lower-stratospheric origin behind the newly discovered (at the time) upper-level front (Reed and Sanders 1953, Reed 1955).

Vertically-pointing radar observations of generating cells at the tops of warm and occluded frontal clouds during the Cyclonic Extratropical Storms (CYCLES) program in the late 1970s and early 1980s largely support the early findings from the 1950s (e.g., Hobbs and Locatelli 1978, Herzegh and Hobbs 1980; Houze et al. 1981). Herzegh and Hobbs (1980) used vertically-pointing Doppler radar and found the strongest downdrafts to be of the order of -1 m s^{-1} and updrafts of 0.60 m s^{-1}. The existence of generating cells and their associated fall streaks from the top of clouds continued to be noted in more recent studies using vertically-pointing radars (e.g. Sienkiewicz et al. 1989, Syrett et al. 1995, Browning 2005, Cronce et al. 2007, Stark et al. 2013, Cunningham and Yuter 2013). The mechanism for precipitation formation in fall streaks accompanying the generating cells has been described as a seeder-feeder process (Bergeron 1950), with the seeder component being the ice particles falling from the cloud-top generating cells, and the feeder component being the moisture provided by larger-scale convergence (Browning 1983, Rutledge and Hobbs 1983).

Recent evidence from studies of cyclones suggests that stability varies across the northwest quadrant, from a conditionally-unstable environment on the equatorward side to a stable environment on the poleward side (e.g., Wiesmueller and Zubrick 1998, Martin 1998b, Nicosia and Grumm 1999, Novak et al. 2008, 2009). Novak et al. (2010), for example, showed that when east-coast cyclones are characterized by a dominant single band, the band forms as frontogenesis increases and conditional stability is reduced, and then dissipates as the opposite occurs. Conditional instability, when present, was most often found during the early period of band formation. Although conditional instability within the comma head of cyclones has been

observed with rawinsondes and calculated with models, details of the structure and vertical motions in resulting elevated convective cells have not been clearly established.

In this chapter, we investigate the detailed structure and vertical motion characteristics of cloud-top generating cells, stratiform clouds, and elevated convection and their relationship to frontal structure across the comma-head region of continental winter cyclones is investigated. This work is unique in that it presents the first statistical analyses of the distribution of vertical air motions across the comma head of three continental winter cyclones that followed distinct archetypical tracks (Zishka and Smith 1980). The first was a strong cyclone that propagated from eastern Colorado across the Midwestern United States and produced over 0.30-0.45 m of snow from the comma-head region as it passed over Iowa and Wisconsin. The second was a cyclone that originated near the Gulf of Mexico coast and propagated northward along the Mississippi and Ohio River Valleys, producing 25-30 mm of rain from the comma-head region as it crossed Illinois and Indiana. The third was an Alberta clipper-type cyclone (American Meteorological Society 2013b) that propagated southeastward from western Canada and produced 0.10-0.25 m of snow north of the low pressure center across southern Illinois and Indiana. Novel aspects of this study are that: 1) the data were obtained with an airborne W-band radar with extremely high resolution and sensitivity capable of resolving fine scale structures and circulations not resolvable in past work, 2) frontal structures determined from model initializations are directly related to fine-scale radar measurements made with airborne radar, 3) the *spatial* distribution of vertical motions relative to key meteorological features such as fronts are determined, 4) the statistical distribution of vertical motions between cloud top and the ground in stratiform and convective regions of the cyclones' comma heads are established, and 5) the vertical motions within the comma heads of each cyclone and the distribution of stratiform and convective

precipitation are interpreted in the context of the thermodynamic environment in which they are observed.

2.2. Instrumentation and methodology

The measurements reported here were made during the 2009-10 Profiling of Winter Storms (PLOWS) field campaign. A detailed description of PLOWS is included in Rauber et al. (2014). In this paper, data from the Wyoming Cloud Radar (WCR) aboard the NSF/NCAR C-130 aircraft are used.

2.2.1. University of Wyoming Cloud Radar

PLOWS was the first campaign to take advantage of a 10 dB improvement in the sensitivity of the WCR (Wang et al. 2012). The WCR was mounted on the rear ramp of the C-130 with two downward-looking beams, one at nadir, and one 34.3° aft of nadir. The single, upward-looking antenna was mounted ~7 m further forward in the aircraft. Widths of all three beams were < 1°. The sensitivity of the upward-looking beam was reduced by 6-8 dB compared with the downward-looking beam due to the longer waveguide run. The WCR outputs data at a rate of 20–25 profiles s^{-1} (corresponding to a horizontal scale of 4-7.5 m at the C-130 nominal airspeeds between 100-150 m s^{-1}). During PLOWS the WCR typically transmitted a 250 ns (37.5 m) pulse, sampled at 15 m resolution. The unambiguous range was 9 km, with 26.3 m s^{-1} unambiguous velocity. The aircraft roll, heading, and pitch angles and the ground-relative aircraft velocity were used to compute the orientation of the WCR beams in ground-relative coordinates, to identify and correct for the component of aircraft motion along each of the beams, and to determine the vertical component of the radial velocity from the upward- and downward-pointed beams. Leon et al. (2006) showed with a previous version of the WCR that, at

reflectivity greater than -10 dBZ, the variance in the vertical radial velocity was of the order of 0.04 m s^{-1}. With the more sensitive new version of the WCR used in PLOWS, the variance is much lower, on the order of 0.04 m s^{-1} at -23 dBZ.

2.2.2. Vertical radial velocity corrections

The horizontal wind field contributes to the total measured radial velocity values (V_{Dop}) according to

$$V_{Dop} = v_x \cdot b_x + v_y \cdot b_y + W \cdot b_z \ , \qquad (1)$$

where v_x, v_y, and W are the three-dimensional particle velocity components, and b_x, b_y, and b_z are the radar beam's directional unit vector components. This equation can be rearranged to obtain the vertical component of radial velocity, W, as

$$W = \frac{V_{Dop} - v_x \cdot b_x - v_y \cdot b_y}{b_z} \ . \ (2)$$

Because b_x and b_y are small for the upward- and downward-looking radar beams when the aircraft is in relatively level flight, an estimate of the horizontal wind field components, v_x, v_y, as a function of height from the initialization of the 20 km Rapid Update Cycle (RUC) model fields at the location of the aircraft was sufficient to derive W from the measured V_{Dop} and Eq. (2). For each radial velocity measurement, the horizontal wind field from the RUC and the radar beam's directional vector were used to derive W. The corrections to V_{Dop} using the RUC horizontal winds resulted in a change in W that was small, on the order of 0.10 m s^{-1} or less.

The equivalent radar reflectivity factor (Z_e, hereafter reflectivity) and W measurements were regridded from aircraft-relative to ground-relative coordinates. Profiles of equivalent

potential temperature (θ_{ei}) and relative humidity (RH_i), both derived with respect to ice, from RUC model initializations were then interpolated to the flight-track position and overlaid on the WCR data cross sections to give thermodynamic context to the radar measurements.

2.2.3. Vertical air motion estimation

The *W* measurements were analyzed using Contoured Frequency by Altitude Diagrams (CFADs; Yuter and Houze 1995). The variance of each *W* measurement and the surrounding eight data points was first calculated to filter noise, defined here as any point with variance > 0.75 m s^{-1}. The filtered *W* measurements were then binned both by velocity (0.2 m s^{-1} bin widths) and altitude (75 m bin widths). The fractional occurrence of each velocity within each height range was calculated for each velocity-height bin. CFADs were developed only across regions where the aircraft was established on a constant-altitude flight leg.

The goal in using the CFADs was to diagnose the magnitude and distribution of the vertical air motion in the sampled winter storms. The vertical particle motion, *W*, from radar consists of three components and is represented by

$$W = \overline{w} + w' - V_T \ , \qquad (3)$$

where $\overline{w}$ is the large-scale vertical air velocity, w' is the mesoscale- and convective-scale vertical air velocity, and V_T is the reflectivity-weighted terminal velocity of the ensemble of particles within a radar range gate. To interpret the CFADs in terms of w', estimates of V_T and $\overline{w}$ were independently derived.

2.2.3.1) Estimating V_T from W measurements

The statistical distribution of W from the WCR at a given altitude can be used to approximate V_T, provided that a flight leg is sufficiently long so that the magnitude and number of updrafts and downdrafts sampled are approximately equal. In this situation, the mean value of W at a given altitude, $\overline{W}$, should approximate V_T. The validity of this statement was tested using observations from the 14-15 February 2010 cyclone (described in section 3c). During this storm, the C-130 made thirteen horizontal flight legs at altitudes ranging from 2.8 to 7.6 km along a repeated flight track through a deep cloud system (Fig. 2.1).

First, a vertical profile of $\overline{W}$ for each pass in the vertical stack was calculated. A linear regression was performed on $\overline{W}$ with height for each profile. Next, the median reflectivity-weighted particle diameter, $\overline{D}$, from the ice particle size distributions for each constant altitude pass was calculated and a linear fit was performed, producing a $\overline{D}$–altitude relationship. Particle size distributions were obtained from the Two-Dimensional Cloud and Precipitation optical array probes for size ranges of $150 < D < 1600$ μm and $1600 < D < 9600$ μm respectively. The optical array data were processed to minimize errors due to shattering effects and other artifacts following the approach of Jackson et al. (2014). Knowing $\overline{W}$ versus altitude and $\overline{D}$ versus altitude, the relationship between $\overline{W}$ and $\overline{D}$ was calculated for each pass. These $\overline{W} - \overline{D}$ relationships are shown in red on Fig. 2.2. Superimposed on Fig. 2.2 in black are the V_T - D relationships for side planes (Locatelli and Hobbs 1974), stellar plates, plates, and columns (Davis 1974), small plates, plates, and dendrites (Kajikawa 1972), and capped columns, spatial dendrites, and plane dendrites (Brown 1970). The $\overline{W} - \overline{D}$ relationships derived from the 14-15 February 2010 cyclone lie within the range of some V_T-D relationships previously published, suggesting that the $\overline{W}$ profile can be used to approximate V_T, at least in stratiform regions. In

stronger convection, the production of particles with large V_T (e.g., graupel or hail) is correlated with the occurrence of stronger updrafts. In addition, passes through convection are short and it is less likely that the sampled distribution of updrafts and downdrafts balance. As a result, the $\overline{W}$ profile in convection might not adequately estimate the V_T profile, and the maximum observed W values will underestimate the true updraft strength. Thus, the estimation of V_T was only used for longer flight legs outside of elevated convective cells.

The CFADs presented in this paper are overlaid with cumulative distribution function values, so the 50% contour represents the median rather than the mean W profile. Velocity-diameter fits were also tested using the median, producing nearly identical results (not shown). Therefore, the median W contour on the CFADs was used to represent the particle ensemble V_T profile when the initial assumptions (lengthy flight legs outside of strong elevated convection) are valid.

2.2.3.2) Estimation of $\overline{w}$

Estimates of $\overline{w}$ were obtained from the RUC model. The model vertical velocity fields represent larger (meso-β) scale motion rather than the convective scale circulations detectable by the WCR. The one hour RUC forecast, valid at the time corresponding to each flight track segment considered, was used rather than the initialization to allow the model time to adequately develop the vertical motion field (Benjamin et al. 2010). Values of $\overline{w}$ were then interpolated directly to the flight track location.

2.3. Case studies

The three case studies presented are cyclones that originated from different geographic regions but impacted the Midwestern United States in winter. They were chosen because they represent different regions of cyclones' comma heads sampled during PLOWS. The 8-9 December 2009 case study describes measurements made within the comma head region directly north of the surface low-pressure center where dry air in the middle and upper troposphere behind the Pacific cold front intruded over moist Gulf of Mexico air at lower altitudes within the comma head. The 2-3 December 2009 case study focuses on measurements of the comma-head precipitation west of the surface low pressure center. The 14-15 February 2010 case study presents measurements made within deep clouds in the cyclone's comma head and in shallow clouds beneath the dry intrusion of air associated with the cyclone's dry slot.

2.3.1. 8-9 December 2009 cyclone

On 8 December 2009, a cyclone developed east of the Rockies in association with a strong short wave that deepened over eastern Colorado. The low-pressure center tracked from northeast New Mexico at 1800 UTC through central Missouri (0000 UTC, 9 December), northwest Illinois (0600 UTC), and southern Lake Michigan (1200 UTC). Aloft, a 500 hPa shortwave was located along the Kansas-Missouri border (Fig. 2.3a). Further aloft, a jet streak was present at 350 hPa over Arkansas at 0300 UTC (Fig. 2.3b), with the surface low-pressure center located under the jet streak's left-exit region. Strong upper-level forcing associated with the trough and jet streak caused the cyclone to strengthen from a sea-level pressure of 997 hPa at 1800 UTC 8 December to 979 hPa at 1200 UTC 9 December. The precipitation organized into a comma structure by 0000 UTC 9 December. Figure 2.4 shows a water vapor satellite image of the cyclone at 0332 UTC along with the surface frontal boundaries, sea-level pressure, the surface position of the 0°C isotherm, and 70% and 90% relative humidity contours at 500 hPa. Particular features which are

relevant to the analyses that follow are the cloud shield north of the low-pressure center and the dry-slot air east and north of the surface low-pressure center. Snow accumulations were approximately 0.30-0.45 m across Iowa, southern Wisconsin and Minnesota, and northern Illinois. The C-130 flight track from 0251-0351 UTC is shown on Figs. 4 (the straight red line) and 5 (the dark gray line). Figure 2.5 also shows the 0300 UTC mean sea-level pressure and 700-400 hPa thickness (approximating the thickness between the frontal surface and the tropopause across the study region) superimposed on the corresponding WSR-88D radar composite. The radar structure in the northern section of the comma head on Fig. 2.5 was characterized by linear bands nearly parallel to the thickness contours, and the southern section by cellular echoes.

Cross sections of Z_e and W from the WCR for the 0251-0351 UTC flight leg, overlaid with θ_{ei} and RH_i from the 0300 UTC RUC initialization, are shown in Fig. 2.6. The lower panel in Fig. 2.6 shows $\overline{w}$ from the RUC one-hour forecast valid at 0300 UTC. A broader perspective of the frontal structure relative to the stratiform and convective regions can be seen in Fig. 2.7, which extends the cross section over a distance of 1500 km, illustrated by the white line on Fig. 2.4 and in the inset in Fig. 2.7. The surface Pacific cold front appearing on Fig. 2.4 from Texas to Tennessee corresponds to the dry slot boundary at higher elevations. However, north of the warm front, the Pacific cold front can only be found aloft, where the dry air behind the front intrudes over warm, moist air. The Pacific cold front aloft corresponds to the southern boundary of the deeper cloud shield and wraps back to the west across Iowa, marking the leading edge of the dry slot boundary. This front appears on Figs. 2.6 and 2.7, the boundary between dry Pacific air aloft and moist Gulf air below. An arctic front is also present at low altitudes.

The character of the radar echoes changes near the midpoint of the cross section, at ~0315 UTC. To the north, the echoes appear stratiform below 7 km. They are topped with generating

cells between 7 and 9 km. These generating cells were ubiquitous in the PLOWS dataset in both the cases examined here as well as cases not shown. To the south, elevated convective cells with updrafts ranging from 1-7 m s^{-1} are evident extending from the top of the frontal surface to the tropopause. The boundary between these two regions was sharp, but was not characterized by a distinct thermal gradient. Grim et al. (2007) examined similar boundaries in two cyclones and found that one was characterized by a thermal gradient, while the other was similar to this cyclone with only a moisture gradient. For convenience here, the north side of the cross section is referred to as the "stratiform region" and the south side as the "convective region", although the stratiform region contains convective elements near cloud top.

The moist stable layer below the front decreased in depth from 6 to 3 km from north to south across Fig. 2.6. In the stratiform region, air above the front had near neutral stability (Fig. 2.6a). Large-scale ascent both above and below the front occurred in this region (Fig 6c). In the convective region, air above the front was conditionally unstable and descending on the large scale as part of the dry-air intrusion south of the comma head. The environmental convective available potential energy (CAPE) associated with these cells was 50-250 J kg^{-1} (see Rauber et al. 2014). The large-scale vertical motion cross section in Fig. 2.6c appears to show a frontal circulation with the ascending and descending branches in locations relative to the deep echoes that are consistent with the frontogenesis calculations of Han et al. (2007) for strong continental cyclones. Except for part of the convective region, the entire area with reflectivity measured by the WCR was supersaturated with respect to ice (Fig. 2.6a). In the analyses below, the stratiform and convective regions are considered separately since the stability and character of the echoes were distinct in the two regions.

2.3.1.1.) Stratiform Region

In the stratiform region, convective generating cells were ubiquitous atop the deep, otherwise stable cloud layer. The generating cells were confined to the air mass above the frontal boundary and originated ~2 km above the front, between 7.0 and 9.5 km altitude. The temperatures at the generating-cell level ranged from -32°C at the base of the generating cells to -51°C at their tops. Ice particle fall streaks were evident originating within the generating cells and merging together within the stable layer below the front. A close up view of the Z_e and W fields using a 1:1 aspect ratio (Fig. 2.8) clearly differentiates the stable lower portion of the cloud from the generating cells. This perspective shows that the cloud-top convection has similar horizontal and vertical scales. Although irregularities appear in their structure and spacing, the generating cells are approximately 1-2 km deep and 0.5-1.5 km wide.

Fourier analysis was used to better quantify the horizontal scale of the generating cells. Five minute time series of Z_e measurements at constant altitudes within the generating cells were randomly selected, smoothed vertically over three data points (45 m) to reduce noise, and processed to remove any linear trend. A Fast Fourier Transform identified the spectrum of frequencies present within each time series, with corresponding wavelengths derived using the average C-130 airspeed over the same time periods. These spectra were smoothed to identify dominant wavelengths. Figure 2.9 shows histograms of horizontal wavelength peaks identified from 1000 random time series. A persistent signal emerges with dominant wavelengths (updraft/downdraft couplets) between 1 and 3 km, corresponding to generating cells with horizontal dimensions of 0.5 to 1.5 km.

Figure 2.8b shows W within individual generating cells. Values of W of 1-2 m s^{-1} appear in the center of the cells with negative values of similar magnitudes along the edges. The mesoscale and convective vertical air motions (w') were determined by analyzing the CFAD of W within

area (*i*) between the dashed lines on Fig. 2.6, shown as Fig. 2.10. On the CFAD, the frequency distribution of W (in color shading) is overlaid with contours showing the cumulative distribution function for each height bin. The value of $\overline{w}$ at the generating-cell level of ~8 km from Fig. 2.6c (~0.2 m s^{-1}) and the value of V_T, estimated from the 50% contour on the CFAD (~0.25 m s^{-1}) approximately cancel. Therefore, from Eq. 3, $W \approx w'$ and the CFAD in the generating cell region can be used as a measure of the updraft and downdraft structure. The range of w' increases from ±1 m s^{-1} at the base of the generating cells (~7 km) to ±2 m s^{-1} at echo top (~9.5 km). Approximately 20% of w' values exceeded ±1 m s^{-1} in the top 1 km of the generating cells.

The median W (approximately representing $-V_T$) below the generating cells decreases from -0.25 m s^{-1} at 7 km to -1 m s^{-1} near the surface, consistent with an increase in terminal velocity with ice particle size as ice particles grow through diffusion and aggregation with depth in the cloud. The value of $\overline{w}$ in this region was approximately 0.2 m s^{-1}. Below the front (under ~5.5 km), 90% of all W values were within -0.2 to -1 m s^{-1}, consistent with the range of terminal velocities expected for a spectrum of falling ice particles.

The structure within the stratiform region conforms to a seeder-feeder mechanism (Bergeron 1950). The stronger vertical motions within the generating cells triggered ice nucleation and the large-scale ascent below provided the moisture for continued particle growth.

2.3.1.2.) Convective Region

Discrete elevated cellular convection was present in the convective region (Fig. 2.6). A sounding taken near the time the C-130 passed near the rawinsonde launch site (yellow dot in Fig. 2.4) had 241 J kg^{-1} of CAPE calculated for parcel ascent from just above the top of the front

at about 3.5 km. The CAPE developed as low θ_{ei} air within the cyclone's dry slot advanced over the moist Gulf airmass. To illustrate this, Fig. 2.4 shows two example air parcel back trajectories calculated using the HYSPLIT model (Draxler and Hess 1998**,** Grim et al. 2007) from starting positions on the C-130 cross section (Fig. 2.6) at two locations, one in the dry-slot air above the front (blue dot) and the other in the moist air near the top of the front (red dot). These trajectories are representative of a family of trajectories that were calculated at various points on the cross section within the dry and moist airmasses. The trajectory in the dry-slot airmass originated over the Pacific at an altitude of approximately 5 km, descended slowly until about 12 hours before the time of the cross section and then rose over the front to an altitude of 7 km. The trajectory near the top of the front originated at the surface over the Gulf of Mexico and ascended to approximately 3 km.

Figure 2.11 shows Z_e and W profiles at 1:1 aspect ratio for one of the cells in region (*ii*) of Fig. 2.5, showing convection on horizontal and vertical scales of ~5 kilometers. Upward W values of 7 m s^{-1} were present from 3.5-7.0 km in the cell's core, with negative values of -4 to -5 m s^{-1} present at the cell's periphery and near echo top. The convection was clearly elevated, based above the frontal boundary and extending to the tropopause. Upward W values of 5 m s^{-1} or more were common above the front in cells sampled on the aircraft pass shown in Fig. 2.5, in subsequent passes, and in ground-based profiler measurements across the broader convective region (see Figs. 5-7 in Rauber et al. 2014). Several cells in the vicinity produced lightning discharges (Rauber et al. 2014).

Figure 2.12a shows the CFAD of W for the convective cell in region (*ii*) of Fig. 2.6. As discussed in Section 2, the median W profile does not adequately estimate the V_T profile in stronger convection above the front. Since Eq. 3 cannot be used to ascertain w' from W, the W

profile will be discussed here. Since V_T is included in *W*, updraft velocity magnitudes will be larger and the downdraft velocity magnitudes smaller than the measured *W*. Within the cell, *W* values increase from just above the front (~3 km) to 6 km, reaching maximum values in excess of 5 m s^{-1}. At the level of maximum upward *W* values, 10% of the *W* measurements exceeded 4 m s^{-1} and 25% exceeded 1 m s^{-1}. Downward *W* values were weaker, with 25% of the measurements between -2 and -3 m s^{-1}, except at cloud top where 10% of the observations ranged from -3 to -6 m s^{-1}. Figure 2.12b shows another CFAD for the convective cell in region (*iii*) on Fig. 2.6. Above the front, maximum upward *W* values again were around 6 km with 10% of the observations ranging from 2 to 4 m s^{-1}. Downward *W* values were maximized near and below the front with 10% of the observations ranging from -2 to -4 m s^{-1} between 2 and 4 km, and a slight increase in downdrafts was also noted near cloud top between 6 and 7 km. The range of *W* was smaller compared to the first convective cell, but was consistent with the convective appearance of the echoes.

The region below the front, located at 3 km, was non-convective and can therefore be interpreted using Eq. 3. Median *W* values range from -1.5 to -1.0 m s^{-1} in the lowest 2 km, the approximate fall velocity of large aggregates or small graupel. The value of $\overline{w}$ was approximately 0.1 m s^{-1} (Fig. 2.6c). Below the front at about 3 km, the majority of *W* measurements were within 0.75 m s^{-1} of the median, consistent with the spread of terminal velocities expected for a spectrum of ice particles ranging from small ice crystals to aggregates and small graupel. The data below the front on Figs. 12a,b suggest that particles were falling at or near their terminal velocities in the absence of any strong w'.

2.3.2. 2-3 December 2009 cyclone

The 2-3 December 2009 cyclone formed along the Gulf Coast as an upper-level cutoff low over Baja California became an open wave and moved over the southern United States (Fig. 2.13a). The cyclone reached the Ohio-Indiana-Kentucky junction by 0000 UTC 3 December and Lake Erie by 0600 UTC, strengthening from 1001 hPa to 992 hPa. Figure 2.13b shows a 350 hPa jet streak at 0000 UTC with its left-exit region over the surface cyclone. Figure 2.14 shows a water vapor image of the cyclone at 2340 UTC on 3 December. The comma head of the cyclone extended across the Great Lakes and southward into Mississippi. A key feature of importance to the analyses below is the upper level front and associated dry air aloft that can be seen wrapping into the cyclone circulation south of the comma head into southern Indiana. The 0000 UTC WSR-88D reflectivity composite in Fig. 2.15 shows precipitation in the comma head extending from the Great Lakes to Arkansas. Surface temperatures were above freezing throughout much of the study region in Illinois and Indiana, with storm-total rainfall amounts of up to 25-30 mm. For this event, the C-130 flew across the eastern side of the comma head, as noted by the flight track in Figs. 14 (red line) and 15 (white line).

A WCR cross section of Z_e from ~0024-0043 UTC overlaid with θ_{ei} and RH_i is shown in Fig. 2.16a. Similarities to the 9 December case are evident. Figure 2.17 illustrates the synoptic-scale extent of the air masses and frontal structure relative to Fig. 2.16. The surface cold front extends from Kentucky to the Gulf of Mexico (Fig. 2.14). The Pacific cold front aloft, marked by the leading edge of the dry slot, in this case was east of the surface cold front (off the right side of the cross section in Fig. 2.17), but wrapped northward across Ohio and southward across Indiana. The position of the front is shown separating moist Gulf air from dry air aloft on Fig. 2.17. Focusing more closely on Fig. 2.16, an ice-saturated stratiform region with stable air below the Pacific front and stable to near neutral air above the front was present through much of the

profile, with the frontal boundary at ~4.5 to ~6.5 km. Deep clouds extending to the tropopause were present in this region, with the radar echoes stratiform in nature except for generating cells present at cloud top. In the convective region further southeast, lower θ_{ei} air was present above the front. Discrete elevated convective cells, based above the frontal boundary, were consistently observed in this region. These regions are considered separately below.

2.3.2.1) Stratiform region

Generating cells were consistently present atop this region, producing ice particle fall streaks that merged in the layer below (Fig. 2.16a). The generating cells were based at ~8 km, ~1.5 km above the frontal boundary, and extended to ~9 km. The temperature at the base of the generating-cell level was -36°C and the tops of the generating cells were located at -46°C. Fourier analysis (not shown) identified the largest peak in horizontal wavelength for Z_e just below 1 km, with additional peaks around 0.5, 1, and 2 km. These are similar wavelengths to the 9 December case.

The W cross section in Fig. 2.16b shows that the largest values (up to ±2 m s^{-1}) were confined to the generating cells. No obvious fine scale vertical circulations beyond the synoptic scale rising motion (Fig. 2.16c) were present through the deeper cloud below. Figure 2.18 shows a CFAD for the stratiform region, corresponding to area (*i*) in Fig. 2.16. Above the front, $\overline{w}$ is ~0.20 m s^{-1} (Fig. 2.16c) and V_T increases with depth from 0.25 m s^{-1} at echo top to 1 m s^{-1} near the front. Accounting for $\overline{w}$ and V_T, w' is greater than W by about 0.25-0.50 m s^{-1} in the generating cells between 8 and 9.5 km, with maximum w' values of ~1.5 m s^{-1} down and ~2.5 m s^{-1} up. About 20% of the measurements in the generating cells are updrafts and downdrafts where w' exceeds ±1 m s^{-1}.

Below the generating cells but above the front, 90% of W values were within 0.5 m s^{-1} of V_T (0.75-1.25 m s^{-1}), typical of fall velocities of ice crystals and aggregates in the low density air at that altitude. Below the front, $\overline{w}$ was about 0.15 m s^{-1} (Fig. 2.16c). V_T gradually increased from 1.25 m s^{-1} near the front to 1.5 m s^{-1} at the melting layer (~2 km), then increased to 4 m s^{-1} near the surface. 80% of W measurements were within 0.5 m s^{-1} of V_T, again indicating small w' values below the generating-cell level.

2.3.2.2) Convective region

Discrete elevated convection again formed within the dry air intrusion associated with the advance of the cyclone's dry slot air over the front. The convection was based near the top of the moist air just below the frontal boundary, which was located between 3 and 4 km (Fig. 2.16a) with echo tops near 8 km. This region was sampled repeatedly by the aircraft. Two passes with the least turbulence-induced velocity contamination, both at a later time than in Fig. 2.16, are shown at 1:1 scale in Figs. 19a-d. Although these data show similar structures, due to the time between passes they are not necessarily the same convective cell. The 1:1 Z_e profiles (Figs. 19a,b**)** show a scale of ~5 km for the convection. The strongest vertical motions, with W values of ~±4 m s^{-1} (Fig. 2.19c,d), are co-located with the highest Z_e values above the frontal layer. Unfortunately, all of the project soundings for this case were taken in the stratiform region so elevated CAPE values for the region where the convection was observed with the WCR could not be obtained. Back trajectories of air parcels that arrived on the cross section above and below the front in the vicinity of the dry intrusion showed similar behavior to the previous cyclone (Fig. 2.14). The dry air trajectory started over the Pacific Ocean and descended from near 10 km to 5.5 km, and then ascended to 7 km in the last few hours before arriving at the cross section. Moist air near the top of the front ascended from approximately 1 km over the Gulf of Mexico to an

altitude of 3 km at the cross section. As with the previous cyclone, the intrusion of low θ_{ei} air over the front created potential instability.

Figures 2.19e,f shows CFADs of *W* for the two convective cells. Above the front at 4 to 5 km, both CFADs exhibit broad *W* distributions. Downward *W* values dominate the earlier pass (Fig. 2.19e) with around 25% of values at or below -2 m s^{-1}. Only 5-10% of *W* values above 5 km have values at or above 1 m s^{-1}. For the second pass (Fig. 2.19f**)**, more updrafts were sampled. The maximum *W* values were found in the layer between 4.5 and 6.5 km, where 10 % of *W* values were at or above 2 m s^{-1}. Fewer large downward *W* values were sampled, with only 10-15% of measurements at or below -1 m s^{-1}.

In the non-convective moist layer below the front, the median *W* profile represents V_T. Values of V_T are ~1.5 m s^{-1} in Fig. 2.19e and ~1 m s^{-1} in Fig. 2.19f above the melting layer at 1 km, increasing to ~4 m s^{-1} at ground level. These values are reasonable fall speeds for aggregates or small graupel melting into raindrops. Values of $\overline{w}$ were around 0.1 m s^{-1} below the front (Fig. 2.16c). In addition, the majority of *W* measurements were within 0.75 m s^{-1} of the median, which is consistent with the spread of terminal velocities expected for a spectrum of ice particles or raindrop sizes.

2.3.3. 14-15 February 2010 cyclone

On 14-15 February 2010, an Alberta-clipper type cyclone moved over the western Ohio River Valley in association with a shortwave that originated east of the Canadian Rockies and propagated into the Midwestern United States (Fig. 2.20a). The low-pressure center moved from southeast Missouri (1200 UTC 14 February) to southern Indiana (0000 UTC 15 February) and eastern Kentucky (1200 UTC), while deepening from 1012 hPa to 1006 hPa. A jet streak at 350

hPa was present with its left-exit region over the surface cyclone at 0600 UTC (Fig. 2.20b). As the cyclone progressed, its comma head and dry slot passed across the operations area in southern Indiana (Fig. 2.21). The 0600 UTC WSR-88D reflectivity composite in Fig. 2.22 shows the precipitation associated with the cyclone. The C-130 made repeated passes between two navigational points across southern Indiana directly north of the surface cyclone as the cyclone moved across the area. This position in the comma head was substantially different from the previous two cyclones which had extensive precipitation shields extending west of the surface cyclones. The flight track is indicated by the red line in Fig. 2.21 and the white line in Fig. 2.22. Snowfall amounts were between 0.10-0.25 m on 14-15 February across the operations area, with locally higher amounts.

Figure 2.23 shows an extended cross section along the flight path to illustrate the relationship between the flight data and the fronts (see white line on Fig. 2.21 and the inset in Fig. 2.23 for cross section location). The cross section extends along a line north of the surface low-pressure center. On this cross-section, a warm front appears to the east of the low pressure center position, and a cold front to the west. In the area of the deeper clouds measured by the WCR, the cold front extended to an altitude of approximately 2 km. To the west where shallow clouds were present, the cold front extended to the tropopause. A region of stable to near neutral air extends to the tropopause above the warm front and east of the cold front. The deeper comma-head clouds were sampled during an early pass of the aircraft. Later, as the cyclone moved eastward, shallow clouds behind the cold front were sampled along the same flight path. These two regions are discussed separately below.

2.3.3.1) Deep Clouds

Figure 2.24 shows cross sections of Z_e and W for the 0515-0542 UTC flight leg overlaid with θ_{ei} and RH_i. Nearly the entire region was supersaturated with respect to ice. Generating cells were ubiquitous, and produced ice particle fall streaks that merged in the stable layer below. The cells were located between 6.5 and 8 km altitude, were 1-1.5 km deep, and Fourier analysis (not shown) identified horizontal wavelength peaks between 0.5 and 3 km, consistent with the range of values from the other two cases. The temperatures at the generating-cell level ranged from -39°C at their base to -54°C at their tops.

The W cross section in Fig. 2.24b shows values to ±2 m s^{-1} in the generating cells, with more uniform values near -1 m s^{-1} below. Figure 2.25 shows a CFAD for the entire cross section in Fig. 2.24. Values of V_T increase from 0.25 m s^{-1} at cloud top to 0.75 m s^{-1} at ~5.5 km altitude. Above 5.5 km, $\overline{w}$ is ~0.20 m s^{-1} (Fig. 2.24c). Because $\overline{w} \approx V_T$ in the generating cells, W approximates w'. Approximately 20% of w' values exceed ±1 m s^{-1} at cloud top.

Below the generating cells but above the front, about 80% of W values are within ±0.5 m s^{-1} of V_T (0.5 m s^{-1}), consistent with the expected spectra of particle fall velocities. Below the front, V_T increased from 0.75 m s^{-1} near the front to 1.25 m s^{-1} at the surface, with $\overline{w} \approx 0.10$ m s^{-1} (Fig. 2.24c). Below the front, 80-90% of W values were within 0.5 m s^{-1} of V_T.

2.3.3.2) Shallow Clouds

Figure 2.26 shows Z_e and W profiles within the shallow clouds behind the cold front for the 1031-1059 UTC flight leg (same location as Fig. 2.24, but later in time), overlaid with θ_{ei} and RH_i. In the case of the Alberta-clipper storm, no elevated convection was observed. Near cloud top, 1-1.5 km deep generating cells were consistently present, originating near 3 km, and

extending over a temperature range of -21°C to -29°C. Fourier analysis (not shown) of the generating cells in this region identified horizontal wavelength peaks between 0.5 and 1.5 km. These wavelengths are shorter than those atop the deeper clouds in this case as well as the previous two cases presented in previous sections.

The organization of the echoes and the velocity distribution was similar (though shallower) to that of the deeper clouds. Maximum W values in the generating cells were ±2 m s^{-1}, and values below the cells were approximately -1 m s^{-1} (Fig. 2.26b). Figure 2.27 shows a CFAD for the cross section in Fig. 2.26. V_T increased from 0.1 m s^{-1} near echo top to 1.25 m s^{-1} near the surface. With $\overline{w} \approx 0.05$ m s^{-1} at the generating cell level (Fig. 2.26c), V_T is greater than $\overline{w}$ by 0.05-0.75 m s^{-1}. Therefore, ~20% of w' values here exceed ±1 m s^{-1}. Below the generating cells, ~75% of the W values were within 0.5 m s^{-1} of V_T.

2.4. Summary

This chapter presented analyses of the vertical air motion and physical structure of cloud-top generating cells, elevated convection, and stratiform clouds within the comma head region of continental winter cyclones and their relationship to fronts. The cyclones were typical of those producing winter weather in the Midwestern United States. One cyclone originated east of the Colorado Rocky Mountains and tracked eastward across the Midwest, producing a major winter snowstorm across Iowa and Wisconsin. The second cyclone formed along the Gulf of Mexico and tracked north and eastward along the Mississippi and Ohio River Valleys. The surface temperatures in this cyclone were warmer, and the storm produced mostly rain at the surface beneath the comma head. The third Alberta-clipper type cyclone originated east of the Canadian Rockies and produced a moderate snowstorm across Illinois and Indiana. The analyses, from the

PLOWS field campaign, were based on data from the Wyoming Cloud Radar (WCR), project soundings, and microphysics probes on the NSF/NCAR C-130 aircraft. This work is the first to relate frontal structures determined from model initializations directly to fine-scale radar measurements made with airborne radar. The PLOWS data were supplemented by analyses from satellite data, trajectory calculations from the HYSPLIT model, and WSR-88D radar data.

This chapter illustrates the relationship between frontal structures and the distribution of precipitation across the comma head of continental winter cyclones. Within the comma head of two of the cyclones, drier air behind the wrapped-back Pacific cold front aloft moved over moist air originating over the Gulf of Mexico. Upright elevated convection and generating cells at the top of deeper stratiform clouds both developed within this airmass. In both cases, Arctic air was present near the surface beneath the comma head. In the Alberta clipper storm, the comma head was sampled directly north of the low pressure center and ahead of the cold front. This case did not involve overrunning of dry air. Nevertheless, cloud-top generating cells were ubiquitous in this storm.

This chapter quantifies the distribution of vertical velocities in and near cloud-top generating cells. A key finding of was the ubiquitous nature of cloud-top generating cells in the stratiform regions of the comma head of winter storms. The deep stratiform regions of the comma heads of all three cyclones were everywhere topped with 1-2 km deep generating cells. Even shallow clouds behind a cold front sampled in one case were topped by generating cells. The base of the generating cells atop the deeper clouds ranged from -32°C to -40°C, while the tops ranged from -46°C to -54°C. The layer in which the generating cells occurred appeared to be near moist-neutral with respect to ice processes based on RUC analyses of the thermodynamic structure. Vertical motions (both updrafts and downdrafts) within the generating cells, determined from

CFAD statistical analyses across the generating cell regions, ranged from 1-2 m s^{-1}. The horizontal scale of the generating cells was ~1-2 km. The generating cells atop the shallow clouds occurred at warmer temperatures of -22°C to -29°C and had a slightly smaller horizontal scale of 0.5-1.5 km, but similar vertical motions to the generating cells atop the deeper clouds. Below the generating cell level in the stratiform region, air was stable based upon soundings and the distribution of θ_{ei} from the RUC analyses. The distribution of W below the generating cell level measured by the WCR, based on CFAD analyses across the stratiform regions of all three cyclones, were of the same magnitude as that expected for a distribution of hydrometeors falling at their terminal velocities, suggesting that any vertical air motion in this region was weak, consistent with the slow large-scale ascent (e.g. 0.1-0.2 m s^{-1}) noted in the RUC analyses. The precipitation in the stratiform region appeared to conform to a seeder-feeder process, as first hypothesized by Bergeron (1950), the seeder being the observed fall streaks of ice crystals generated by each of the cloud top generating cells, and the feeder being the moisture provided by the large scale ascent at lower altitudes within the comma head that would support continued ice particle growth. Vertical air motion magnitudes in the generating cells agree with the more limited past observations from Wexler and Atlas (1959) and Carbone and Bohne (1975), but were slightly larger than those found by Herzegh and Hobbs (1980).

A second major finding of this study was the presence of elevated convection on the equatorward side of the comma head where dry air associated with the cyclones' dry slot overran moist air below the wrapped-back cold front aloft. This process occurred in the cyclones originating east of the Colorado Rockies and along the Gulf of Mexico, but not in the colder Alberta clipper cyclone. In the two cases where elevated convection was present, the dry air was characterized by lower values of θ_{ei} relative to air just below the frontal surface, leading to the

development of potential instability. In both cases, based on trajectory analysis, the moist air below and near the wrapped-back cold front aloft originated near the surface over the Gulf of Mexico, while the dry air further aloft originated between 5 and 10 km altitude over the Pacific Ocean. Elevated convection extended from just below the cold frontal boundary to the tropopause in both cases. The bases of this elevated convection in the two cases ranged from 3-4 km, while the tops ranged from 7-9 km. Both updrafts and downdrafts were observed. Based on CFAD statistical analyses, the stronger updrafts ranged from 2 to 7 m s^{-1} and the stronger downdrafts ranged from -2 to -6 m s^{-1}. The horizontal scale of the convective cells was roughly 5 km in both cases. In a companion paper, Rauber et al. (2014) showed that some of the convective cells in PLOWS cyclones occasionally produced cloud-to-ground and cloud-to-cloud lightning, and contained supercooled water and graupel between -10°C and -20°C, consistent with non-inductive charging.

The present findings show that cloud-top generating cells and elevated convection are key elements contributing to the mesoscale structure of the comma head region of continental winter cyclones. The importance of generating cells and elevated convection in snow generation in continental winter cyclones clarifies findings of a half-century past, when pioneering scientists of the 1950s first turned their radars skyward, and observed the phenomena explored here with modern instrumentation.

2.5. Figures

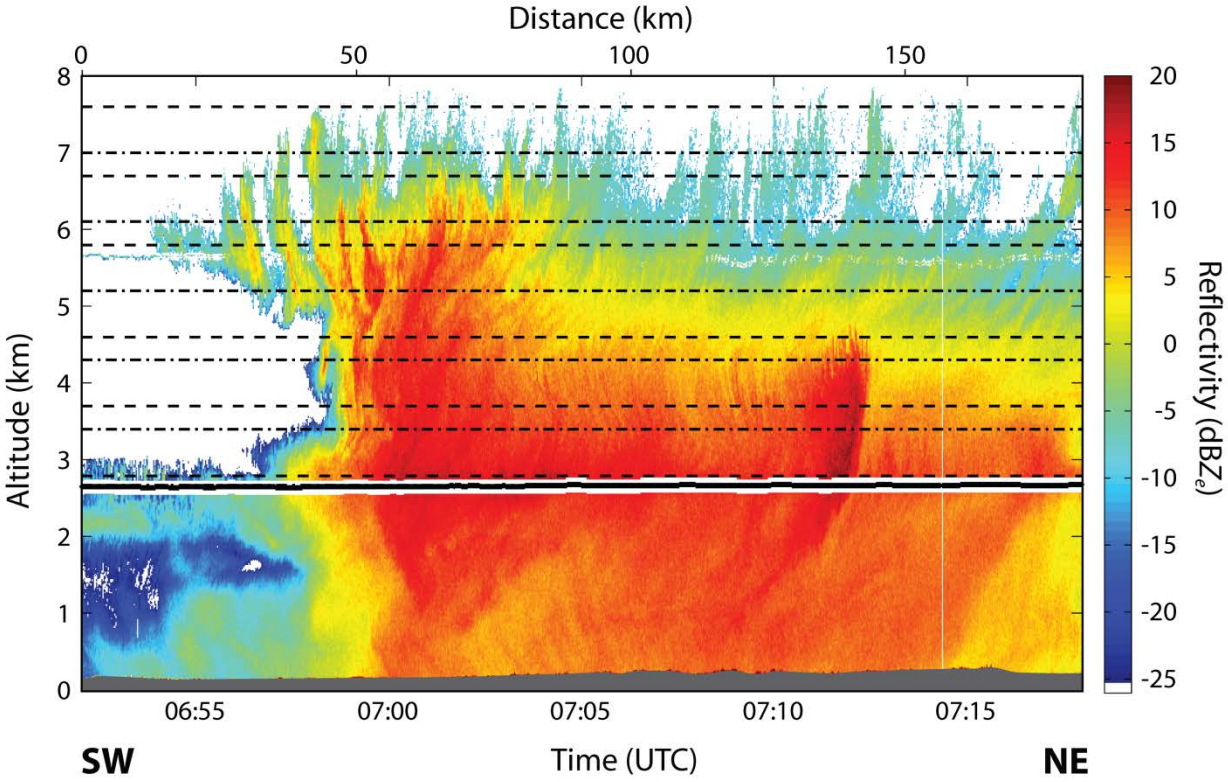

Figure 2.1: Z_e from the WCR from 0651-0718 UTC 15 February 2010. The solid black line indicates the flight track corresponding to the radar data. Dashed lines indicate altitudes of other aircraft passes along the same flight track between 0350-0720 UTC, and dash-dot lines indicate passes between 0740-1100 UTC. The radar depictions were different for these flight legs since the weather system evolved over the course of the flight. The linear echo near 5.7 km is the ground reflection detected by the WCR.

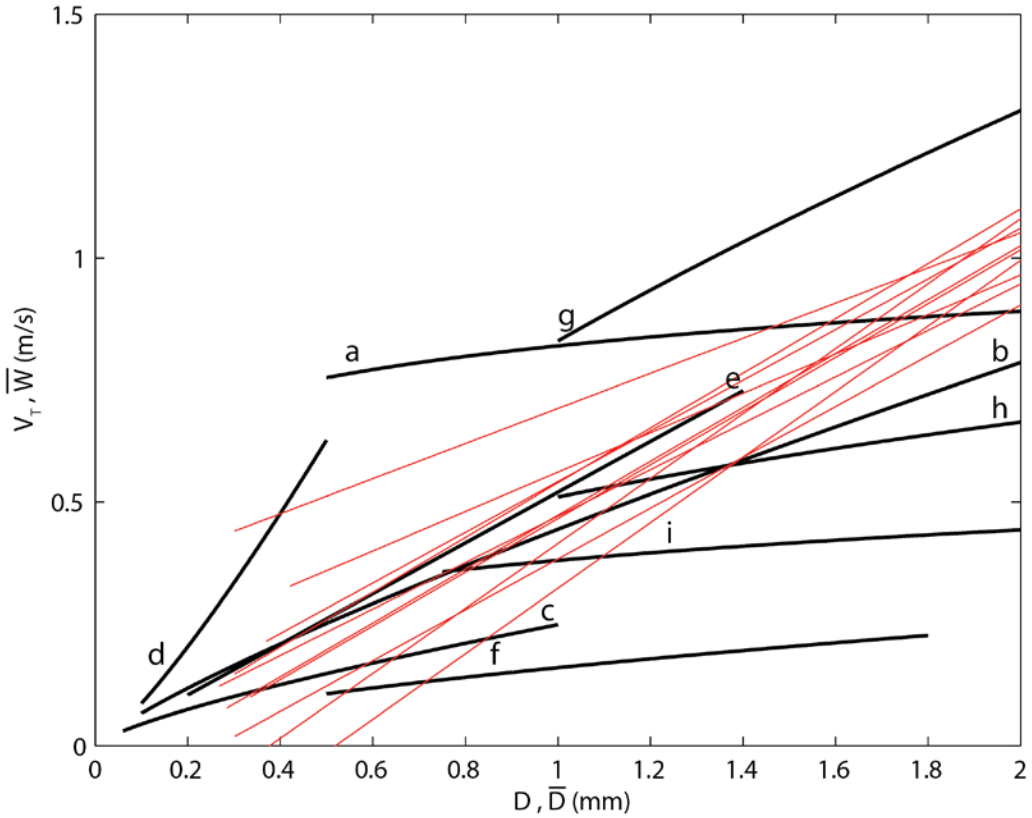

Figure 2.2: WCR-derived $\overline{W}$ - $\overline{D}$ relationships (red) and V_T-D relationships from the literature in black. The V_T-D relationships are from: Locatelli and Hobbs (1974) side planes (a); Davis (1974) plates (b), branched plates (c); Kajikawa (1972) small plates (d), plates (e), dendrites (f); and Brown (1970) columns (g), spatial dendrites (h), and plane dendrites (i).

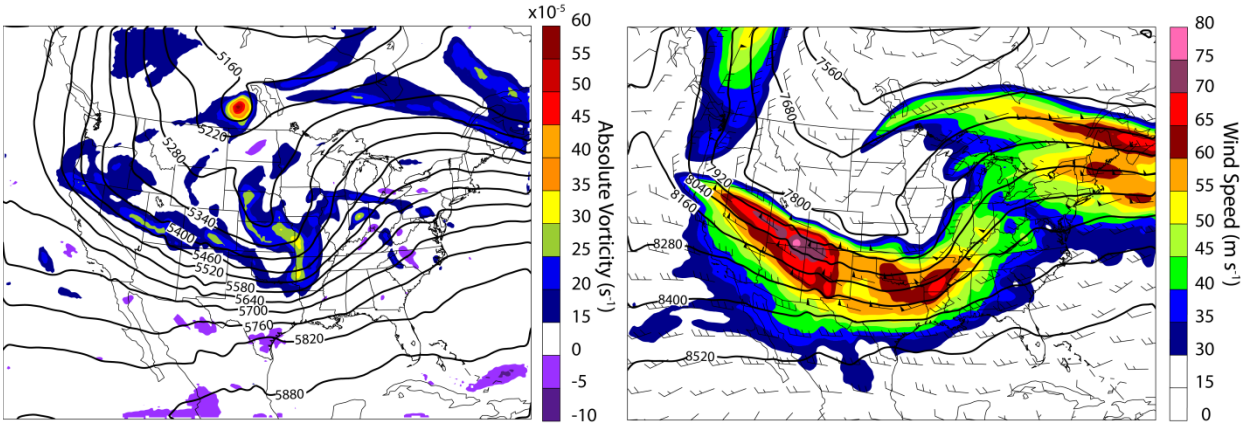

Figure 2.3: RUC analysis of (a) 500 hPa geopotential height (contours) and absolute vorticity (s^{-1}, shaded), (b) 350 hPa geopotential height (contours) and wind speed (m s^{-1}, shaded), valid 0300 UTC 9 December 2009.

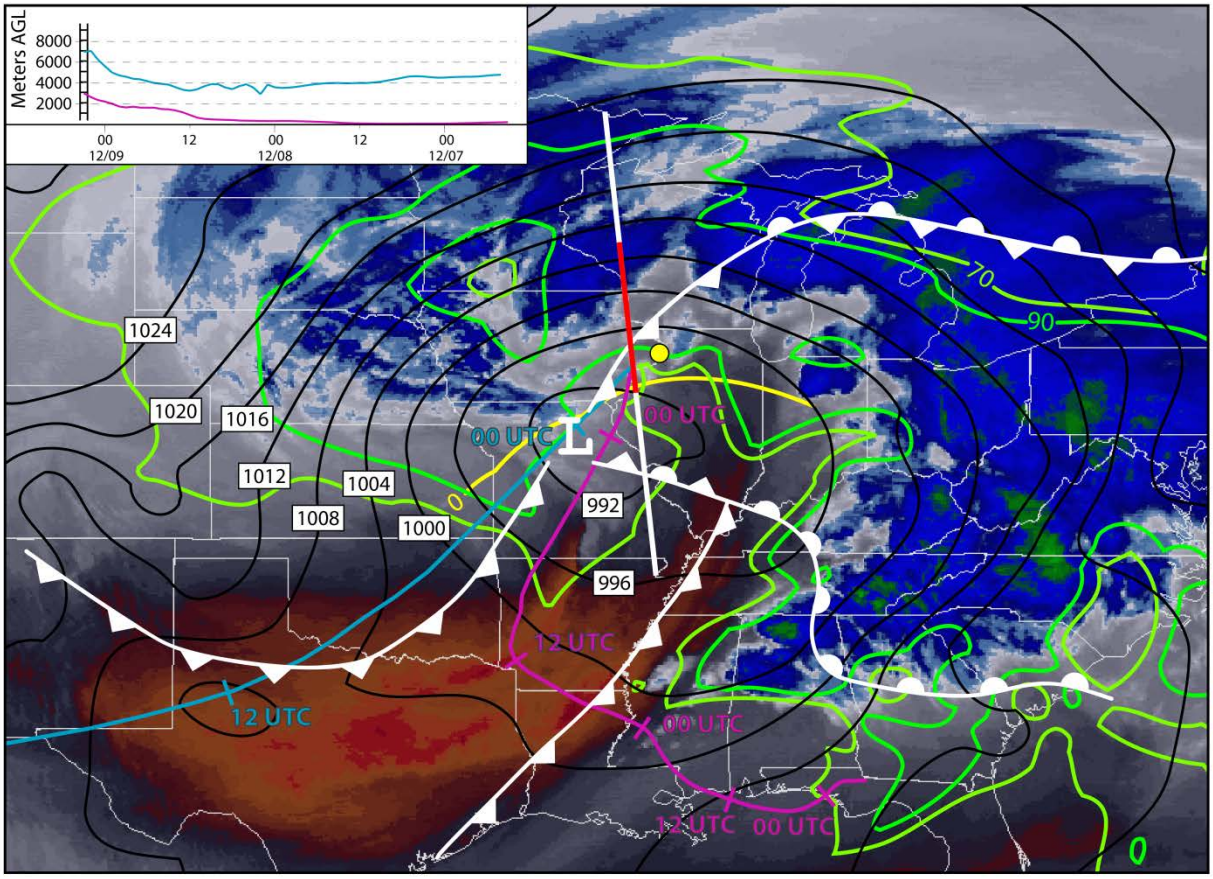

Figure 2.4: GOES water vapor imagery from 0332 UTC 9 December 2009 with 0300 UTC 9 December surface frontal analysis overlaid. The red line indicates the cross section location shown in Fig. 2.6, while the white line indicates the longer cross section in Fig. 2.7. Black contours are RUC 0300 UTC analyzed mean sea level pressure; light and dark green contours are 70% and 90% 500 hPa RH contours, respectively; the yellow line is the surface 0°C isotherm in the vicinity of the cross-section; and the fuchsia (blue) lines indicate back trajectories from near (above) the front, terminating at the points in Fig. 2.6. The inset shows these trajectories' altitudes versus time. The yellow dot indicates the sounding location for this case.

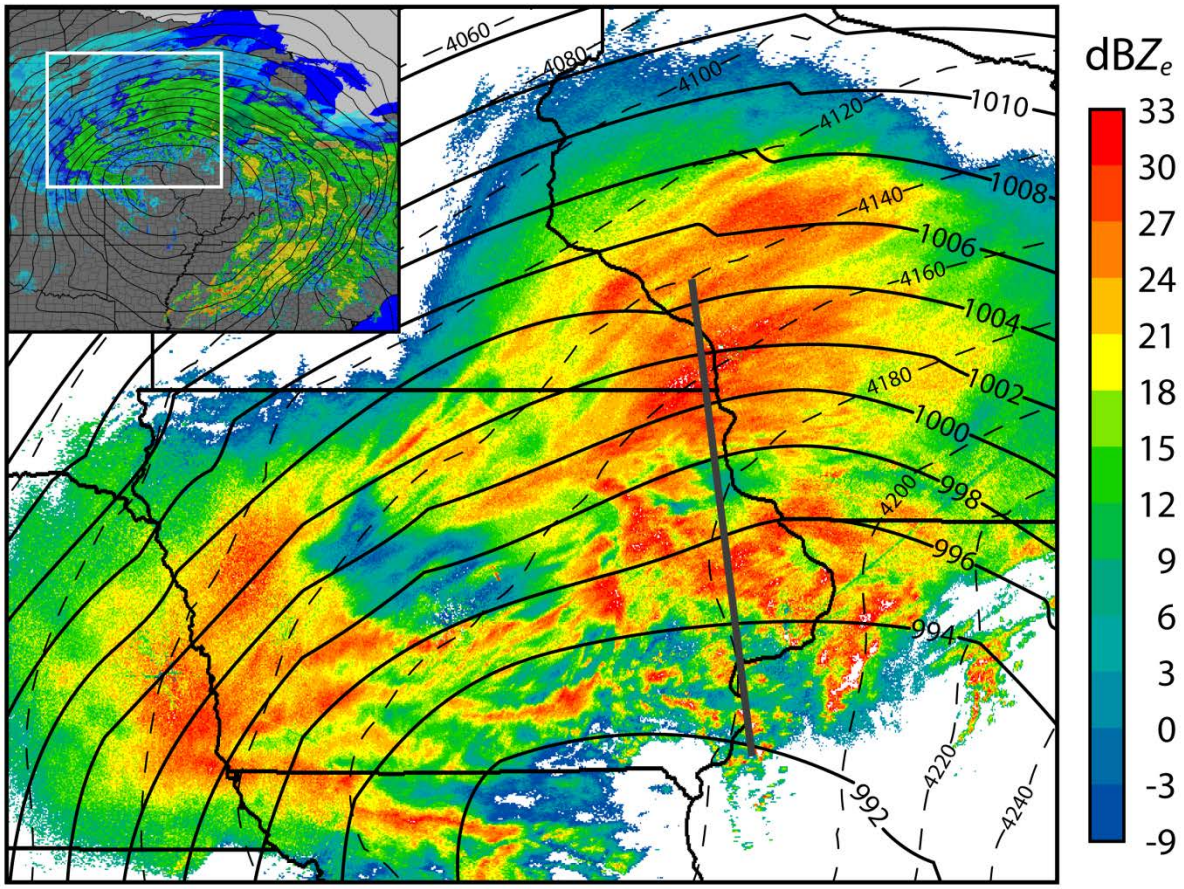

Figure 2.5: Level II base reflectivity from KARX, KDVN, KDMX, and KOAX at 0300 UTC on 9 December 2009. The 0300 UTC RUC analysis of mean sea level pressure (solid) and 700 hPa to 400 hPa thickness (dashed) is overlaid. The 0251–0351 UTC C-130 flight track is shown as the straight line. The area of the analysis is shown as the inner box in the inset.

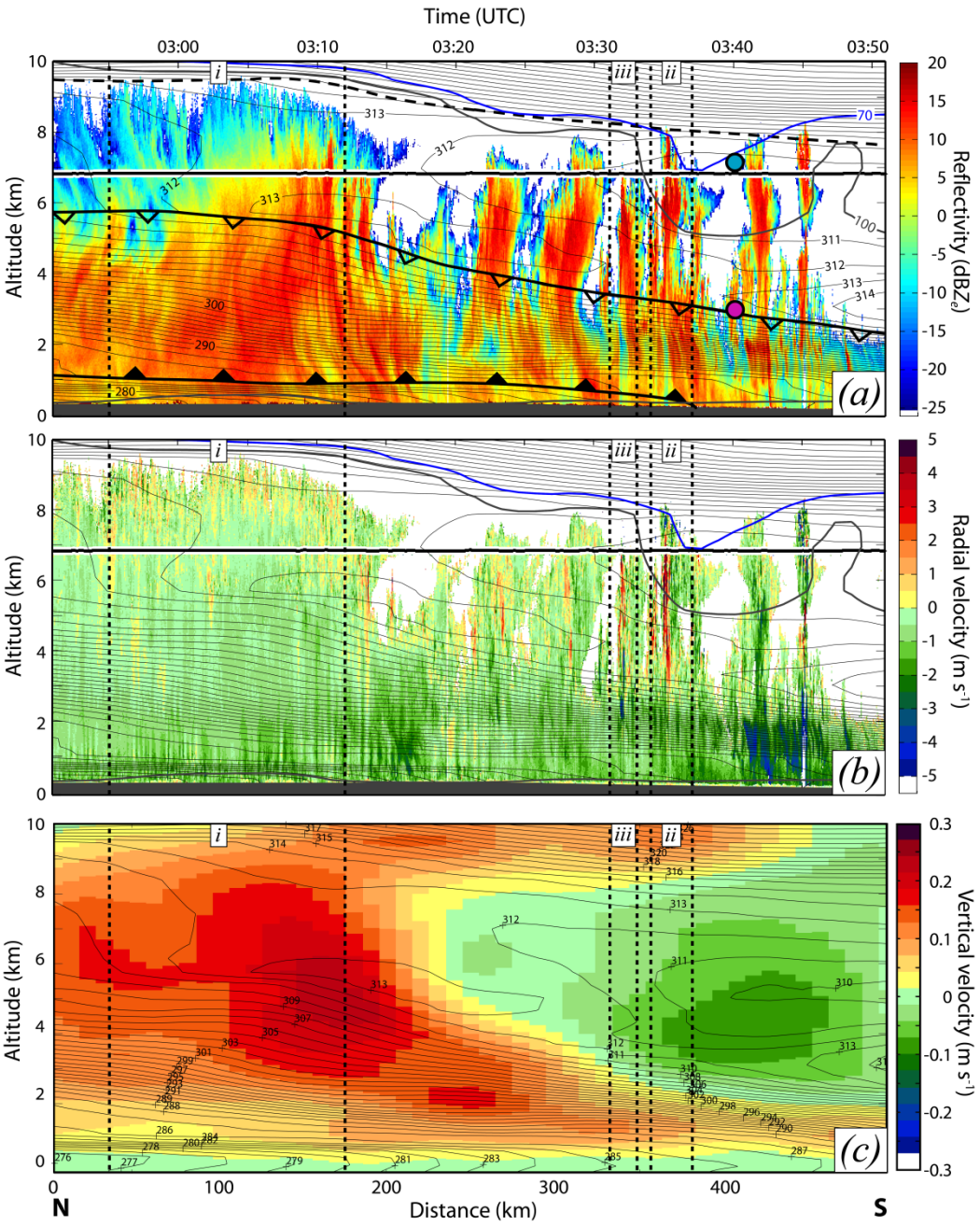

Figure 2.6: (a) Z_e from the WCR from 0251-0351 UTC 9 December 2009 and θ_{ei} from the 0300 UTC RUC analysis along the same cross section. The blue (dark grey) line denotes the 70 (100)% RH_i contour. The black dashed line is the tropopause. The horizontal black line is the C-130 flight track. The blue (fuchsia) dot indicates the endpoint of the backward trajectory shown in blue (fuchsia) on Fig. 2.4. (b) Vertical particle velocities (W) measured by the WCR, overlaid with θ_{ei} and RH_i from the RUC analysis. (c) Vertical air velocities ($\overline{w}$, shaded) and θ_{ei} for the one-hour RUC forecast valid 0300 UTC 9 December 2009 for the cross section corresponding to panels a & b. Regions *i*, *ii*, and *iii* indicate locations used for CFADs.

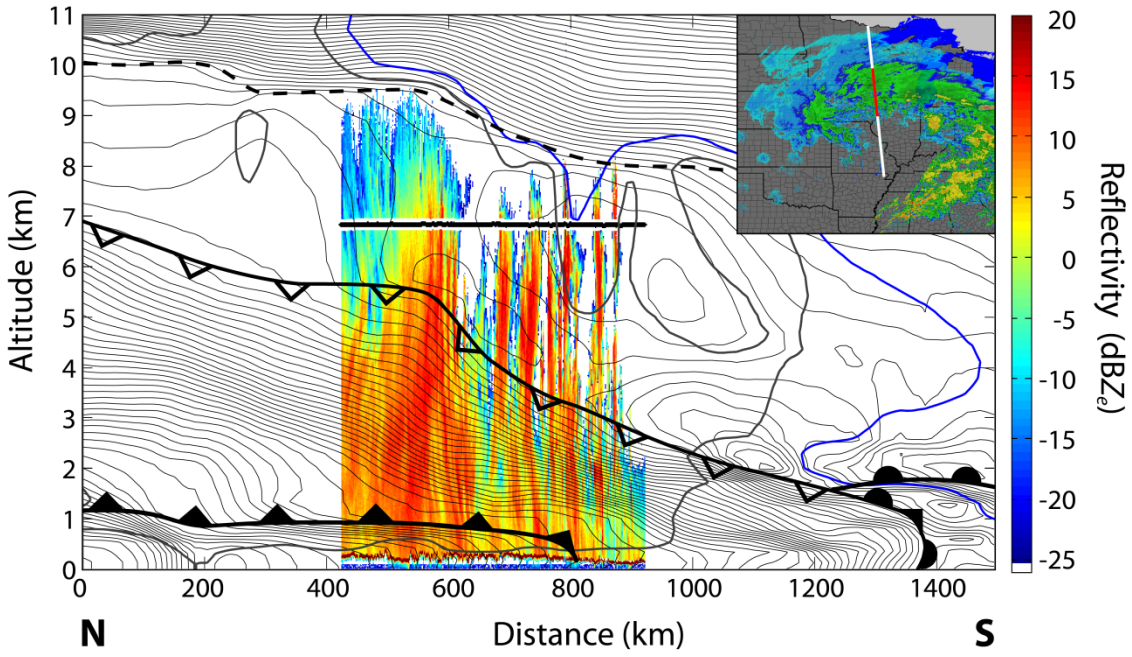

Figure 2.7: WCR Z_e from Fig. 2.6 and θ_{ei} from the 0300 UTC 9 December 2009 RUC analysis along the cross section indicated by the white and red line in the inset. The red part of the line in the inset is the location of the cross section in Fig. 2.6. The blue (dark grey) line denotes the 70 (100)% RH_i contour. The black dashed line is the tropopause. The horizontal black line is the C-130 flight track.

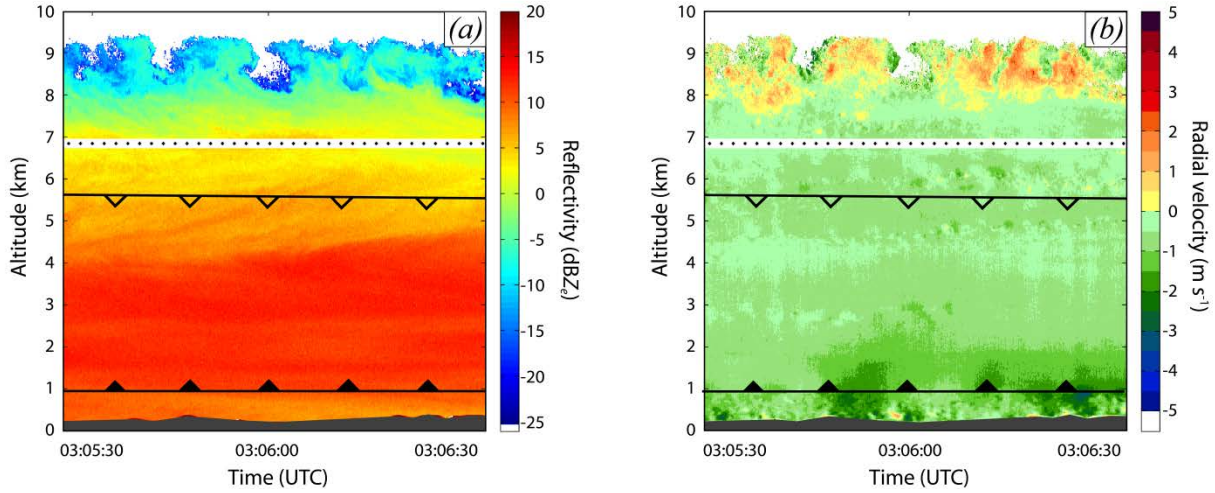

Figure 2.8: (a) WCR Z_e and (b) vertical total particle velocity (W) at a 1:1 aspect ratio from 030525-030637 UTC in Fig. 2.6.

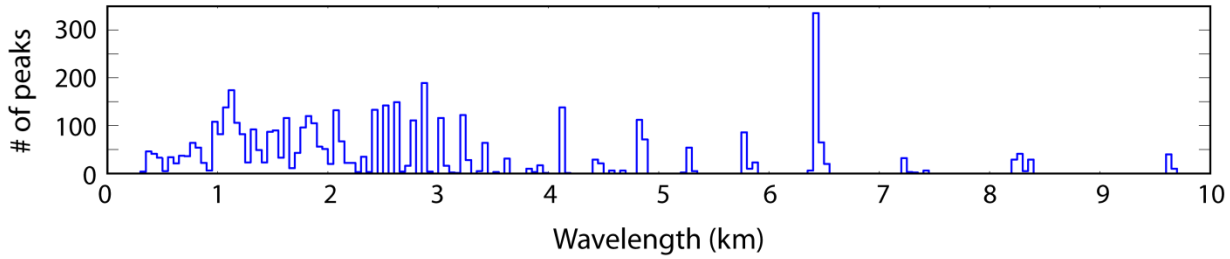

Figure 2.9: Frequency histogram of horizontal wavelengths identified from Fourier analyses of 1000 randomly selected Z_e time series within generating cells during the 9 December 2009 research flight.

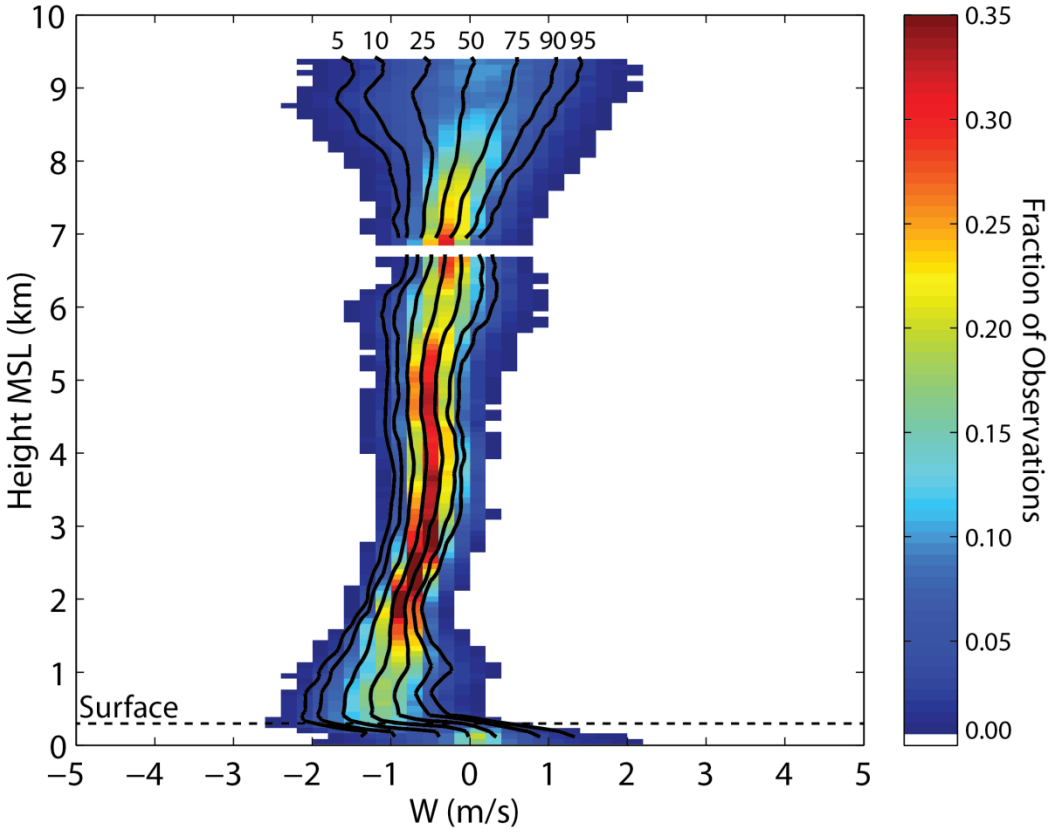

Figure 2.10: Contoured frequency by altitude diagram (CFAD) of *W* measured by the WCR for area (*i*) on Fig. 2.6. Color shaded values indicate percentage of observations at that altitude falling in each 0.2 m s^{-1} velocity bin. The break in the diagram, here below 7 km, is the aircraft altitude. The numbers on the contours denote the percent of observations with values to the left of the contour.

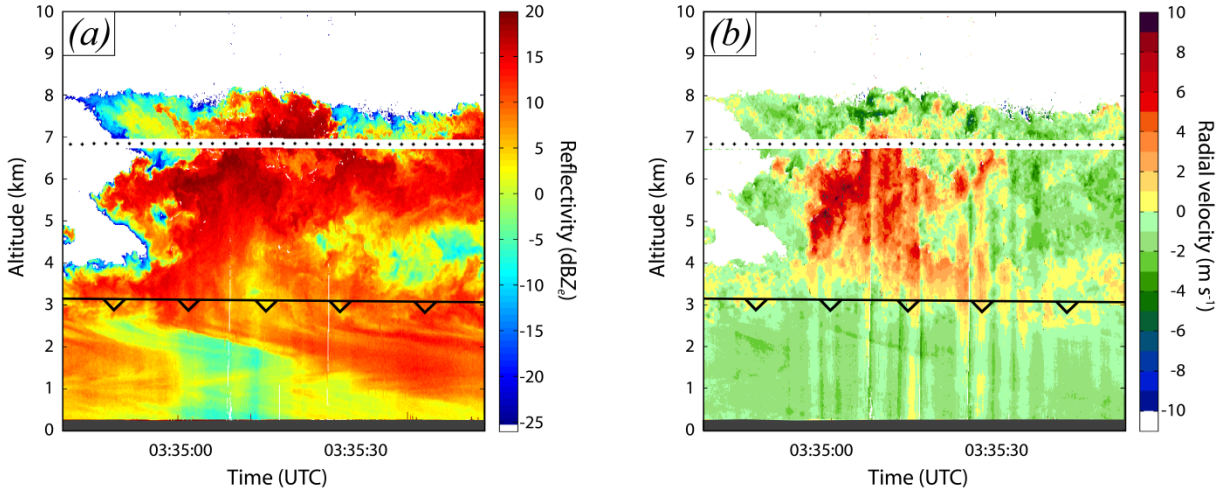

Figure 2.11: As in Fig. 2.8, but for 033450-033552 UTC.

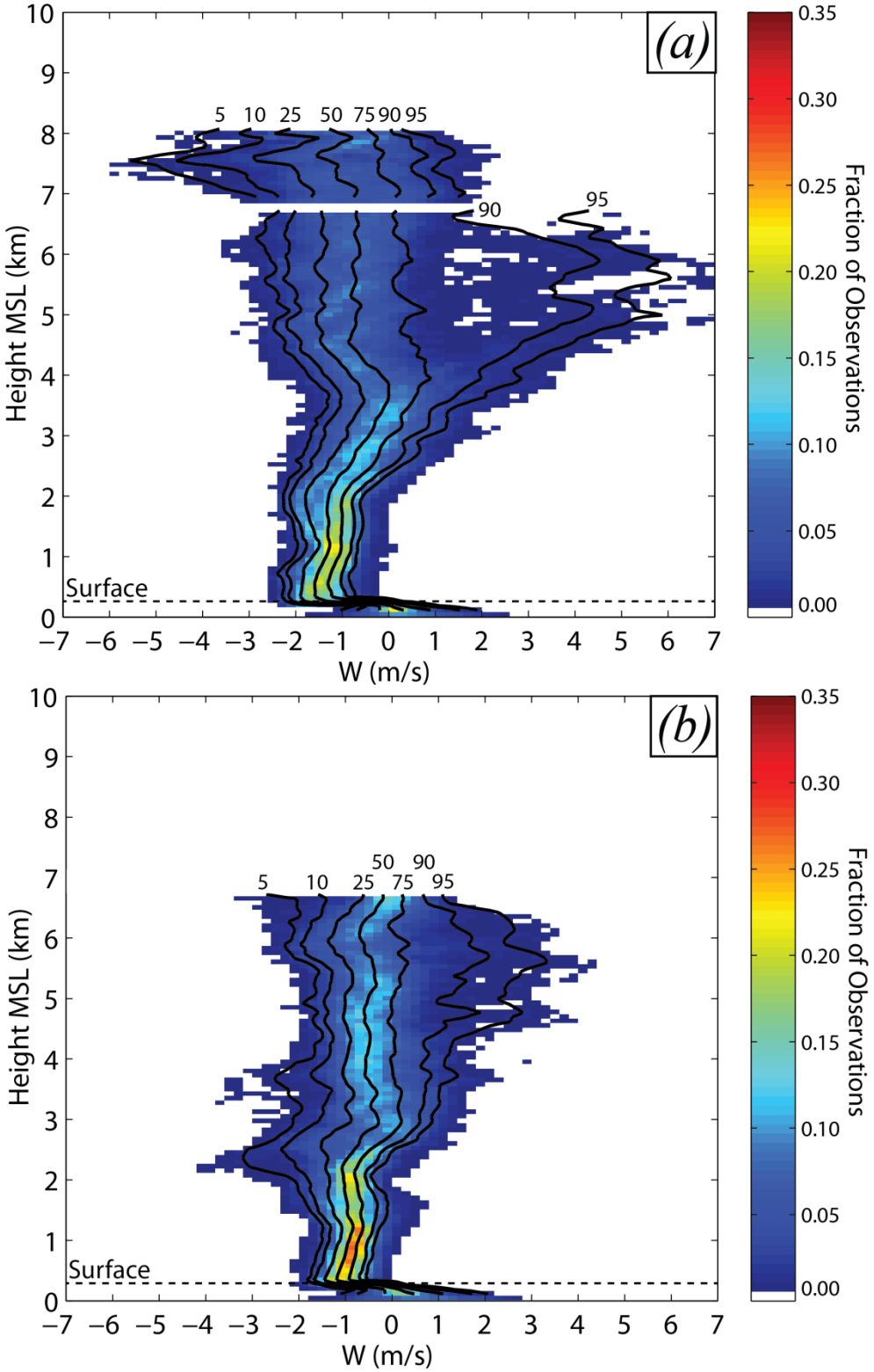

Figure 2.12: As in Fig. 2.10 but for areas (*ii*, a; *iii*, b) of Fig. 2.6.

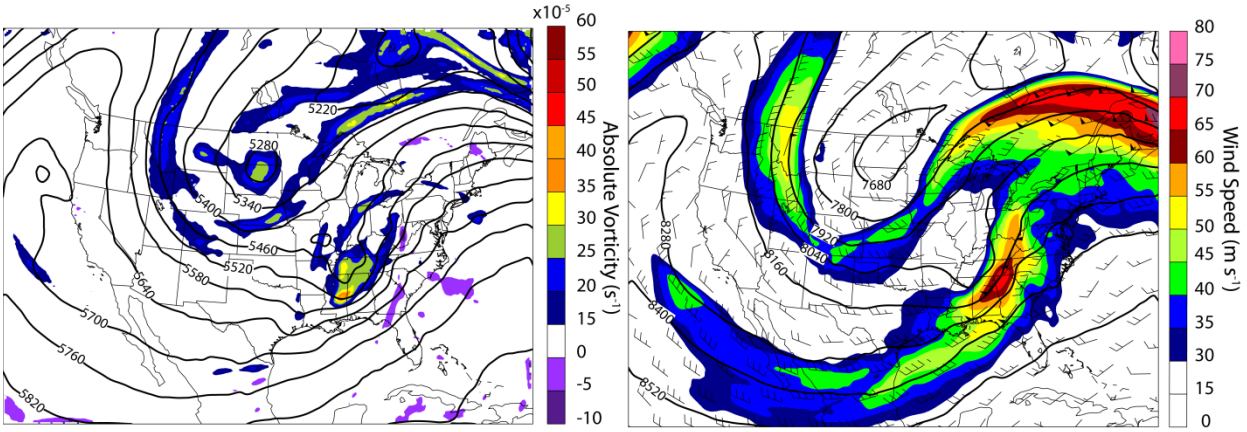

Figure 2.13: As in Fig. 2.3, but valid 0000 UTC 3 December 2009.

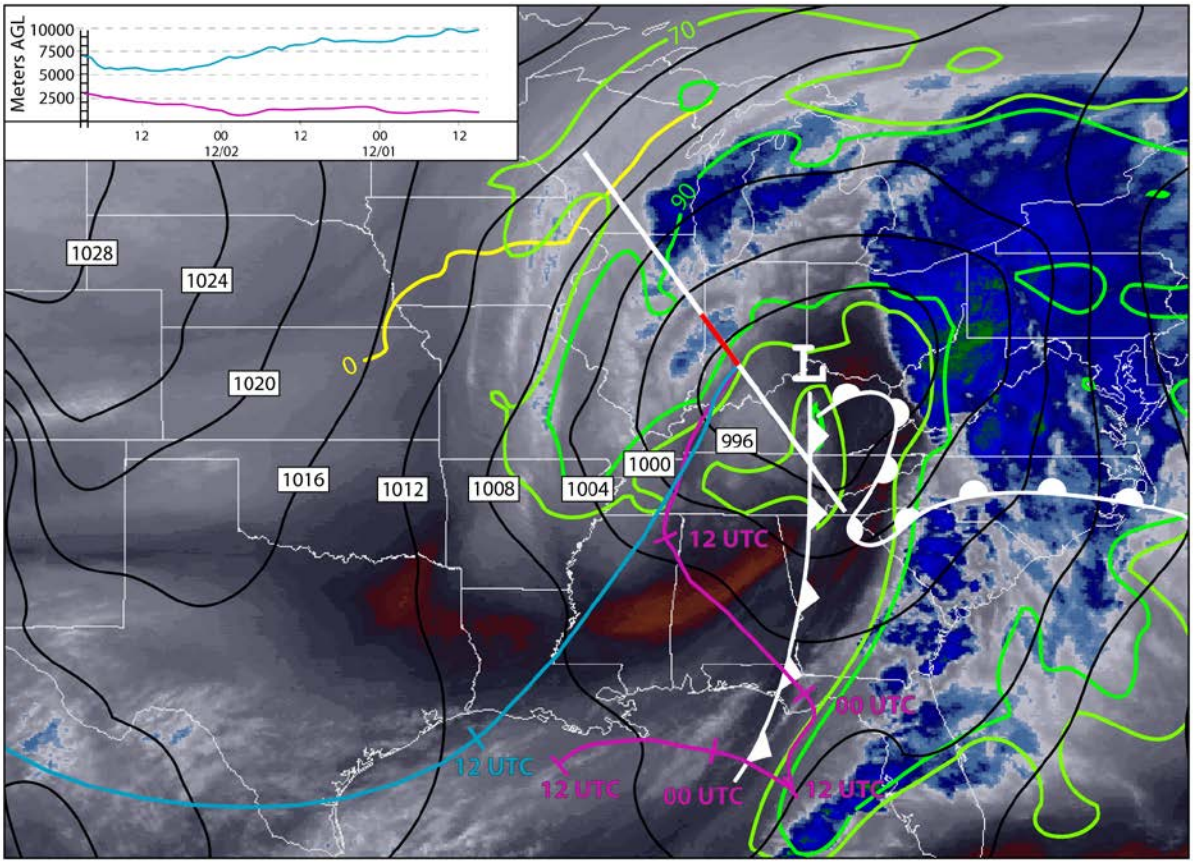

Figure 2.14: As in Figure 2.4, but for the 2340 UTC 2 December water vapor image and 0000 UTC 3 December surface frontal analysis and RUC data. Trajectory end points are shown in Fig. 2.16.

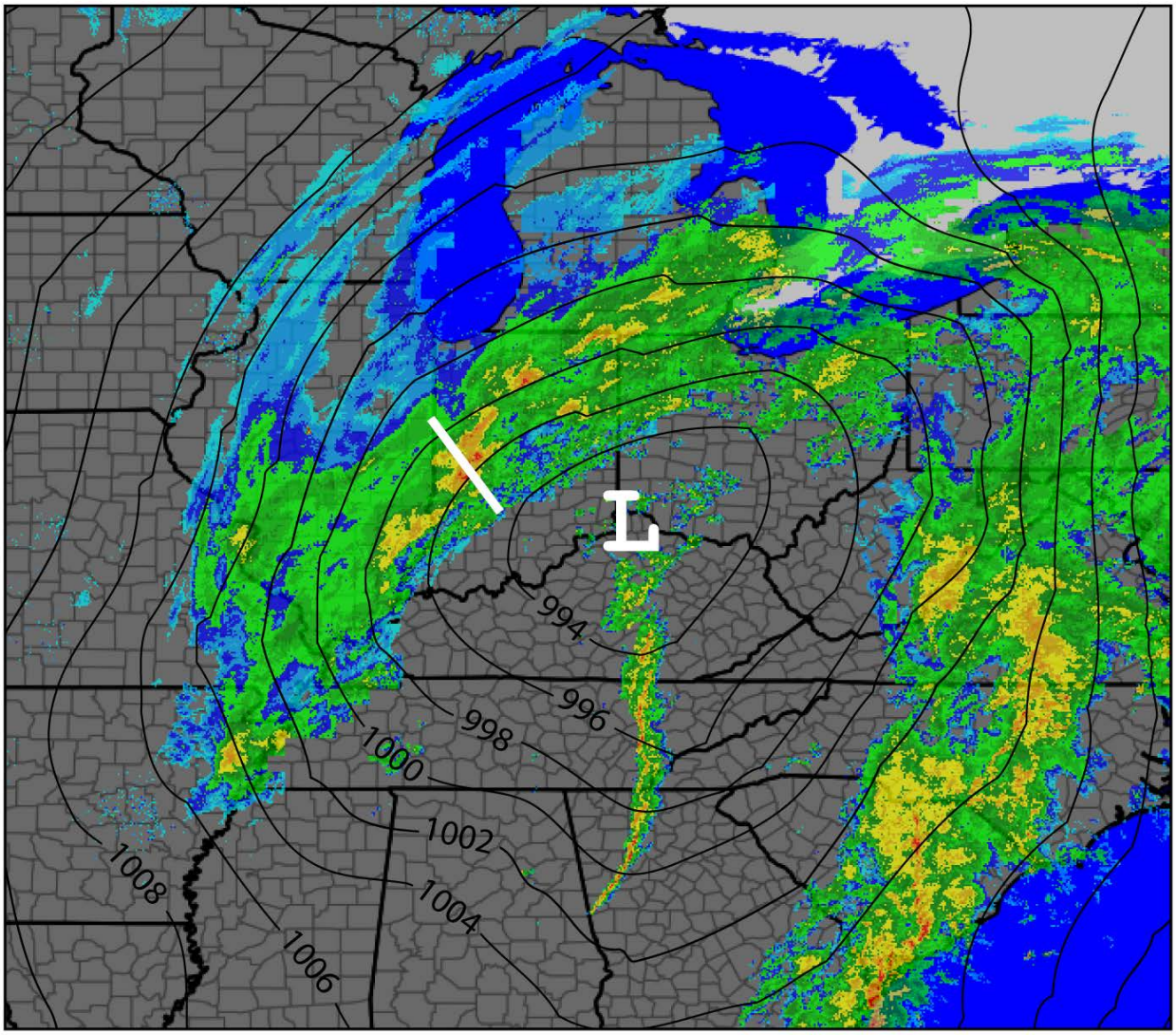

Figure 15: WSR-88D composite reflectivity overlaid with RUC mean sea level pressure analysis, both valid 0000 UTC 3 December 2009. White line indicates the C-130 flight track from 002430-004300 UTC.

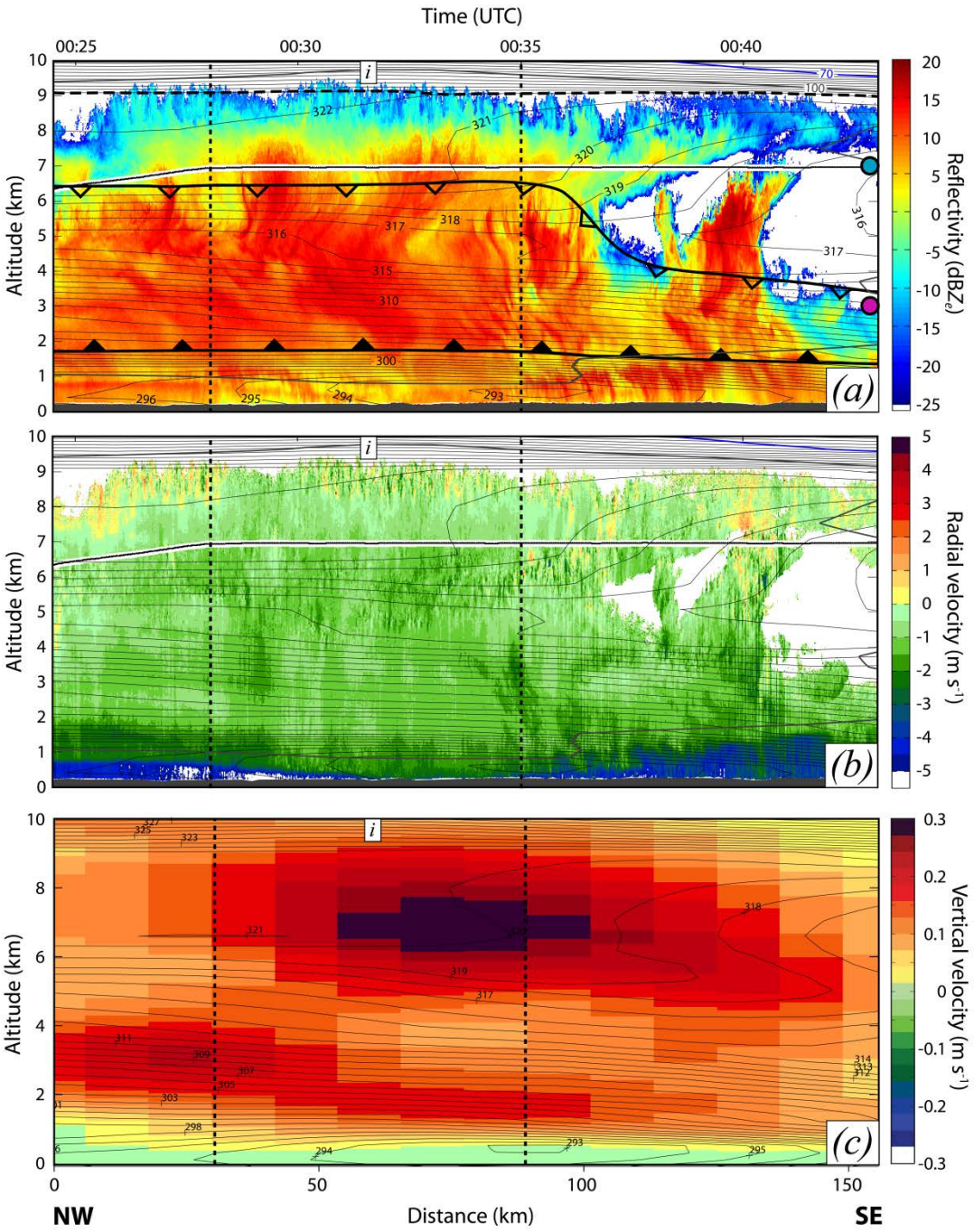

Figure 2.16: As in Fig. 2.6, but for the 002430-004300 UTC 3 December 2009 flight leg and RUC data valid at 0100 UTC.

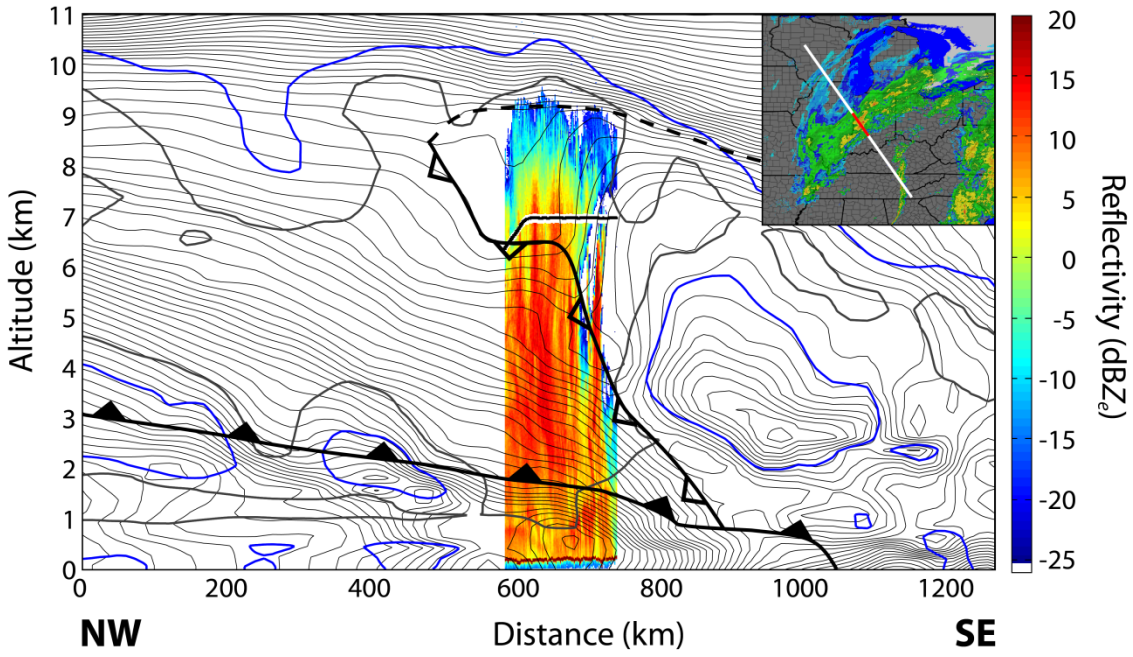

Figure 2.17: As in Fig. 2.7, but for the 002430-004300 UTC 3 December 2009 flight leg and RUC data and composite reflectivity valid 0100 UTC.

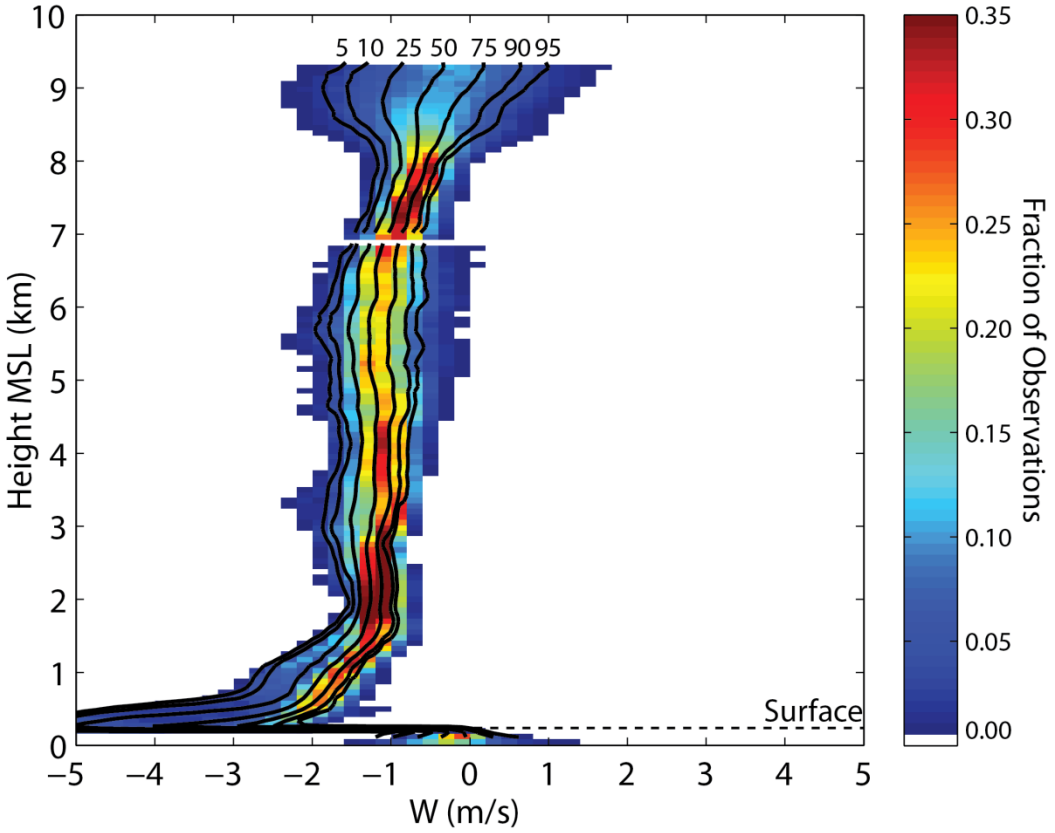

Figure 2.18: As in Fig. 2.10, but for area (*i*) in Fig. 2.16.

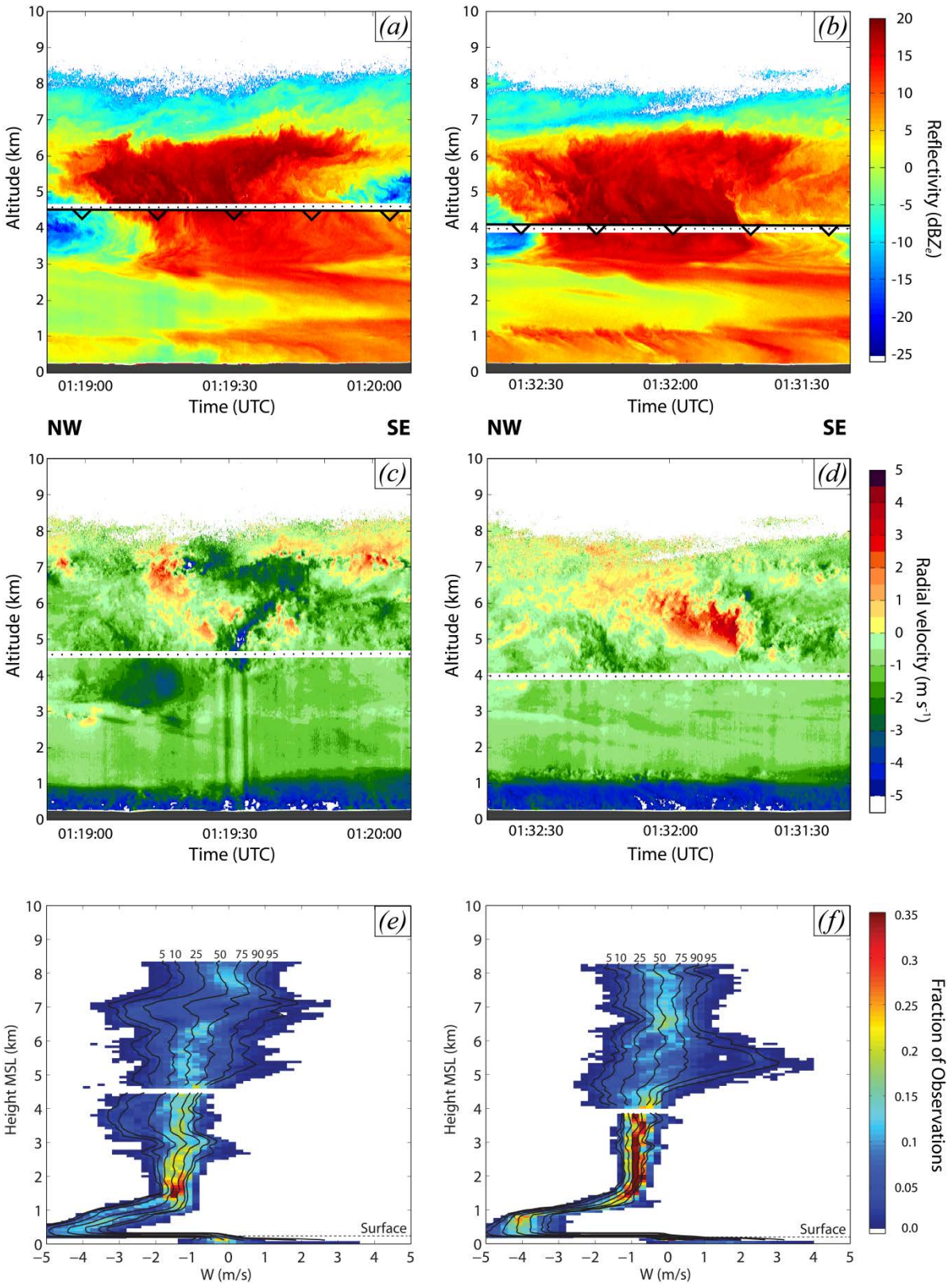

Figure 2.19: WCR Z_e at a 1:1 aspect ratio from: (a) 011852-012008 UTC and (b) 013119-013241 UTC 3 December 2009; (c,d) *W* measurements corresponding to panels a and b; (e,f) CFADs of *W* measurements in panels c and d.

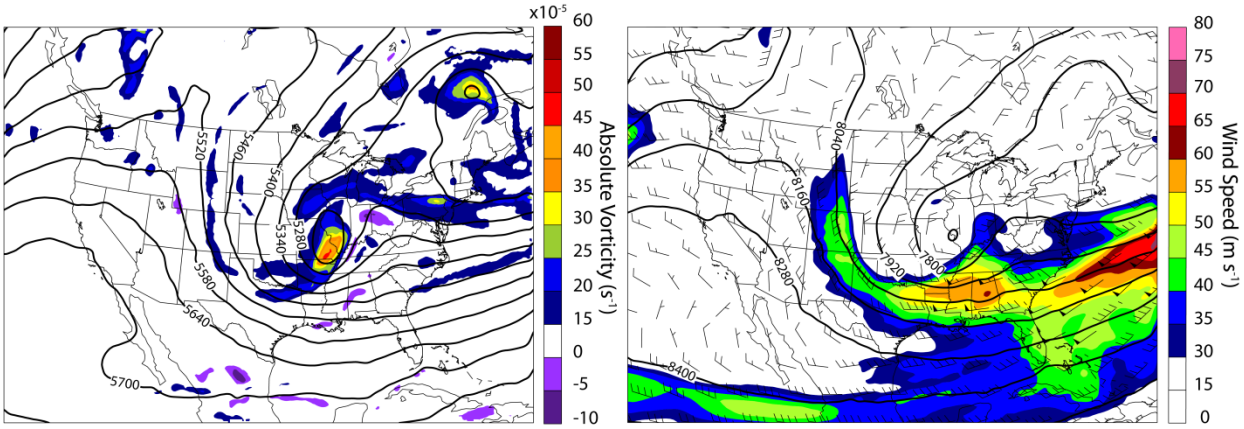

Figure 2.20: As in Fig. 2.3, but valid 0600 UTC 15 February 2010.

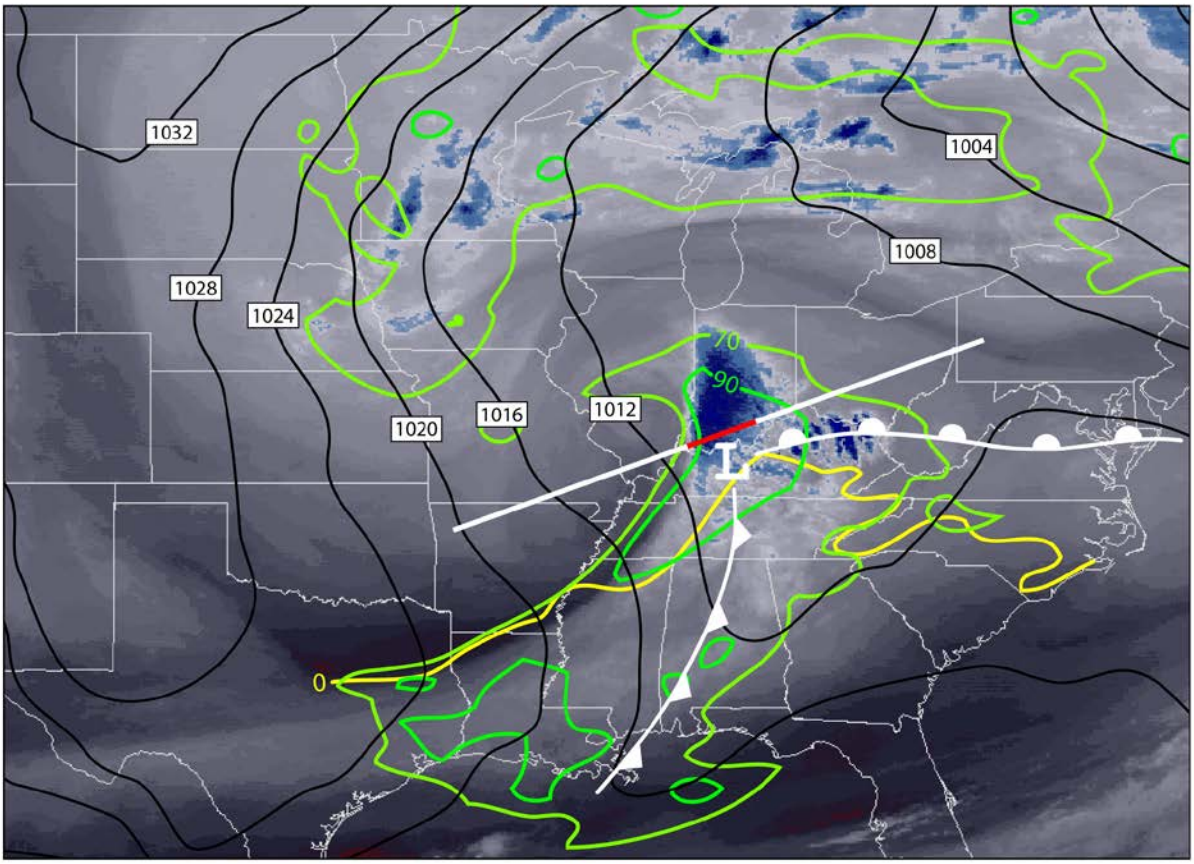

Figure 2.21: As in Figure 2.4, but with no trajectories shown and for the 0632 UTC 2 December water vapor image and 0600 UTC 15 February surface frontal analysis and RUC data.

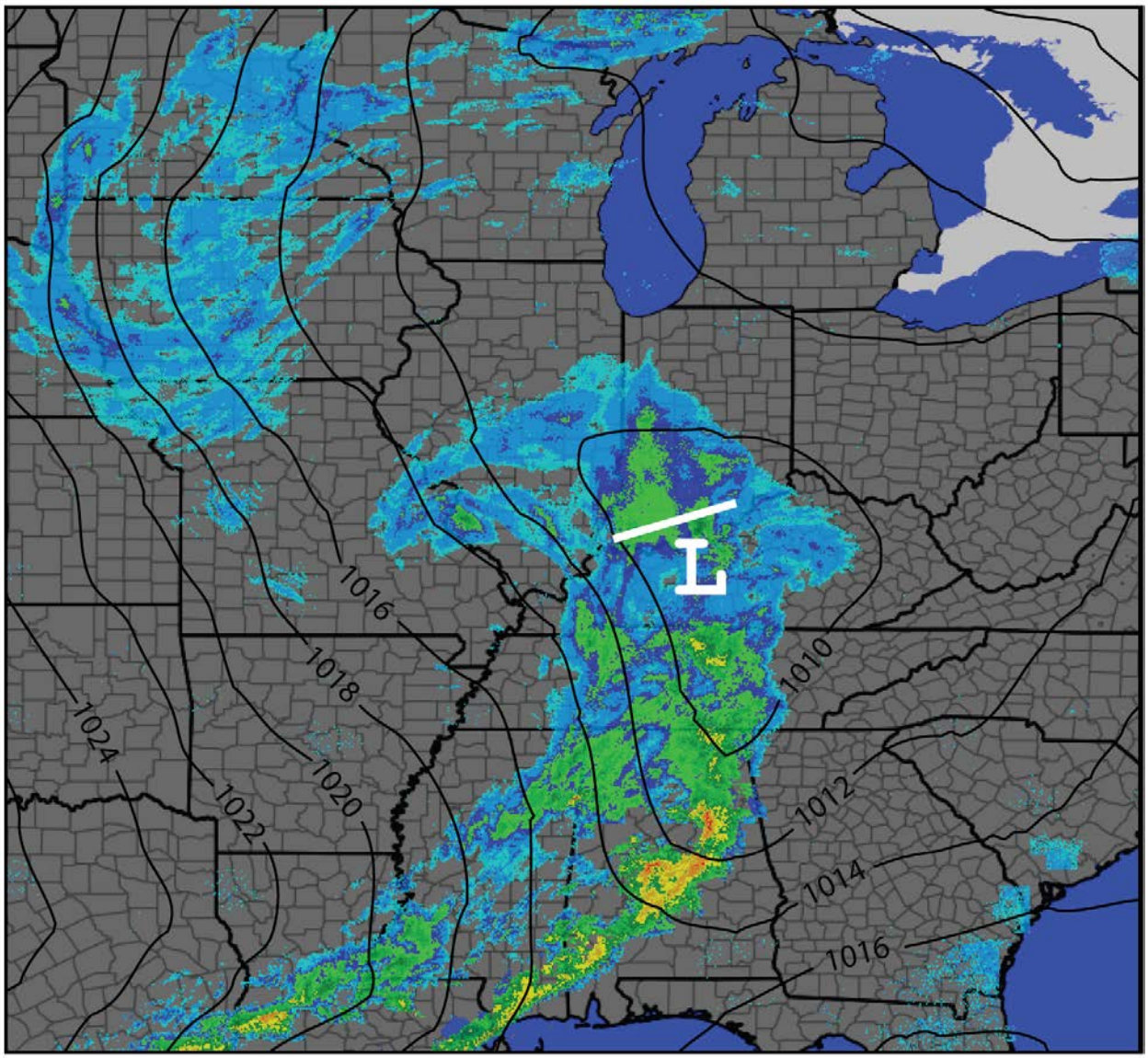

Figure 2.22: As in Fig. 2.15, but valid 0600 UTC 15 February 2010. The flight track shown here was valid for each leg of this research flight.

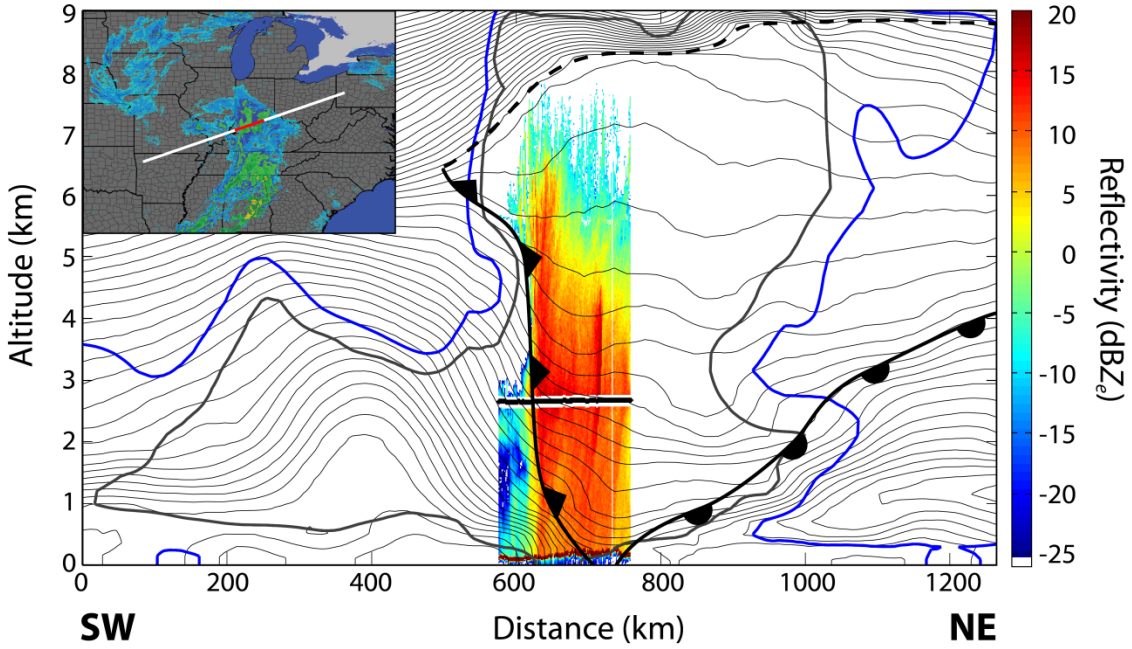

Figure 2.23: As in Fig. 2.7, but for the 0648-0715 UTC 15 February 2010 flight leg. RUC data and composite reflectivity are valid at 0700 UTC.

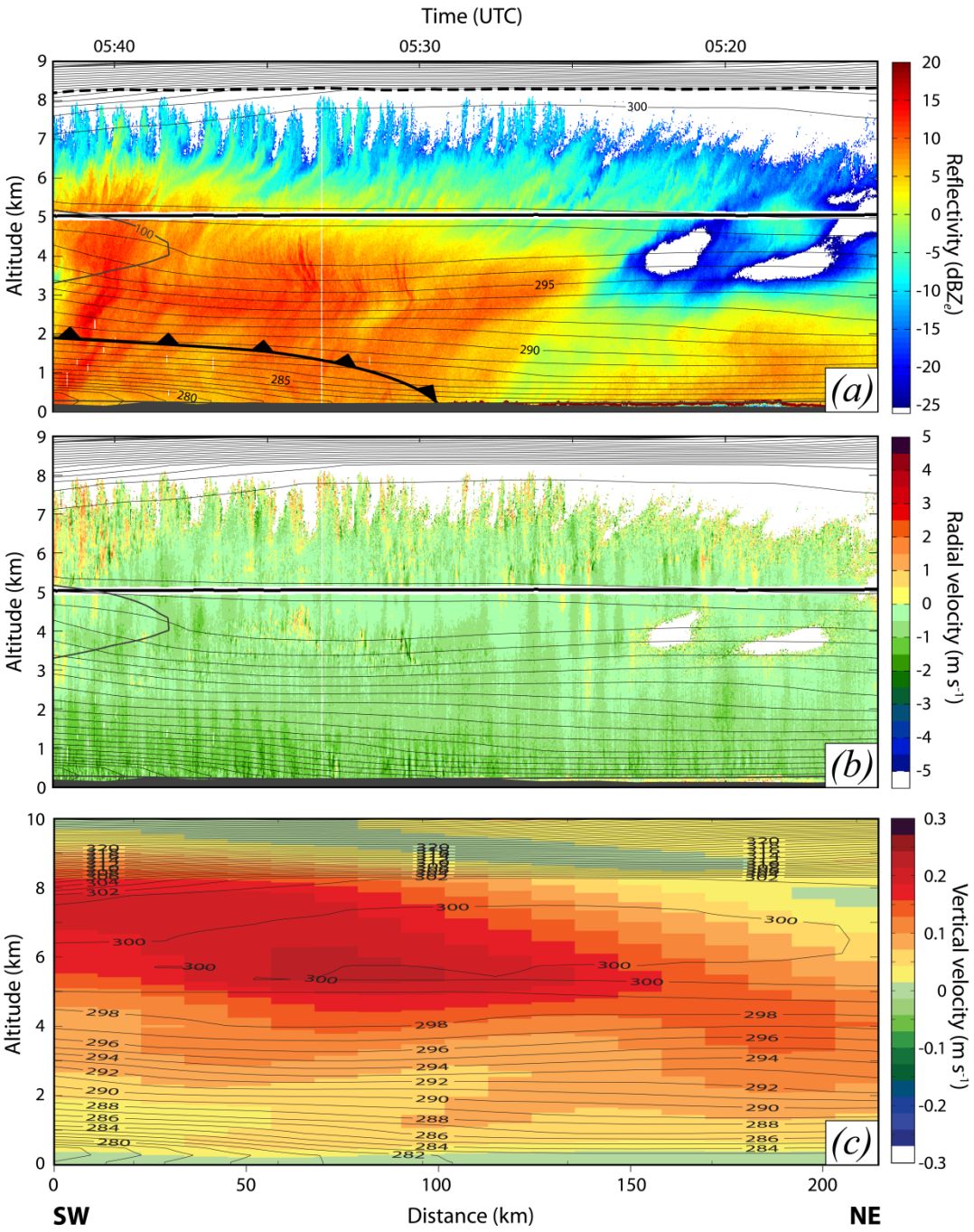

Figure 2.24: As in Fig. 2.6, but for the 0515-0542 UTC 15 February 2010 flight leg. RUC data are valid at 0500 UTC.

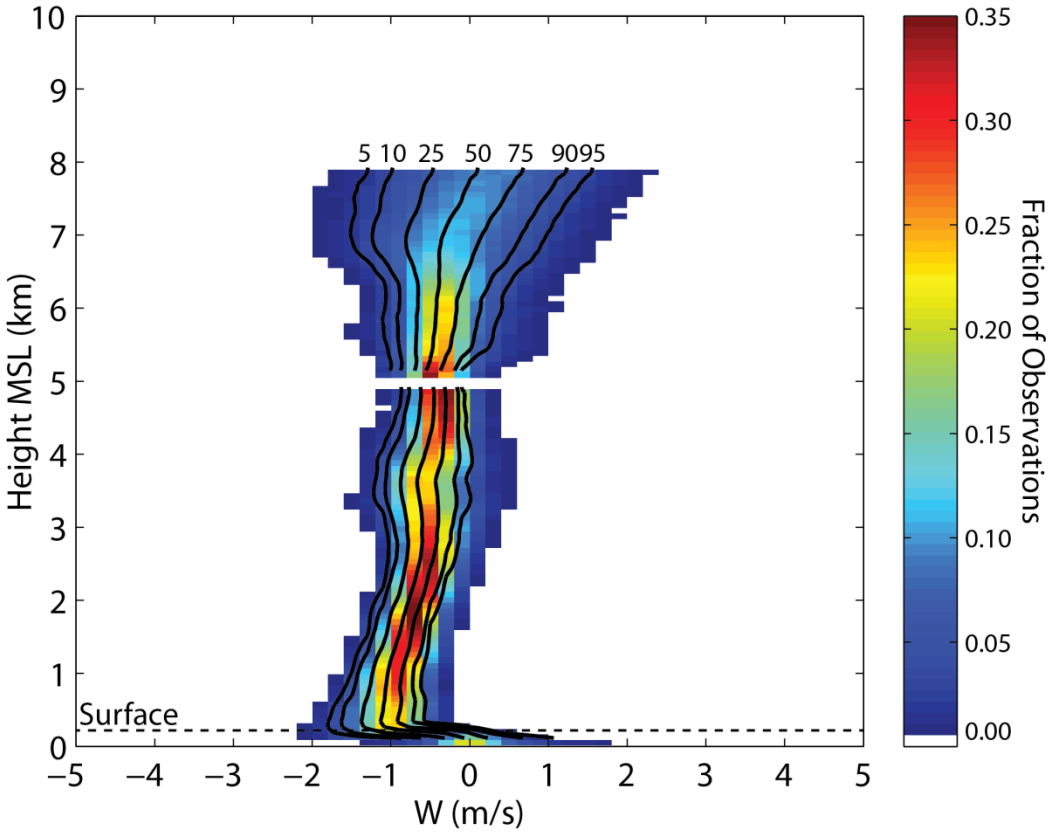

Figure 2.25: As in Fig. 2.10, but corresponding to the WCR profile shown in Fig. 2.24.

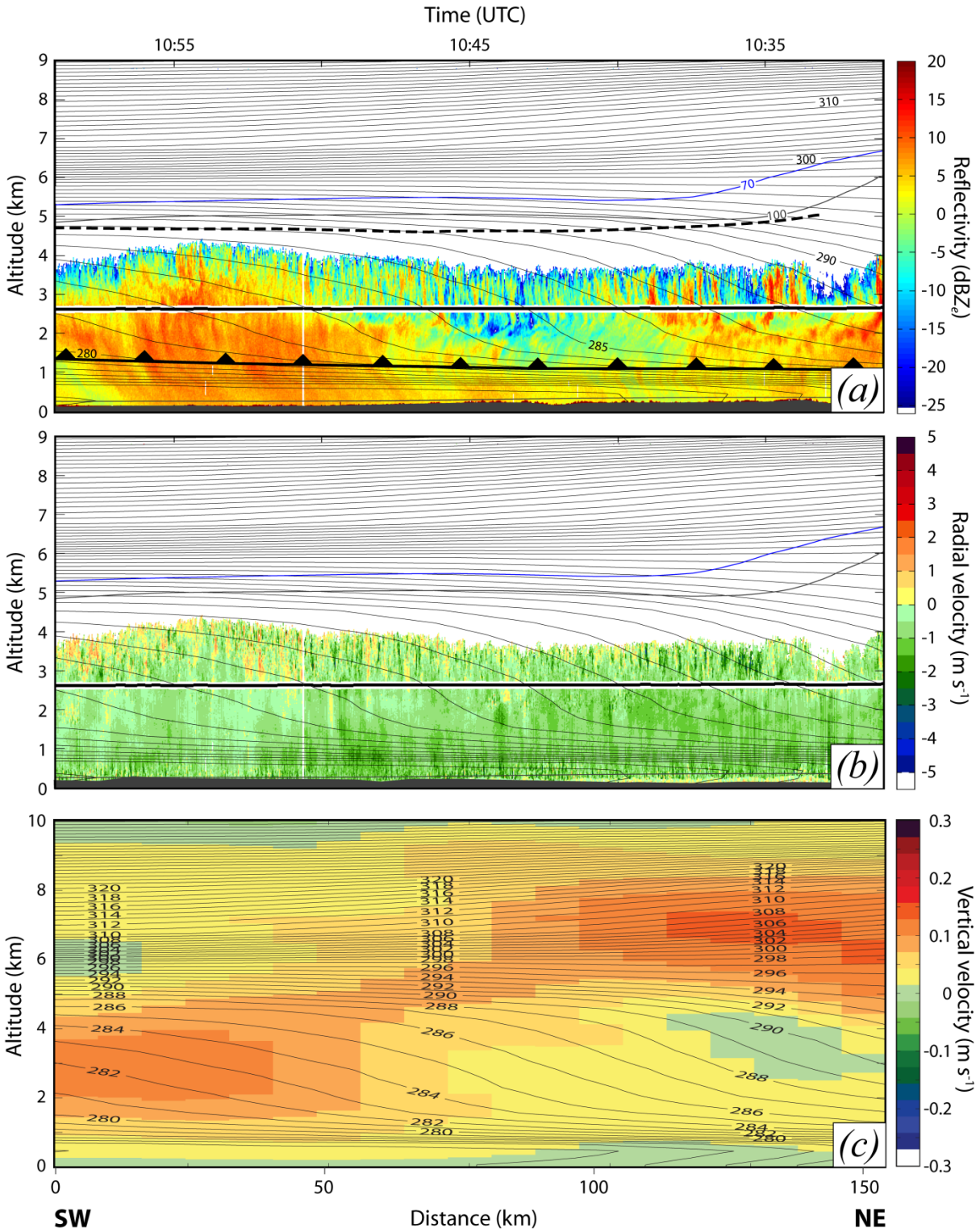

Figure 2.26: As in Fig. 2.6, but for the 1031-1059 UTC 15 February 2010 flight leg. The flight leg is along the same cross section as Figure 2.24, but the cyclone had moved east so that the aircraft sampled clouds behind the cold front. RUC data are valid at 1100 UTC.

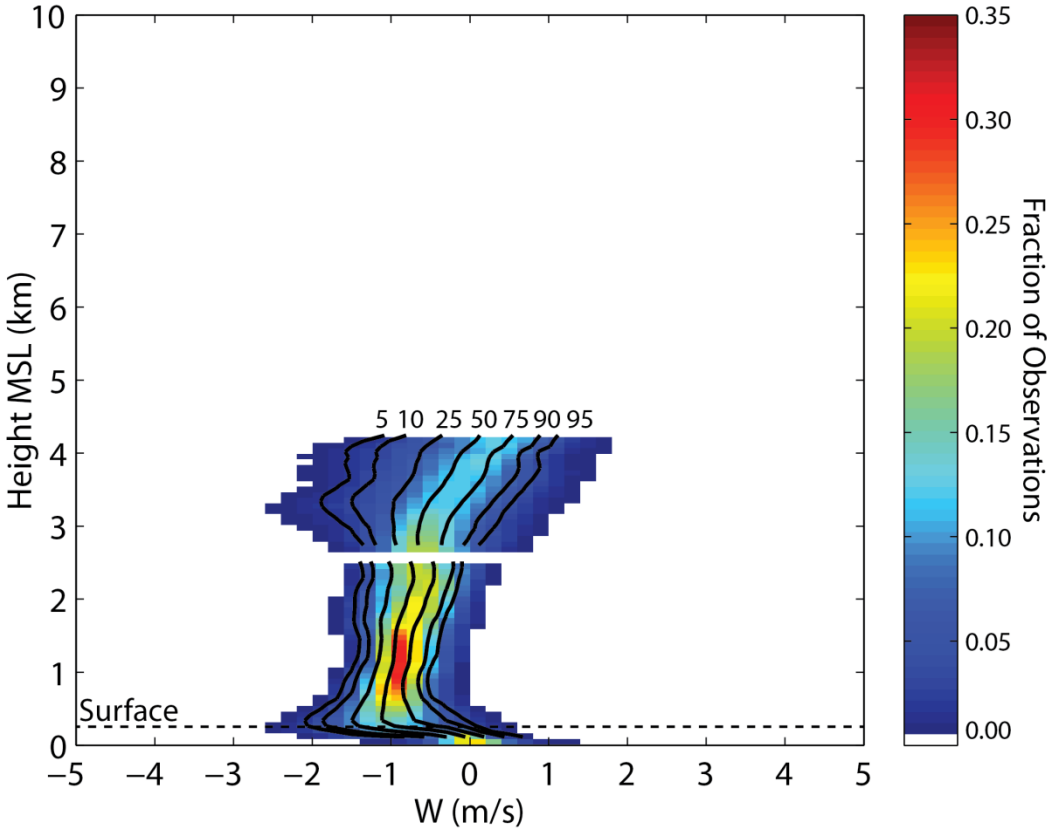

Figure 2.27: As in Fig. 2.10, but corresponding to the WCR profile shown in Fig. 2.26.

3) Elevated Potential Instability in the Comma-Head: Distribution and Development

3.1 Introduction

The comma-head region of cyclones is responsible for a variety of significant severe winter weather, including heavy snow, strong winds, and even lightning (Rauber et al. 2014). Past studies have used radar to study both the precipitation distribution as well as the intensity of precipitation and vertical motions in these cyclones. (e.g. Herzegh and Hobbs 1980; Sienkiewicz et al. 1989; Browning 2005; Cronce et al. 2007; Stark et al. 2013). Studies have also examined cold-season instability in the comma-head region of cyclones (Browning et al. 1973, Martin 1998; Halcomb and Market 2003; Moore et al. 2005). Cold season instability convective available potential energy (CAPE) values of more than 100 J kg^{-1} have been measured in the comma-head of cyclones (e.g. Market et al. 2012). Lightning, an indicator of the presence of convection, has been observed in these storms as well (Curran and Pearson 1971, Colman 1990, Holle and Cortinas 1998, Rauber et al. 2014, and Market et al. 2002). Previous studies have shown that convection in the comma-head forms from instability based above an elevated boundary (Moore et al. 1998; Martin 1998; Hunter et al. 2001; Halcomb and Market 2003).

The presence of elevated instability and convection was also reported in analyses developed from the PLOWS field campaign (Rauber et al. 2014, Rosenow et al. 2014). These analyses reported the presence of lightning and graupel in the 8-9 December 2009 cyclone, with vertical air velocities in the elevated convection ranging from 1 to 7 m s^{-1}. This chapter expands upon the findings of these analyses to understand the origins of elevated wintertime convection and the background environmental instability responsible for its formation within the comma

head by studying the relationship between this instability and airflows into the comma head region of the cyclone.

Ever since the publication of the Norweigian cyclone model (Bjerknes, 1910), attempts have been made to better understand how air combines to produce the various observed precipitation structures (e.g. Browning et al. 1973). A major area of study in cyclone airflows has concentrated on the diagnosis and description of the warm and cold conveyor belts (Carlson 1980). In particular, these conveyor belts have been examined with trajectory studies (e.g. Schultz and Mass 1993, Wernli 1997, Pfahl et al. 2014), though these studies have shown differing properties and paths for these conveyor belts (Schultz 2001).

Outside of conveyor belts, studies of other aspects of continental cyclone airflows and precipitation, in relation to cold season precipitation within the comma-head specifically, are rare. These studies (e.g. Fuhrmann and Konrad 2013, Rauber et al. 2015) have tended to focus on the development of larger-scale precipitation structures. Studies have also examined how air within the aforementioned conveyor belts interact with convection (Rasp et al. 2016).

In this chapter, the results of numerical simulations designed to understand how the environment for elevated convection develops in the comma-head are presented. Trajectory analysis, designed to understand how air parcels approaching the comma-head are modified by diabatic processes such that they arrive in the comma-head to form an environment where elevated instability exists in the comma-head region is employed. The 8-9 December 2009 cyclone, which was a significant wintertime cyclone previously described (Rosenow et al. 2014, Rauber et al. 2014), is the focus of this analyses, as the storm had well-documented elevated convection, positive most unstable CAPE (MUCAPE) above the frontal inversion, and produced

occasional lightning discharges. The first goal of the simulation is to produce a simulation of a cyclone that is consistent structurally with the observed cyclone, particularly in that it produces the observed comma-head instability. Data from this simulation are then used with the goal of understanding the evolution of air that results in the creation of the potentially unstable layer in which convection forms.

The methodology is described in section 3.2. In section 3.3, the simulation is compared to the observations. In section 3.4, the evolution of the elevated instability within the modeled cyclone is discussed. The results of trajectory analysis for parcels arriving in the region of the comma-head where potential instability was observed is then presented, focusing on how diabatic processes modify the air parcel properties and how these air parcels juxtapose to create the conditionally unstable environment. The chapter concludes with a discussion of the mechanisms by which changes in air parcel properties occur along trajectories.

3.2 Methodology

This study uses observational data from the PLOWS field campaign, the initialization data from the RUC model, as well as results from a numerical simulation designed to study instability and convection. The cyclone studied here, the 8-9 December, 2009 cyclone, was chosen because the cyclone was the best observed example of an intense cyclone during PLOWS, and because of the availability of observations of elevated convection in the storm. The data used in this study include special rawinsondes and reflectivity data from the Wyoming Cloud Radar (WCR). The WCR data used in this chapter were taken during the flight leg shown in Figure 2.5. The PLOWS deployment strategies and the WCR data processing routines are described in detail in Rosenow et al. (2014) and Rauber et al. (2014).

A real data simulation of the 8-9 December storm was carried out using the Weather Research and Forecasting (WRF) model, version 3.5.1 (Skamarock et al. 2008). Two domains were used (Fig. 3.1), with horizontal grid spacing of 9 km and 3 km. The resulting domains consisted of 1002 by 714 points and 988 by 907 points for the outer and inner grids, respectively. The settings and parameterizations used for the WRF simulation are presented in Table 3.1, and are summarized below. There were 120 prescribed vertical levels up to a model top of 60 hPa, focused on the troposphere. The model resolution and domains were designed to ensure that mesoscale flow features, particularly around fronts, were sufficiently resolved to allow the formation of potential instability. The size of the outer domain was chosen to be large enough for trajectories within faster upper-level flow to remain inside the domain. GFS model data were used for model initialization and 6-hourly boundary conditions.

The Kain-Fritsch cumulus parameterization (Kain and Fritsch, 1990) was used for the outer domain, and the inner domain was convective permitting. The model time step was 20 seconds in the outer domain and 6.67 seconds in the inner domain. Thompson microphysics (Thompson et al. 2008) and Rapid Radiative Transfer Model for Global Climate Models (RRTMG, Iacono et al. 2000) radiation schemes were used based on favorable comparisons to PLOWS observations in testing described by Keeler et al. (2016a). A 5 km deep Rayleigh damping layer was placed at the top of the model to prevent wave reflection off the model top.

The model initialization time was chosen to be 63 hours (60 hours plus 3 hours to allow model initialization at the nearest synoptic time) prior to the time of the intensive observation period with the WCR (see the radar cross section in Fig. 2.6) to allow for 63 hour backward trajectories to be calculated. Nudging was not used in the simulation. Output was saved every five minutes to provide high temporal resolution data for computation of trajectories.

Trajectory release points were selected based on the presence and location of potential instability in the model. Thousands of trajectories were calculated in and near the areas of potential instability, with the trajectories providing information about the sources of air that led to the development of potential instability. The trajectories presented were all calculated on the 9 km domain, but the two-way nesting in the model allowed information from the inner domain to be present in the outer domain.

The algorithm in the Read, Interpolate, Plot (RIP) software package was used to calculate backwards trajectories (Stoelinga 2009). The trajectories were initialized in three north-south oriented two-dimensional y-z planes across the comma-head region. Figure 3.2 shows a plan view of WRF simulated reflectivity at 0300 UTC, with the cross-sections where backwards trajectories were initialized indicated by black lines. These locations were chosen based upon the location of the region of maximum elevated instability in the comma-head of the simulated storm at 0300 UTC on 9 December. Within these planes, trajectories were released at every horizontal model grid point at altitudes of 0 km, 1 km, and every 0.25 km from 1.5 km to 9 km AGL. The altitudes were chosen to ensure high vertical resolution between the frontal boundary and the tropopause, where the potential instability and the convection were observed.

Values of potential temperature (θ), equivalent potential temperature (θ_e), and mixing ratio (q), which are conserved for adiabatic and/or pseudoadiabatic flow, were saved along trajectories. These parameters change in the presence of diabatic processes, and show the nature of diabatic changes that occur as air moves forward with time. Other variables, such as pressure and temperature, were saved to supplement the analysis of conservative variables.

3.3 Comparison of Simulation with Analysis

This section describes the temporal synoptic-scale evolution of the observed cyclone and compares it to the WRF simulation of the storm at two times, 48 hours and 60 hours after model initialization. Figure 3.3 shows six panels: two each at 300 hPa, 500 hPa, and the surface valid at 1200 UTC on 8 December 2009. Plots in the left column are from the initialization of the Rapid Update Cycle (RUC) model (hereafter, the analysis), and the right column, 48 hour forecasts from the WRF model (hereafter, the simulation).

The 8-9 December 2009 cyclone was forming at 1200 UTC on 8 December as a shortwave trough and associated ~70 m s^{-1} jet streak was present within the base of a longwave trough over the Rocky Mountains (Fig. 3.3a). While the jet stream positioning was mostly similar between the analysis and 48 hour simulation, there were subtle differences that led to differences in how the cyclone evolved in the simulation. The jet stream in the simulation at 300 hPa in Fig. 3.3b was about 50 km further north than in the analysis, which resulted in its left exit region being located a similar distance northward as well. The jet streak also was slightly stronger in the simulation, with an area of winds in excess of 70 m s^{-1} several times larger than in the analysis.

The axis of the vorticity maximum at 500 hPa associated with the shortwave trough was located over central and northern Arizona at 1200 UTC in the analysis (Fig 3.3c), placing the ascent region associated with differential cyclonic vorticity advection over northern New Mexico. At 500 hPa in the simulation, shown in Fig. 3.3d, the vorticity maximum was also about 100 km further north of its position in the analysis. In addition to the position difference, the vorticity maximum was more elongated to the north by an additional 100 km, which led to increased ascent to the north of the region of maximum ascent in the analysis.

At the surface in the analysis, the cyclone that ultimately affected the Midwestern US was forming in north-central New Mexico, within the surface trough of low pressure in Fig. 3.3e**.** The trough, with minimum pressures around 990 hPa, extended south from a deeper 984 hPa cyclonic circulation in western Colorado. The developing cyclone over New Mexico moved east, while the low pressure center over Colorado weakened. The subtle differences in the simulation continue at the surface in Figure 3.3f, where the cyclone over western Colorado was still present and had similar minimum pressure (986 hPa) to the simulation. The pressure trough to the southeast over New Mexico was notably absent in the simulation. This difference manifests itself in the simulation as the 986 hPa low in Colorado moved east to become the dominant cyclone over the Plains.

Figure 3.4 shows a six-panel plot of the same fields as Fig. 3.3, but for 0000 UTC on 9 December, three hours before the cross-sectional analysis presented in the next section. In the analysis, by 0000 UTC, the jet streak had expanded and progressed east, now consisting of multiple speed maxima. The left exit region of the 70 m s^{-1} lead speed maximum was located over SW Missouri and SE Kansas (Fig. 3.4a). At 300 hPa in the simulation (Fig. 3.4b), the eastern-most end of the 70 m s^{-1} jet streak over NW Arkansas and NE Oklahoma was about 50 km further NW than it was in the analysis, which shifted the left exit region a similar distance NW compared to the analysis.

At 500 hPa in the analysis, the vorticity maximum associated with the shortwave trough progressed to the ENE and was centered over Kansas and Oklahoma by 0000 UTC (Fig. 3.4c). The 500 hPa pattern in the simulation (Figure 3.4d) showed slight differences compared to the analysis, with the vorticity maximum 50-100 km further west with a more negative tilt.

At the surface in the analysis, the cyclone continued to develop and had a minimum pressure of 995 hPa over southern Missouri (Fig. 3.4e). The cyclone would eventually deepen to around 980 hPa over southern Lake Michigan by 1200 UTC on 9 December (not shown). At the surface in the simulation (Fig. 3.4f), the cyclone is both deeper (984 hPa) and ~200 km further west when compared to the analysis. This simulated cyclone is the original, deeper Colorado cyclone that moved eastward. That allowed the cyclone to start from a lower pressure instead of having to deepen as it moved into the central US, as it did in the analysis.

As the actual cyclone matured, it produced a large precipitation shield, as evidenced by the 0005 UTC 9 December radar composite in Figure 3.5. The cyclone produced precipitation across an extensive area of the United States, from deep within the warm sector in the southeastern US back across the comma-head, which was located from Kansas to Wisconsin at that time. In the comma-head region, there was extensive stratiform precipitation across much of IA, MN, WI, KS, and IL, generally on the poleward side of the comma head. Within the southern and eastern potions (the equatorward side) of the comma-head, more cellular echoes were present, although not easily seen in the national composite in Figure 3.5. They are apparent in Figure 2.5, which shows the reflectivity from local radars.

The corresponding 1 km AGL simulated radar reflectivity associated with the cyclone is shown in Figure 3.6. When compared to the observed radar reflectivity in Figure 3.5, the WRF reflectivity resembles the reflectivity composite when the shift in the cyclone center location is taken into account, specifically the westward bias in the simulation. The model captures the extensive warm-sector precipitation, the large, stratiform echoes in most of the comma head, and the more cellular precipitation on the southern and eastern edge of the comma-head.

Overall, the simulated cyclone was structurally similar on the large scale, but the center of the simulated cyclone was approximately around 300 km west when compared to the analysis. Several additional simulations were carried out in an attempt to simulate a storm that more closely matched the observed cyclone in evolution and location. Alternative advection schemes, different parameterizations, resolution and time step changes, and nudging were all tried to bring the simulated storm closer to the actual storm position, but these did not appreciably change the timing and track of the simulated storm. This simulation shown was the one that most closely represented the actual storm. This study focuses on the development of elevated instability and air parcel trajectories into the region of elevated instability. The importance of the elevated instability and antecedent airflows that produce that instability comes from their position relative to the cyclone, not relative to geography, so the position errors, as will become apparent, were not critical to addressing the questions regarding the generation of instability.

3.4 Convection and Potential Instability

3.4.1) Observed and Simulated Convection

Chapter 2 (see also Rauber et al. 2014) demonstrated that the cells observed in the 8-9 December cyclone have expected characteristics of elevated convection, including vertical velocities over 1 m s^{-1}, as well as graupel, charging, and lightning. The potential instability of the environment in the convective region of the comma-head of the cyclone was also observed with soundings. An example of one such sounding is shown in Figure 3.7. This sounding was launched near convective cells at 0400 UTC on 9 December. This particular sounding had 241 J kg^{-1} of MUCAPE, and four other soundings launched from the same location from 0000 UTC to 0800 UTC had positive MUCAPE values (Rauber et al. 2014). These observations of MUCAPE, combined with radar observations of convection, show the presence of potential instability in the

environment where the elevated convective cells were observed, the distribution of which will be examined below.

Figure 3.8 shows the WCR reflectivity and equivalent potential temperature from the analysis valid at 0300 UTC on 9 December. On the south side of the image, elevated convective cells are present extending from above the elevated boundary. The cells extend from 3-5 km altitude to the tropopause at around 8 km. These cells developed in an environment which was potentially unstable, with equivalent potential temperature values reaching a local maximum of 313-314 K just above the frontal boundary, decreasing to 311-312 K in the 6 to 7 km range, and then increasing again to the equilibrium level at the tropopause, with saturated air (with respect to ice) present in the layer at the top of the front.

The vertical cross-sections in Figure 3.8 are compared with the simulated reflectivity at 63 hours into the simulation to show that the simulation produced a reasonable representation (presence of instability, depth of unstable layer) of the convective region. Figure 3.9 shows a cross-section of θ_e contoured at every 0.5 K from the simulation across the convective region. As with the convection observed with the WCR, simulated convective echoes extend from above the elevated front at 2 to 3 km to the tropopause from 8 to 9 km. These narrow, tall echoes are convective in nature as they are located in the inner 3 km grid with explicit convection, and coincide with updrafts of 1 to 2 m s^{-1} in the model (see also section 3.6). These updrafts are smaller in magnitude than expected from Chapter 2, which is expected as convection is not adequately resolved at 3 km horizontal resolution. In addition, the convective cells exist in a potentially unstable environment, as is evident in the θ_e contours. The θ_e values reach a local maximum of around 314 K just above the elevated frontal boundary, which extends from 1.5 to 3 km (150 km to 450 km along the cross section horizontally) and decrease to a local minimum of

310 to 312 K in the 6 to 7 km range, similar to the analysis. The equilibrium level for parcels originating at the θ_e maximum is at the tropopause between 7 and 9 km, which increased in altitude from south to north.

3.4.2) Simulated Instability

At the surface, there is stable, cold air, as in the analysis (Fig. 3.8). Above the cold air, the vertical θ_e gradient tightens and stability increases in the 0.5 to 1 km range, also present in the analysis. The top of the uppermost front, indicated by the sharp decrease in potential stability, was located from about 1 km altitude in the south (x=450 km on Fig. 3.9) to about 5 km altitude in the north (x=0 on Fig. 3.9). Potential instability in the comma-head is based above this elevated frontal boundary.

The air above the elevated frontal boundary in the simulation consists of distinct layers, which are labeled in Figure 3.9. These layers were present in other cross-sections from the simulated storm taken ~100 km apart in space and 2 hours apart in time. The first layer, Layer A, lies above the front and represented warmer, moister air, and a θ_e maximum. This layer slants upward from 1.5 km altitude at the south to about 3.5 km at x=150 km. This maximum, with magnitudes around 314 K is consistent with the analysis (Fig. 3.8), and is where the instability is based. It is this air that ascends in convection in the simulation, a process examined in the next section.

Above layer A, lies a primary θ_e minimum, layer B (see Fig. 3.9). The minimum is located from about 2.75 km altitude in the south, slanting upward to about 4 km in the middle of the cross-section. θ_e within this layer ranged from 310 to 312 K. Above this minimum lies a secondary maximum, layer C, from about 3.75 km at the south to 4.25 km in the middle of the

cross-section. At the time of the cross-section, the secondary maximum in θ_e was not as large as the primary maximum, with the secondary maximum having magnitudes of 312 to 313 K, about 2 K less than the primary maximum. Above the secondary maximum was a secondary minimum, layer D, at an altitude of ~ 4.75 km to the south to ~7 km in the middle of the cross-section. Finally, the equilibrium level (layer E) was located from ~7 km to ~8 km altitude, where θ_e values again reach the same value as layer A, approximately 314 K.

In addition to the aforementioned layers, the signature of a convective cell is present at about x=150 km in Fig. 3.9. The effect of this cell on the background θ_e fields stands out. Instead of decreasing with height, θ_e is nearly constant with height due to upward transport of potentially warm air within the convection.

This convective cell can be seen in the simulated radar cross-section in Figure 3.9. The tall, cellular echoes reach up to the equilibrium level, with more stratiform echoes present in the stable air underneath the frontal boundary similar to cells observed with the WCR. The convective cells formed from the release of potential instability. The instability does not appear in the θ_e field overlain on the simulated radar reflectivity in the cells in Figure 3.9 because the cells have already released the instability, mixing air vertically. The convective cells and associated trajectories will be examined in more detail in section 3.5.

The potential instability from the cross-section can be seen in model soundings, an example of which is shown in Figure 3.10. While the instability in this sounding is not as pronounced as in the observed sounding owing to the smaller magnitude of instability in the model, there is still a clear layer of instability based at around 640 hPa up to an equilibrium level

near the tropopause at around 350 hPa, a layer of similar depth when compared to the observed unstable layer in Figure 3.9. The instability is based above the elevated boundary.

The region of elevated potential instability evolves in both location and magnitude with the cyclone in the simulation. Figure 3.11a shows a plan view of the column MUCAPE from the simulation, valid at 0000 UTC on 9 December 2009. The solid black contours are 10 dBZ contours of reflectivity from the simulation at the same time. Figure 3.11b shows the lifting condensation level (LCL) of the parcel with maximum column CAPE value indicated in Figure 3.11a. For elevated convection in the comma head, which begins at the top of the stable layer with saturated air, as shown in the sounding in Figure 3.10, the Lifted Condensation Level (LCL) will correspond to the Level of Free Convection (LFC). At this time, precipitation was located across Illinois, Missouri, and Indiana, and the model indicated potential instability coincident with this precipitation in the southern part of the comma-head (Fig. 3.11), with MUCAPE values around 47 J/kg in northeast Missouri. The MUCAPE across northern Missouri, southern Iowa, and central Illinois was based in the 2.5 to 4.5 km range, which is consistent with the altitude of Layer A in Figure 3.9**.**

By 0300 UTC on 9 December, the MUCAPE across southern Iowa increased, with the maximum in MUCAPE reaching 93 J kg^{-1} (Fig. 3.13c). This potential instability increase happened within the precipitation on the south side of the comma-head, as indicated by the 10 dBZ contour in Fig. 3.11c. Figure 3.13d shows that this instability is once again elevated, with parcels with MUCAPE values having LCLs generally in the 3 to 4 km range across southern Iowa and central Illinois, consistent with the altitude of Layer A on Figure 3.9 and the sounding in Figure 3.10.

3.5 Trajectory analysis

Backwards trajectories are used in this section to establish the history of air in the potentially unstable layer. The goal of this analysis is to understand the thermodynamic history of air that led to the pre-convective environment which supported elevated convection in the comma-head. Trajectories shown here are from each of the layers indicated on Figure 3.9. The cross-sections where the trajectories were released (Fig. 3.2) lie across the MUCAPE maxima in Figure 3.11a and c. The trajectories arriving within each of the layers (A-E) had similar sources. The source points for trajectories arriving in each layer appears in Figure 3.12. The numbers near the star indicate the altitude from which the backwards trajectory was released. The trajectories are plotted for every five gridpoints, 45 km apart, in the north-south direction. In Figure 3.12a, the source points are for trajectories released from the eastern cross-section on Figure 3.2 at 0300 UTC. Air arriving in layer A originated over the eastern Pacific near Baja California (region A on Fig 3.12a), with the exception of one location over north-central Mexico, and originated at altitudes from 2.25-2.75 km altitude. Layer B air originated to the northwest in region B on Figure 3.12a, between 2.2 km and 3 km altitude. Layer C was smaller in horizontal extent, so there are fewer trajectories, but these trajectories originated in region C on Figure 3.12a, north of those in Layer B, at altitudes from 2.75 km to 4.5 km. Layer D air originates in region D on Figure 3.12a over northwest Canada at 8.5 km to 9.25 km altitude, and the air arriving in Layer E originated from two points within region E on Figure 3.12a, so only two source points are shown on the map. This air originated from 9.25 km to 9.75 km altitude..

Overall, the juxtaposition of air from over the subtropical Pacific and Arctic, such that air from regions A-E all arrive and arrange into the layers in Figure 3.9, creates potential instability in the comma-head. In this storm, air from the Gulf of Mexico or central Plains was not

incorporated into the layer where the instability occurred. It is notable that air within layers A and E originated at locations up to 5000 km apart 63 hours before arriving in the comma-head.

Figure 3.12b, 3.12c, and 3.12d are plots of trajectory endpoints, as in Figure 3.12a, except the panels are all for trajectories released at 0100 UTC. Figure 3.12b is for trajectories on the westernmost cross-section in Figure 3.2, Figure 3.12c is for the middle cross-section, and Figure 3.12d is for the easternmost cross-section.The trajectories from 0100 UTC are examined because the model had fewer convective cells present at that time. All three 0100 UTC cross-sections are similar to the 0300 UTC cross-section, with Layer A air originating near Baja California, and subsequent layers of air originating further north and west in similar locations and altitude to the 0300 UTC cross-section. The most notable difference is in Fig. 3.12b, the west cross-section at 0100 UTC, where there was no signal of Layer C, as a large, nearly neutral layer separated Layers B and D (not shown).

Fig 3.13 shows backwards trajectories released at 0300 UTC on 9 December along the easternmost cross-section on Figure 3.2. An example trajectory from each of the layers in Figure 3.9 appears on Figure 3.13. The example trajectories on Figure 3.13 show plan views colored by pressure (left column), and as a time series of key parameters along with the trajectory altitude in the right column. The trajectories presented in Figure 3.13 are representative of other trajectories in their respective layers.

Altitude (m, blue), terrain height (m, brown), potential temperature, (K, black), equivalent potential temperature, (K, green), and mixing ratio (g kg^{-1}, red) appear on Figure 3.13b,d,f,h,j. In the absence of diabatic processes, θ, θ_e, and q are conserved. The assumption that diabatic processes do not appreciably affect elevated airstreams and thus air flows adiabatically

through the free atmosphere is a common one and forms the basis for isentropic analysis and isentropic charts (Uccellini 1976).

Figure 3.13a shows a trajectory from within Layer A. Air arriving in Layer A would be the source air for convection in the comma-head. The trajectory began at hour zero directly south of Baja California at 2250 m altitude. Air following this trajectory moved northeast, going over continental Mexico, and it reached the Rio Grande valley by hour 36, where the air's forward speed increased, indicated by the trajectory's arrival in north Texas by 48 hours, and it reached eastern Missouri by 60 hours before the air arrived at the cross-section at 63 hours.

The thermodynamic evolution of the air appears on Figure 3.13b. The air began at hour zero around 2.5 km altitude. The air maintained roughly the same altitude until encountering higher terrain of the Sierra Madre Occidental mountains, which forced the air to ascend over the terrain to 3.5 km at time α (Fig. 3.13b), where mixing with clouds and precipitation increases q by 1.5 g kg^{-1} while θ_e increased by 5 K. The air then descended on the far side of the terrain at time β to around 1.5 km, mixing in cooler and drier air as q decreased 1 g kg^{-1}, and θ and θ_e decreased by about 5 K each. After this, the air slowly descended and cooled until time γ. At time γ, the air encountered clouds and precipitation behind a front located across eastern Texas, where evaporative cooling in stratiform clouds behind the front decreased θ and θ_e by 7 K while q increased by 1.5 g kg^{-1}. Finally, at time δ, the air ascended 1000 m within the comma-head, where it precipitated out 2 g kg^{-1} of moisture, while θ increased by 5 K and θ_e remained constant due to pseudoadiabatic ascent.

Both θ and θ_e steadily decrease during most of the trajectory time series in Figure 3.13b. This decrease, which is around 1-2 K per day, is consistent with the expected range of radiational cooling rates in the atmosphere (c.f. Cavallo et al. 2011, Fig. 1b). This cooling was observed in

every trajectory examined, including the other ones presented here. Between radiational cooling and other diabatic processes, over the length of the trajectory in Figure 3.13b, the air's θ_e value decreased from 323 K to 314 K. Despite this decrease, the air arrived at the cross-section in the layer with a local maximum, and became the source air for convection.

Layer B consists of trajectories similar to the example shown in Figure 3.13c. This trajectory begins over the Pacific Ocean in region B in Figure 3.12a, starting at 2900 m altitude. As with the previous trajectory, air moved across northern Mexico, and accelerated after 36 hours as the air encountered stronger flow, reaching west Texas by 48 hours and central Missouri by 60 hours.

The air along this trajectory slowly descended from its 2900 m starting altitude, and cooled diabatically as it moved in Figure 3.13d. This diabatic cooling was evidenced by a 2 K decrease in both θ and θ_e over the first 30 hours. At time α, the air was mixed with surrounding higher moisture air, evidenced by the 0.5 K increase in θ_e and a 0.1 g kg^{-1} increase in q. This mixing was induced by crossing the higher terrain of Baja California. At time β, the air encountered the Sierra Madre Occidental mountains, which forced the air to rise 1000 m. As it rose, the air mixed in potentially warm air, increasing θ by 1K. This mixed-in air was associated with precipitation on the windward side of the mountains, so the air gained 4 K in θ_e as well as 1.4 g kg^{-1} in q. On the other side of the mountain, θ decreased by 1 K, but θ_e held roughly steady as q increased by another 0.1 g kg^{-1}. The air then held steady in altitude until time γ, where the air ascended 1000 m in the comma-head region. As it did so, the conservative parameters remained essentially constant until the last hour, where the air gained 0.2 g kg^{-1} in q while θ decreased by 0.5 K due to evaporational cooling.

For Layer C in Figure 3.13e, the source region at hour zero was farther northwest over the Pacific Ocean than Layer B with air starting at 3500 m altitude, but the trajectory otherwise followed a similar path once it reached land, though it was moving faster owing to being further aloft by about 500 m. Over the first 40 hours, the air slowly descended 500 m and radiationally cooled (Fig. 3.13f), with gradual changes of 0.1 to 0.2 g kg^{-1} in q.

At time α, the air moved over the higher terrain of Baja California, which caused a 0.4 g kg^{-1} decrease in q, with a 1 K increase in θ and a 1 K decrease in θ_e, all of which is due to mixing. At time β, the air then moved over the Sierra Madre Occidental mountains, which again induced mixing. This time, q increased by 0.4 g kg^{-1}, and θ_e increased by 1 K. At time γ, air ascended 1000 m and mixed with drier air in the comma-head, decreasing q by 0.9 g kg^{-1} while θ_e decreased by 2 K as the air arrived at the comma-head. This mixing occurred due to the air ascending through a region of lower RH values aloft.

A trajectory characteristic of Layer D is shown in Figure 3.13g. Air in this layer originated in northern Canada at model hour 8 (due to being outside the domain at hour 0), near 9 km altitude (Fig. 3.13h). The air in this layer moved quickly around the base of the longwave trough, ending up off the coast of Oregon by 24 hours, off the coast of central California by 36 hours, over southeast Arizona by 48 hours, and over southwest Missouri at 60 hours before it arrived at the cross-section in the comma-head by 63 hours.

In Figure 3.13h, the air from Layer D began near 9 km altitude, and then it cooled diabatically by about 2 K in θ and θ_e over about 40 hours as it descended by almost 5000 m. During this decent, q remained constant. At time α, the air was at around 4 km altitude and moved over the Rocky Mountains. This caused the air to mix with its surroundings, which

consisted of clouds and precipitation near the base of the longwave trough. This mixing increased θ by 1 K and θ_e by 2 K, with q increasing by 0.4 g kg^{-1}. After crossing the mountains, the air again radiationally cooled by about 1 K in θ and θ_e until time β, when q increased by 0.2 g kg^{-1} in the last hour due to mixing/evaporational cooling in the comma head, which accelerated the ongoing decrease in θ with time, but caused θ_e to stop decreasing.

Air from Layer E also originated over northern Canada, west of the air from Layer D (Fig. 3.13i) at 9.5 km altitude and model hour 20. As with the previous layer's air, air from Layer E moved rapidly around the base of the longwave trough, where it was located off of Oregon at 36 hours, over southeastern California by 48 hours, over the Kansas/Missouri border at 60 hours, and arriving at the cross-section at 63 hours.

From its starting altitude of 9.5 km in Figure 3.13j, the air was mixing due to the influence of the Canadian Rockies until 32 hours, after which the air cooled radiationally and slowly descended. This happened until time α, when the air crossed over the Rocky Mountains again, causing mixing and small fluctuations in q, θ, and θ_e. After crossing the mountains, the descent stopped and the air began to rise towards 7.5 km, with θ and θ_e again decreasing due to diabatic cooling and q remaining constant.

3.6 Convective cells

The trajectories in the previous section examined source air for an environment in which instability had yet to be released. In this section, air passing through active convective cells is examined. Several convective cells can be seen in Figure 3.14, which is a cross-section in the same location of Figure 3.9, but showing vertical velocity. These convective cells are on the left side of the cross-section between 0 and 200 km, with vertical velocities in the cells reaching over

1 m s^{-1}. These vertical velocities are below the observed velocities from this case (Rosenow et al. 2014), which is expected due to the model resolution being insufficient to fully resolve the convection.

Figure 3.15 shows a plan view and time series of a trajectory ending at 6.25 km at the black dot within the developed cell in the convection in Figure 3.9 and Figure 3.14. At this altitude south of the convection in Figure 3.14, air parcels lie in Layer D and originated in northwest Canada. However, Figure 3.15a shows that the air parcel arriving at point F originated near Baja California, the origin for parcels in Layer A. Like Layer A in Figure 3.13a, air from this convective cell moved northeast over Mexico, Texas, Oklahoma, and Missouri before arriving at the cross-section (Fig. 3.15a).

In Figure 3.15b, the evolution of the parcel is similar to the evolution of the Layer A air in Figure 3.13b, with the air starting out at around 2500 m. At time α in Figure 3.15b, the air crossed the Sierra Madre Occidental and encountered the same windward clouds and precipitation as air from Layer A did, which here caused a 3 K increase in θ_e, a 1.5 g kg^{-1} increase in q, and a 2 K decrease in θ. On the other side of the mountains, the conservative variables cooled radiatively until time β, where the air encountered the post-frontal precipitation, which induced evaporative cooling, including a 0.5 K increase in θ_e, a 1 g kg^{-1} increase in q, and a 2 K decrease in θ by hour 40. After that, having descended only 500 m through time γ, the air began to rise into the comma-head region, mixing with the saturated air aloft, increasing θ by 3 K, θ_e by 2 K, and q by 1 g kg^{-1}. At this point, the air begins to rise rapidly through the potentially unstable layer at time δ, gaining 3000 m altitude in under an hour and rapidly loses moisture due to precipitation during pseudoadiabatic ascent, as q decreased by 3.5 g kg^{-1}. Because the ascent is pseudoadiabatic, θ increases by 4 K, but θ_e remains essentially unchanged.

3.7 Summary

In this chapter, the distribution and formation of potential instability in the comma-head region of a strong continental cold-season cyclone was examined. A WRF simulation was presented to simulate convection in the comma-head region of a strong continental winter cyclone while providing a sufficient domain to calculate parcel origin. The presence of elevated potential instability in the model was demonstrated, which compared favorably with observations of the actual cyclone. The favorable comparison provides confidence that the simulation can be used to demonstrate how the environment for elevated convection forms.

Trajectory analysis presented in this chapter shows that potential instability, at least in this cyclone, formed by the vertical arrangement of air from sources up to 5000 km apart, with the base of the potentially unstable layer sourced near Baja California or over continental Mexico and the air at the top of the potentially unstable layer sourced in the Arctic. Notably absent from the potentially unstable layer is any air from the Gulf of Mexico region. Air from over the Gulf was confined to the area in the stable layer below the elevated boundary.

As the air transits from these diverse sources to the comma-head region, the air undergoes significant diabatic changes. One of the dominant effects on the thermal characteristics of the air as it moved was the effect of longwave cooling. This longwave cooling effect, a loss of 1-2 K per day, was seen across all trajectories, regardless of differing starting altitudes and air properties. This result suggests that using an adiabatic framework to examine atmospheric motions outside of short time scales is likely to result in significant error.

In addition to diabatic effects, other prominent changes in conservative parameters along trajectories were due to terrain influences. As the air in the unstable layer is sourced over the

Pacific or northwestern Canada, any path to the Midwestern US must cross a mountain range, such as the Rocky Mountains or the Sierra Madre Occidental. As the air crosses these mountains, fluctuations of 1-3 K (in some cases, 5 K or more) occur in θ and θ_e as the air is mechanically forced to rise and encounters turbulence above the mountains, mixing with other air and potentially passing through orographic clouds.

Despite these large changes in thermodynamic properties, this analysis shows that air was ultimately organized into a potentially unstable layer in the comma-head consisting of five distinct layers. The production of instability occurred as air in these layers took different geographic paths to be arranged in the vertical with θ_e decreasing with height, even though θ_e changed by 5 K or more as the air was in transit to the comma head. It was the arrangement of airmasses that ultimately was responsible for the instability in the comma-head region.

The results presented here are from one cyclone. Future research using additional cyclones will show whether the findings of this study can be generalized to other strong continental cyclones. Similar work on weaker cyclones with weaker instability and/or a lack of observed convection would also be useful to understand what causes these stronger cyclones to produce more instability and convection than weaker storms.

3.8. Table

WRF Parameter	Setting(s)
Run Time	3 days, 18 hours
Initialization Time	6 December 2009 at 1200 UTC
Output Interval	5 minutes
Time Step (Outer Domain)	20 seconds
Number of Domains	2
nx, ny	Domain 1: 1002,712; Domain 2: 988,907
Vertical Levels	120
dx, dy	Domain 1: 9 km; Domain 2: 3 km
Domain x,y Start	457, 179
Microphysics Option	8 (Thompson Microphysics)
Radiation LW/SW Physics	4 (RRTMG Scheme)
Radiation dt	5 minutes
sf_sfclay, sf_surface Physics	1, 2 (Monin-Obukhov, Noah LSM)
Boundary Layer Scheme, dt	1 (YSU scheme), every time step (0)
cu_physics, cudt	Domain 1: 1 (Kain-Fritsch), 5 minutes; Domain 2: 0 (explicit convection)
damp_opt	3 (Rayleigh damping)
Zdamp	5000 m
epssm	0.5
h,v Advection Order	5^{th} Order
Time Step for Sound	6 seconds
Moist, Scalar, Chem Adv.	4 (5^{th} order WENO)

Table 3.1: Non-default WRF settings used for the simulation

3.9. Figures

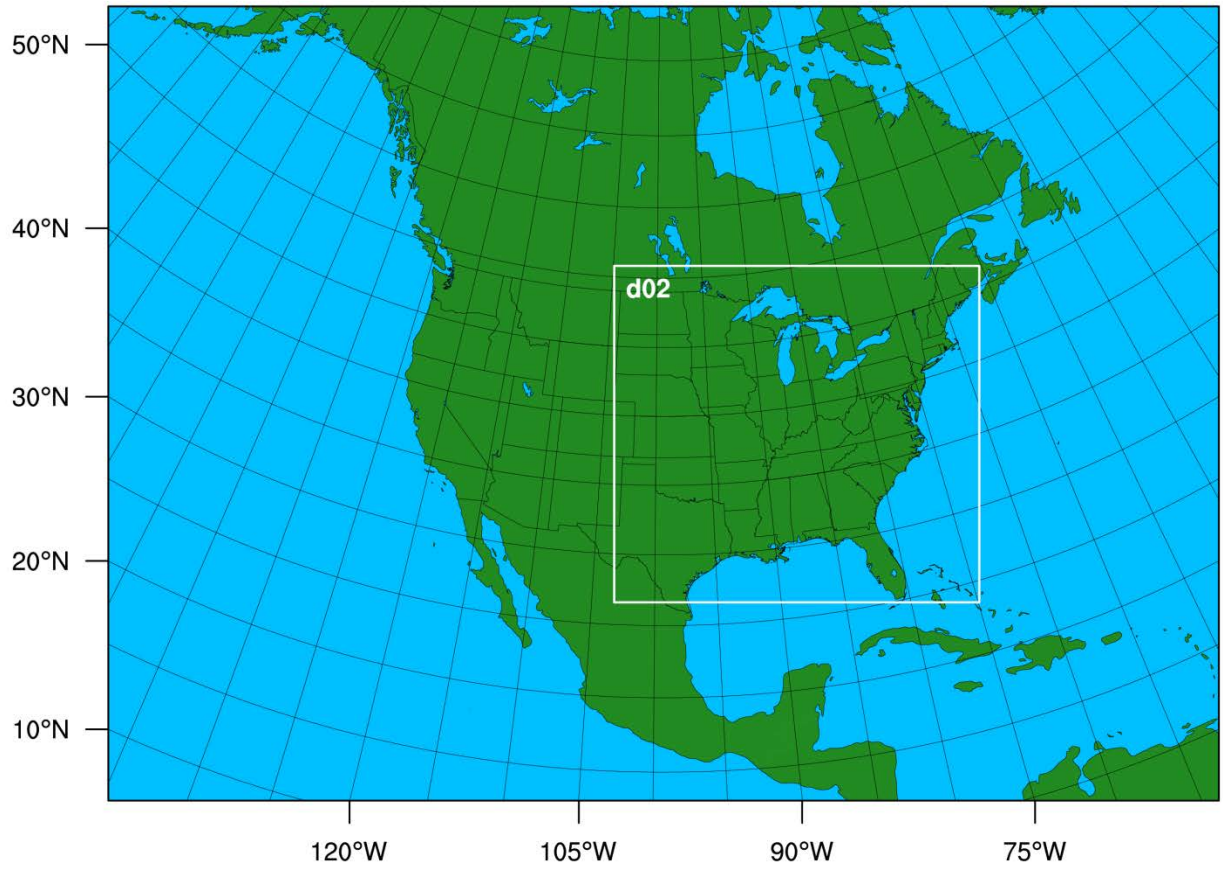

Figure 3.1: Domains used in the simulation. The entire map represents the size of the outer domain, and the white box represents the size of the nested domain.

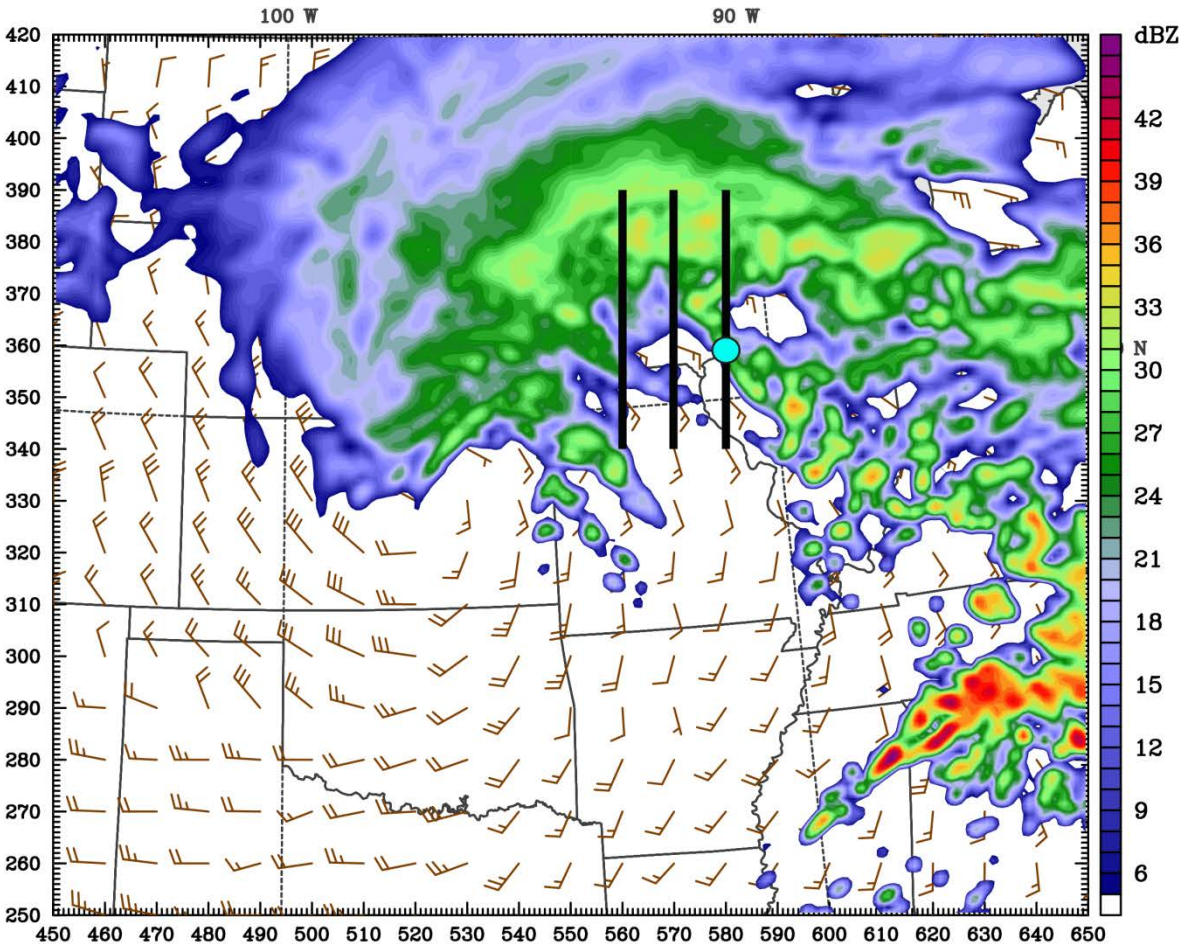

Figure 3.2: WRF Simulated radar reflectivity (colors) and surface wind barbs (knots) valid at 0300 UTC on 9 December 2009. Black lines indicate location of z-y cross-sections where back trajectories were released. Cyan dot indicates sounding location in Figure 3.10. Axis labels on bottom and left side indicate model grid point number (nx=ny=9km).

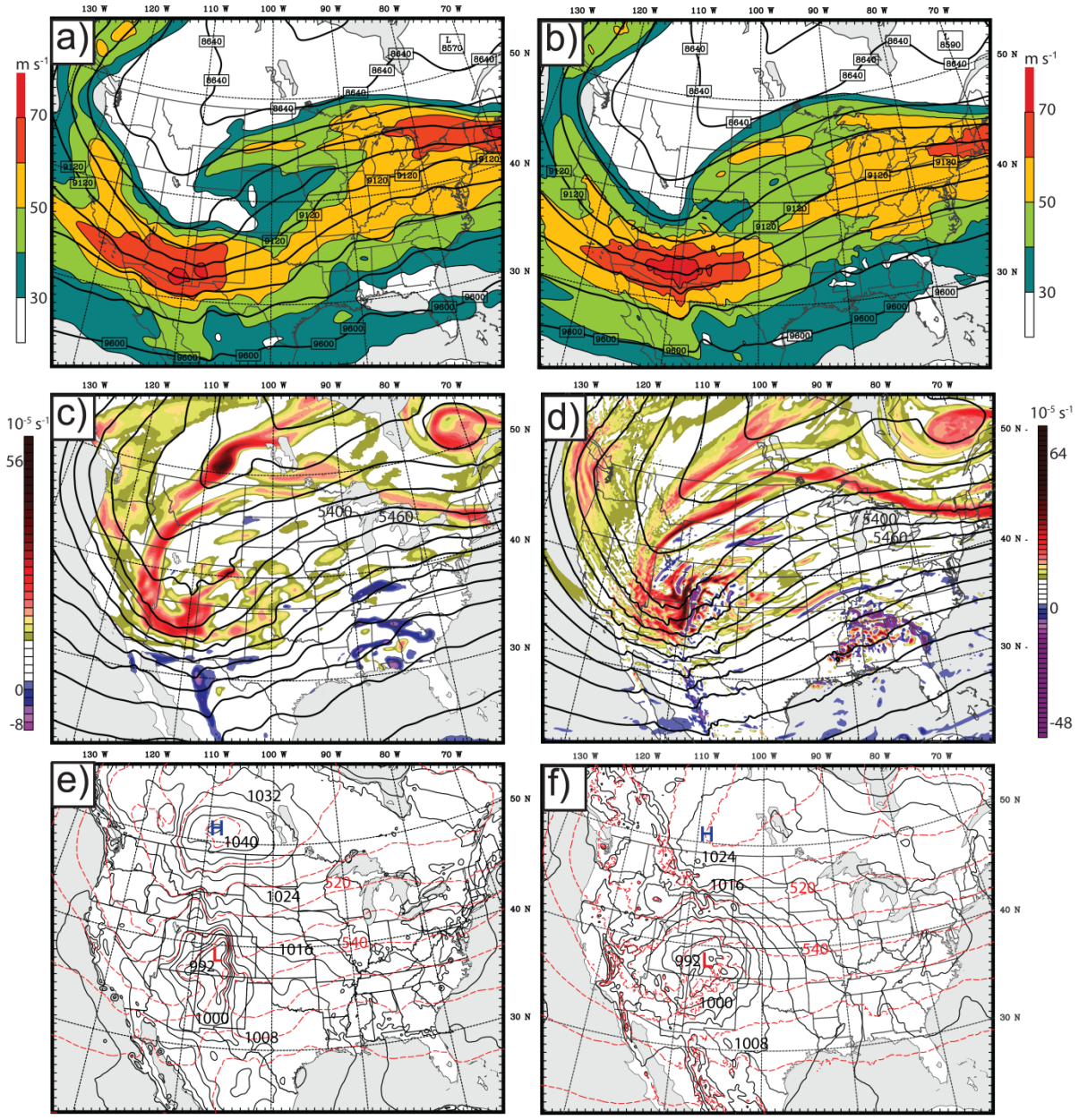

Figure 3.3: Synoptic plots valid at 1200 UTC on 8 December 2009 from the RUC initialization (a, c, e) and the WRF run (b, d, f). Plots are: a), b): 300 hPa heights (contours, m) and winds (colors, m/s); c), d): 500 hPa heights (contours, m) and relative vorticity (colors,10^5 s^{-1}); e), f): mean sea level pressure (solid contours, hPa) and 1000-500 thickness (red dashed contours, dm).

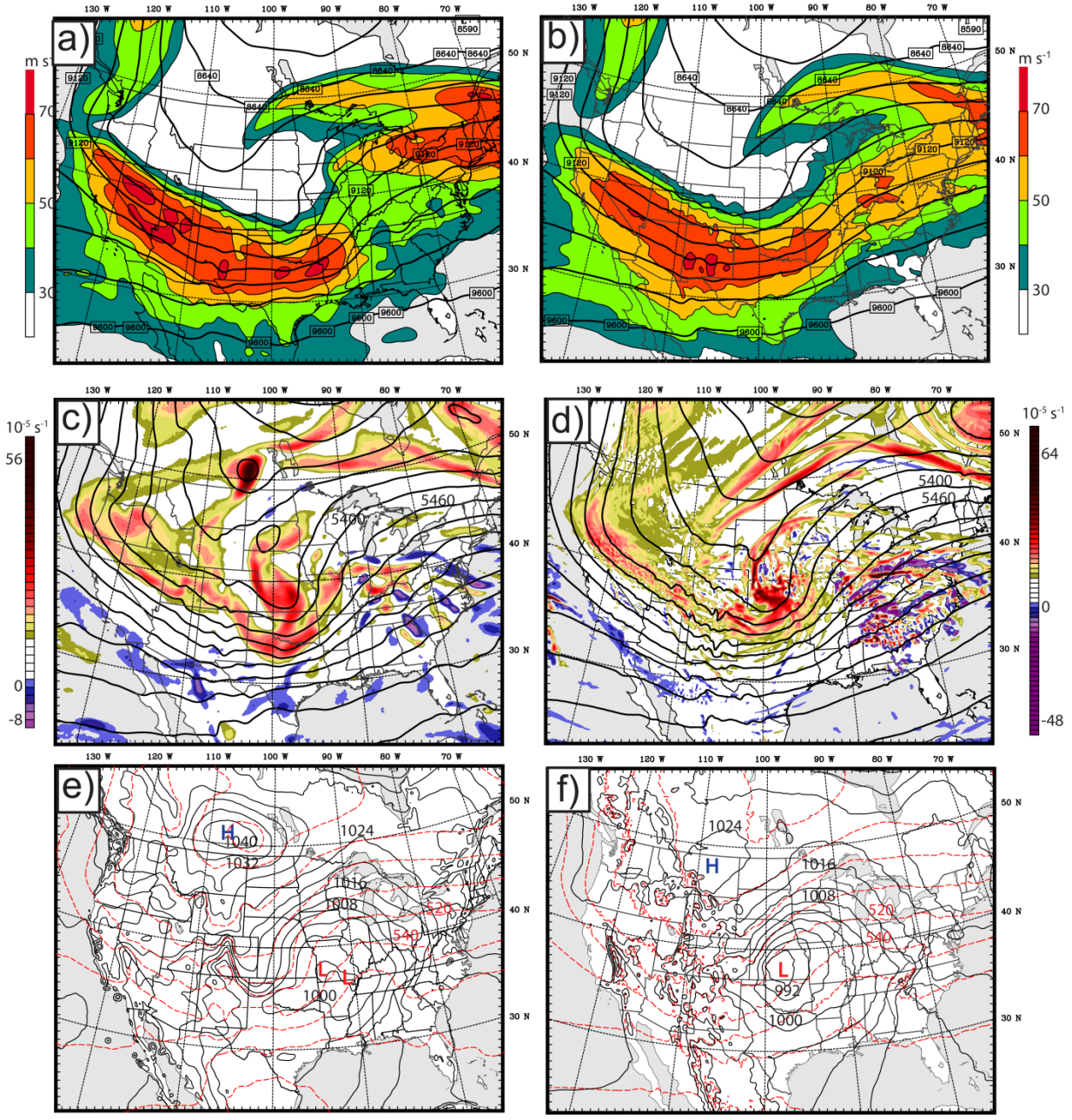

Figure 3.4: As in Figure 2, but for 0000 UTC on 9 December 2009.

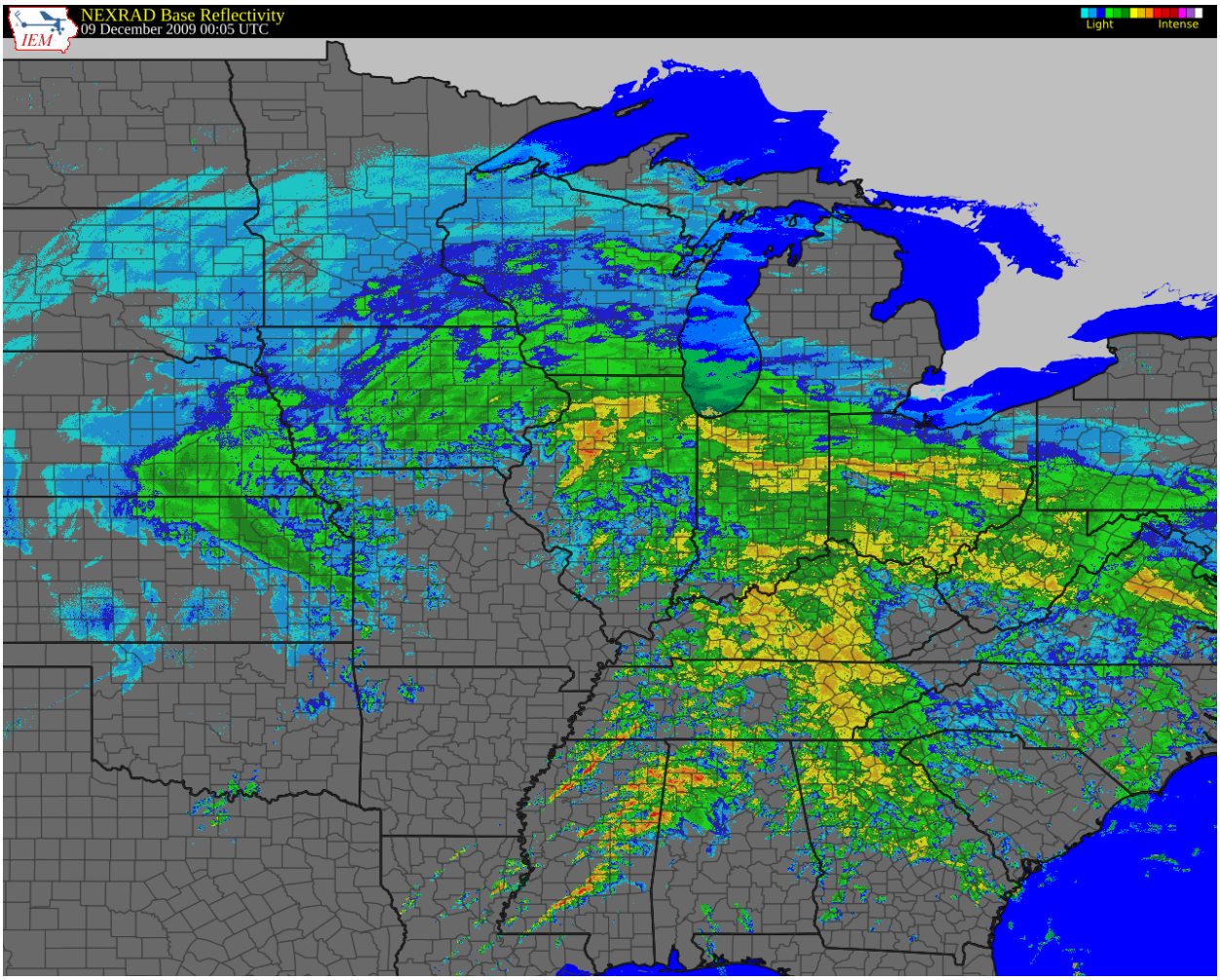

Figure 3.5: WSR-88D radar reflectivity composite for 0005 UTC on 9 December 2009.

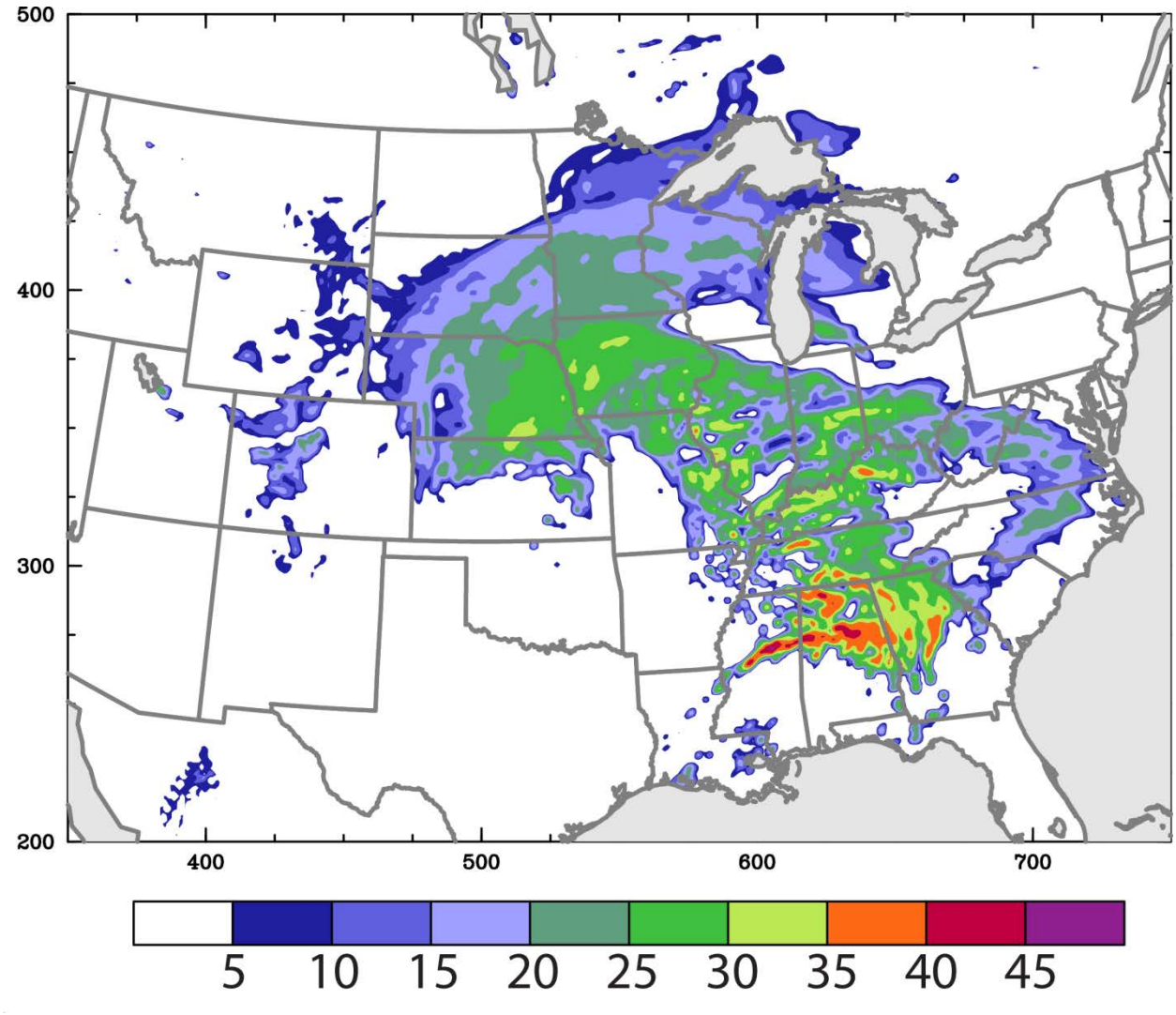

Figure 3.6: Simulated radar reflectivity valid at 0000 UTC on 9 December 2009. Axis labels indicate model grid point number (nx=ny=9 km).

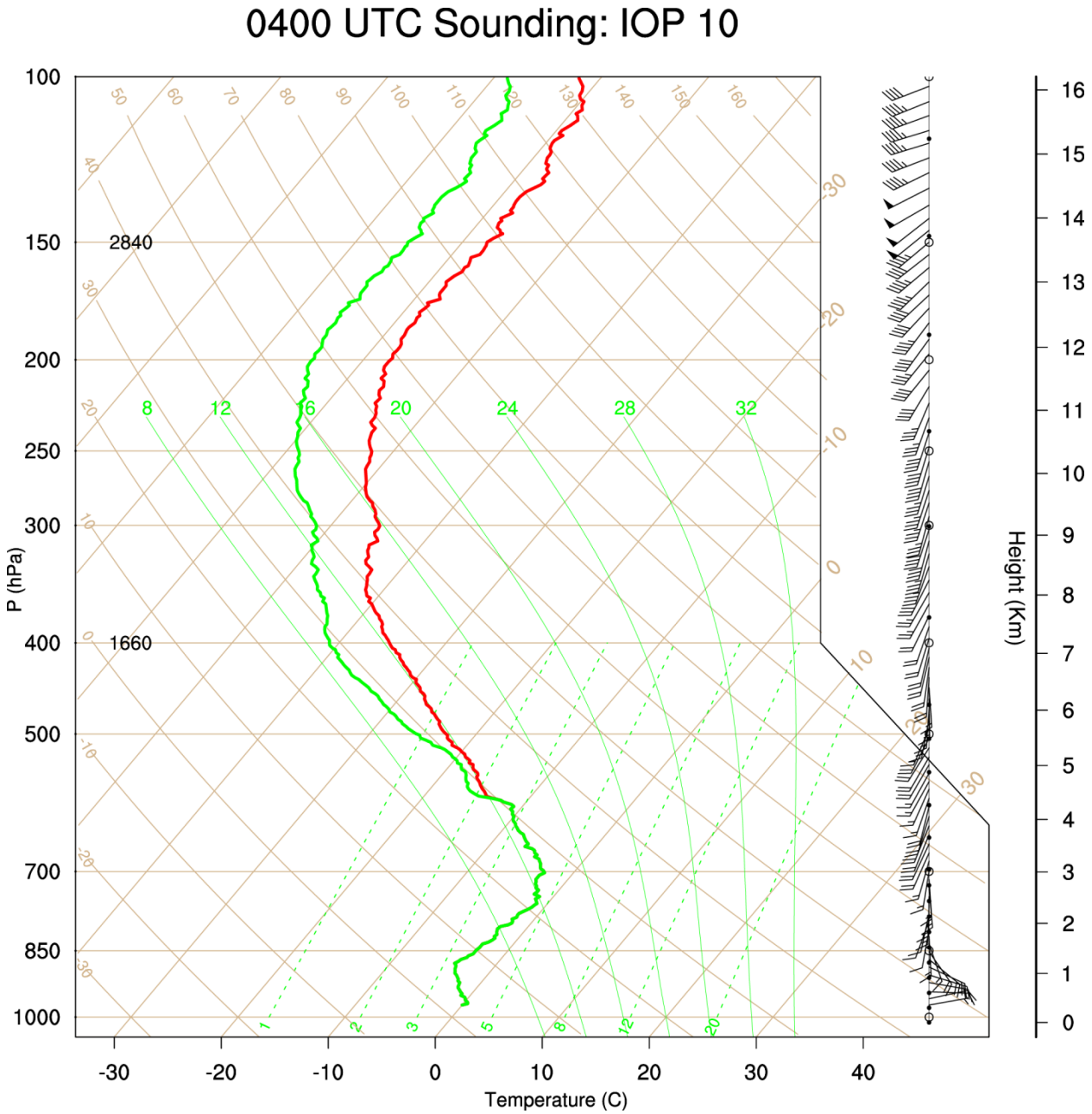

Figure 3.7: Observed 0400 UTC special sounding taken from Clinton, IA in the convective region of the cyclone on 9 December 2009. Winds are in m s^{-1}.

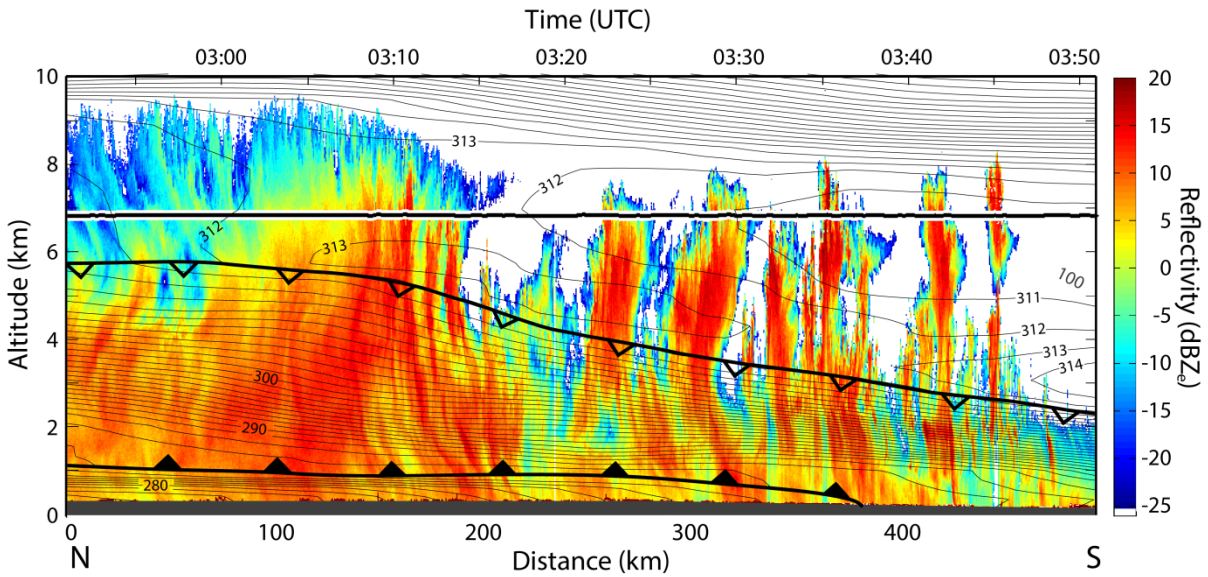

Figure 3.8: Wyoming Cloud Radar reflectivity and RUC θ_e with respect to ice from a cross-section of the 9 December cyclone indicated on Figure 2.5. Adapted from Rosenow et al. (2014).

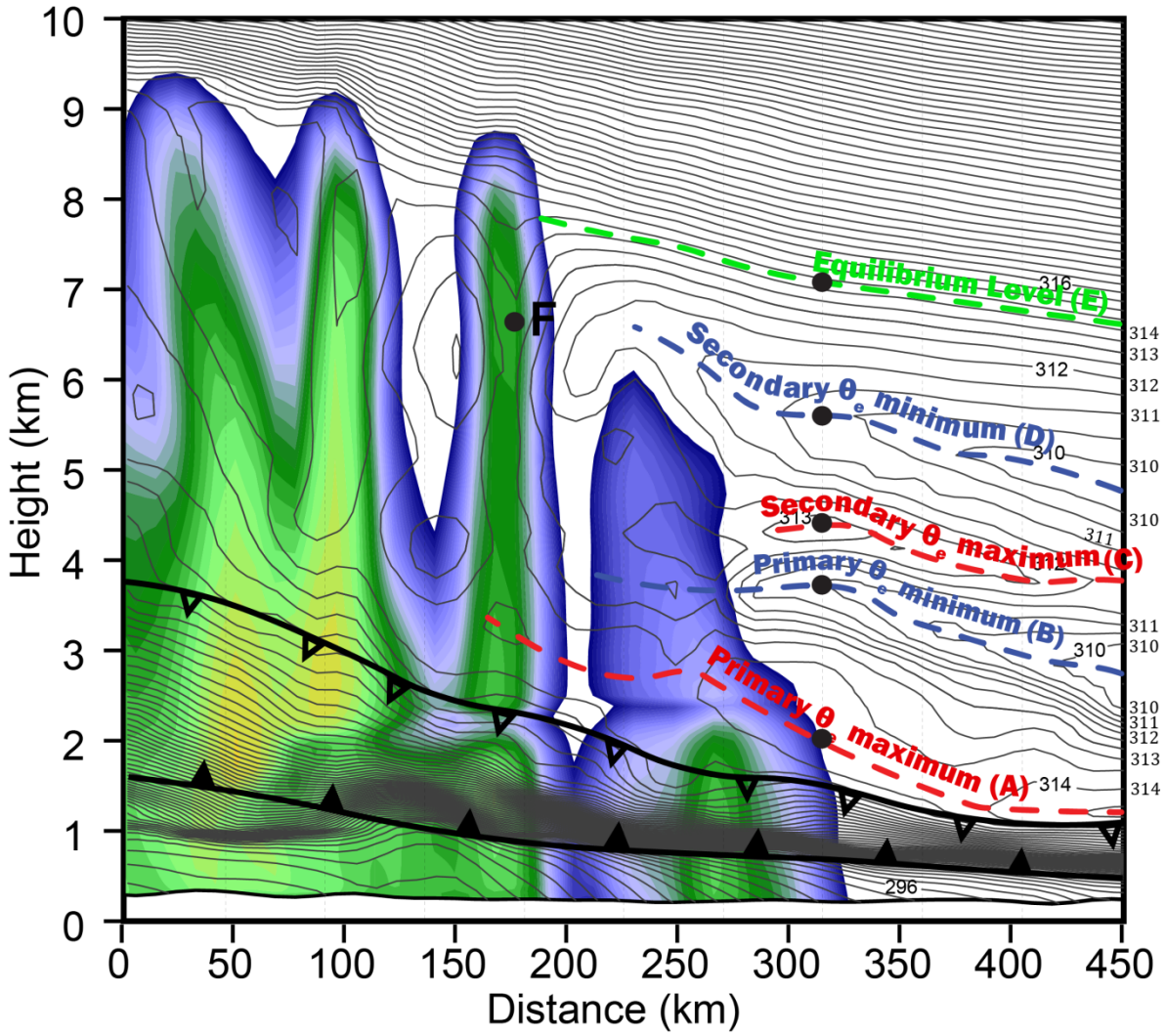

Figure 3.9: Simulated radar reflectivity (colors) and θ_e (contours) from the easternmost cross-section in Figure 3.2 at 0300 UTC on 9 December. Dashed colored lines indicate distinct labels in the convective region; letters in parentheses indicate layer name used throughout the paper. Black dots at x=325 km indicate trajectory locations in Fig. 3.13. Black dot labeled "F" is for the trajectory in Fig. 3.15.

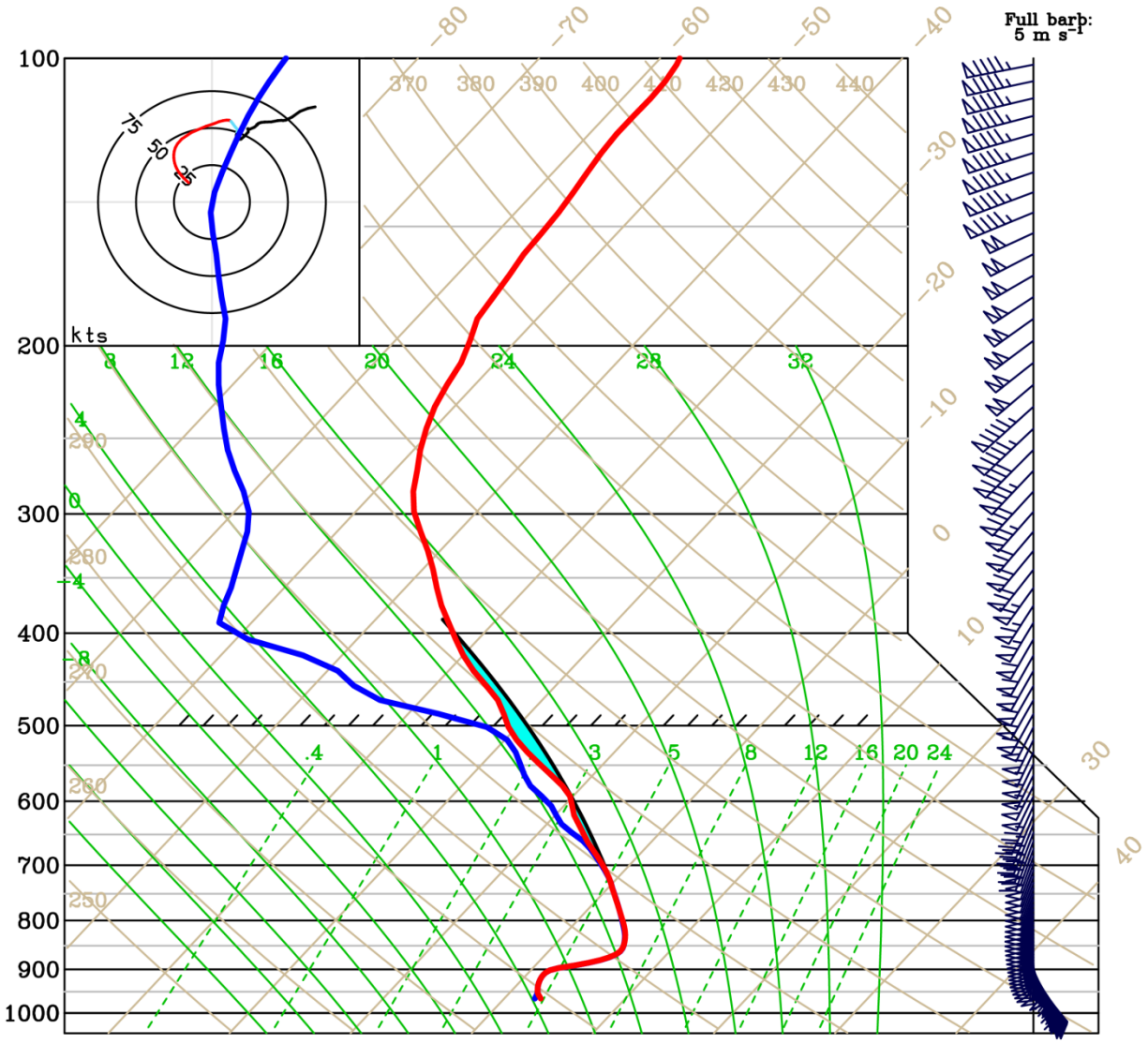

Figure 3.10: WRF model sounding from within the convective region of the cyclone at the point indicated on Figure 3.2 at 0300 UTC on 9 December 2009. Red line is temperature, and blue line is dew point temperature. Winds are in m s^{-1}. Black line indicates most unstable parcel path, and cyan fill indicates positive area (buoyancy) for MUCAPE parcels.

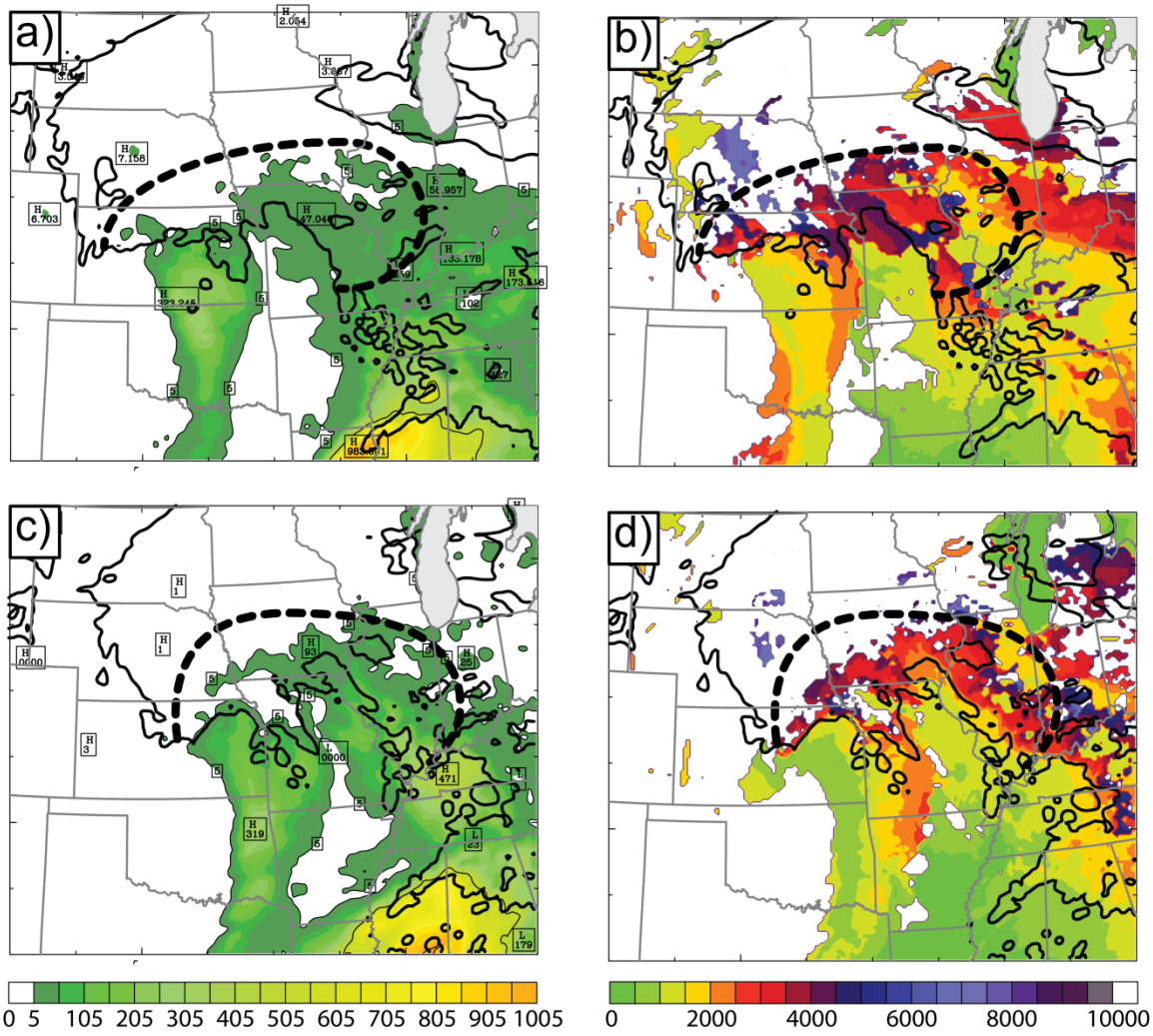

Figure 3.11: a,c): Simulated column maximum CAPE (colored) and 10 dBZ simulated reflectivity contour (black) from the WRF run, and b,d): the LCL of the parcel with maximum MUCAPE. Plots are valid at: a,b) 0000 UTC 9 December; c,d) 0300 UTC 9 December. The bold dashed lines enclose the approximate location of the convective region.

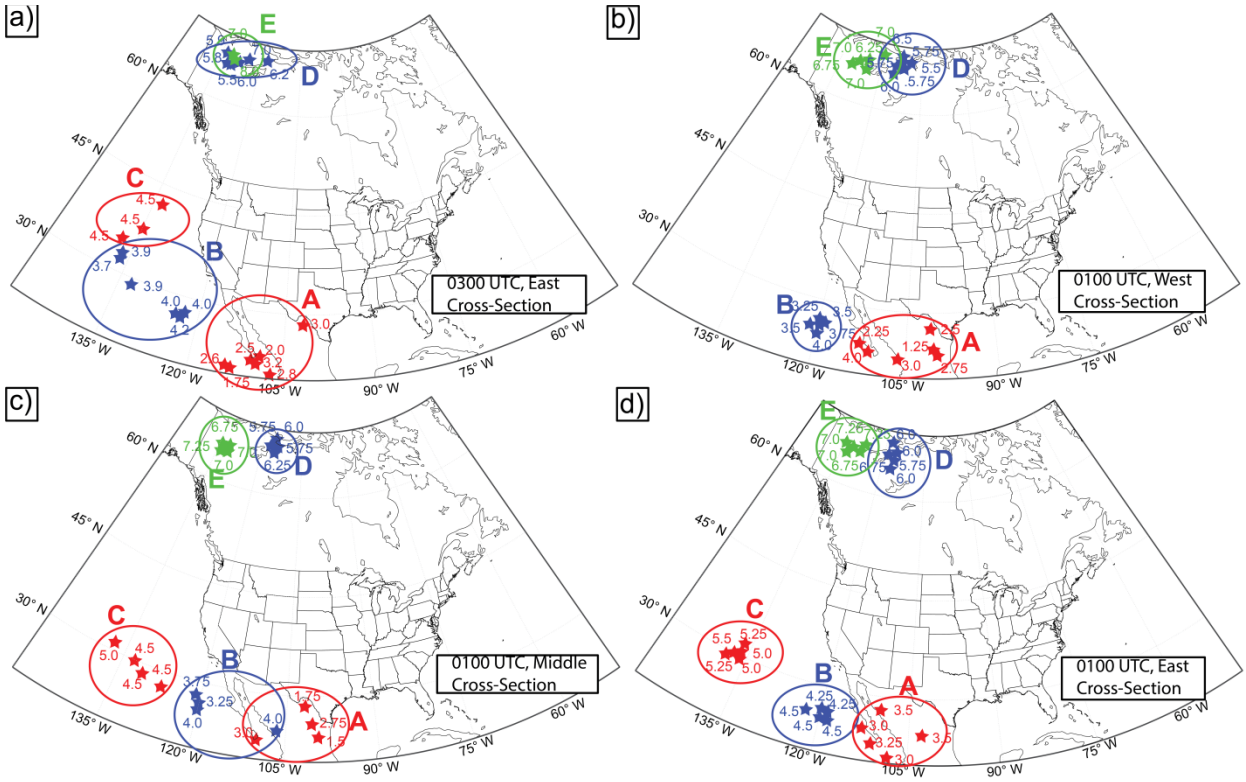

Figure 3.12: plots of source locations for each of the layers in Figure 3.9. Maps are for trajectories from a) 0300 UTC 9 December, easternmost cross-section in Figure 3.2; b) 0100 UTC 9 December, western cross-section in Figure 3.2; c) 0100 UTC 9 December, central cross-section in Figure 3.2; d) 0100 UTC 9 December, eastern cross-section in Figure 3.2.

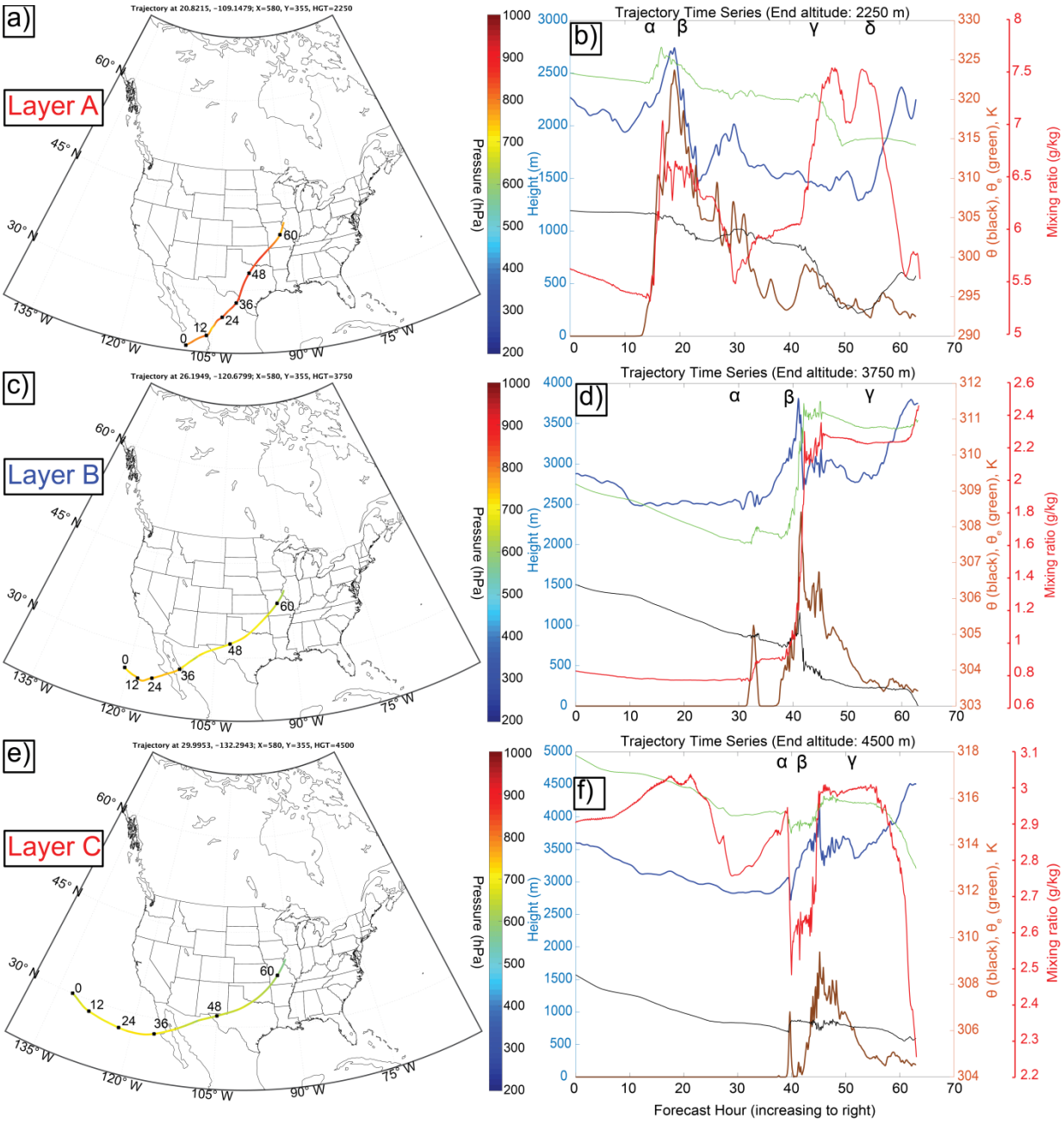

Figure 3.13: Trajectory examples from each of the layers in Figure 3.9. Trajectories all arrive at the same geographic location on the easternmost cross-section on Figure 3.2, but at different altitudes. Left column: Plan view of trajectories with model forecast time indicated every 12 hours. Trajectories are colored by pressure. Right column: time series of trajectory height (m, blue, left axis), height of terrain under trajectory (m, brown, left axis), equivalent potential temperature (K, green, right axis), potential temperature (K, black, right axis), and mixing ratio (g kg^{-1}, red, far right axis). Trajectories are from: a,b) Layer A; c,d) Layer B; e,f) Layer C; g,h) Layer D; i,j) Layer E. Greek letters indicate times of interest referenced in the text.

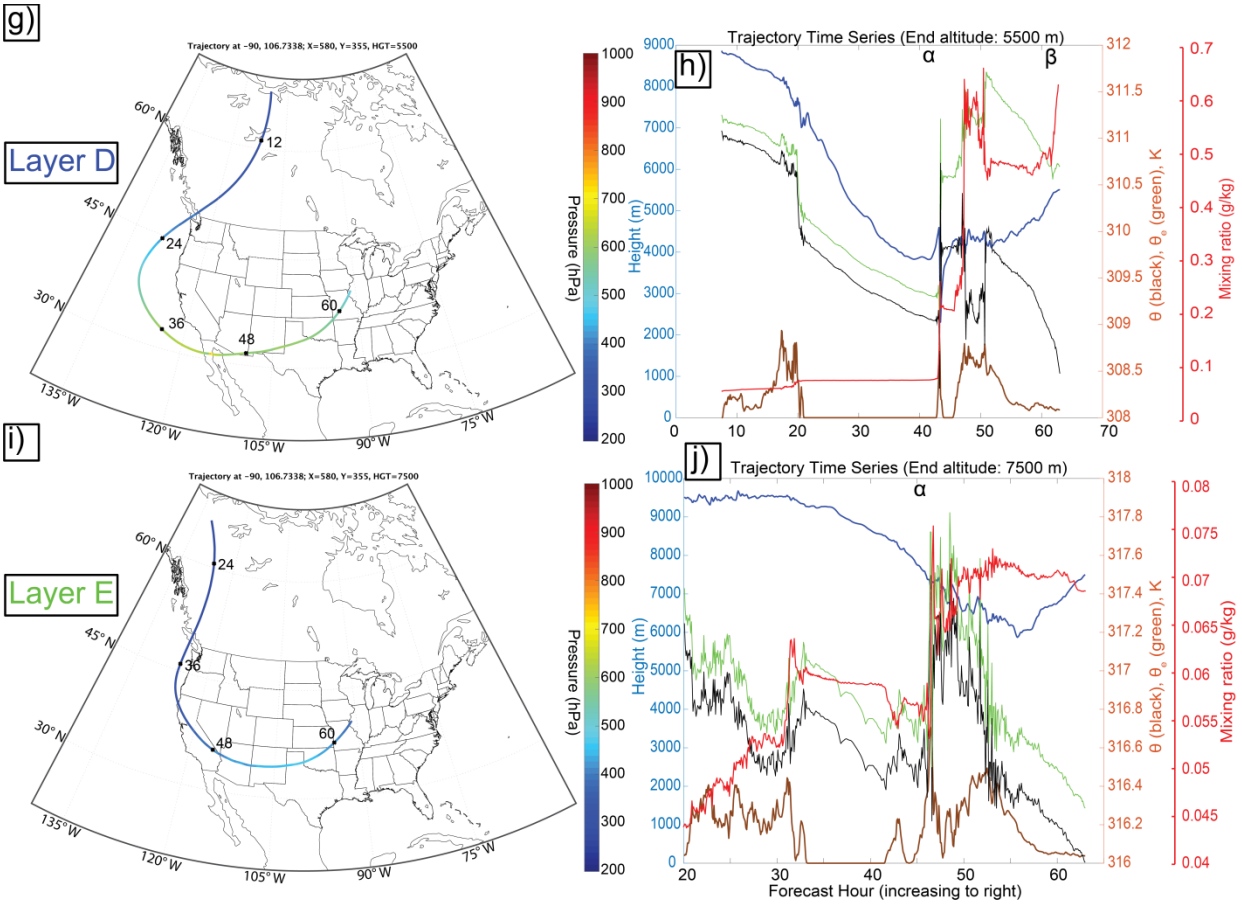

Figure 3.13 (continued)

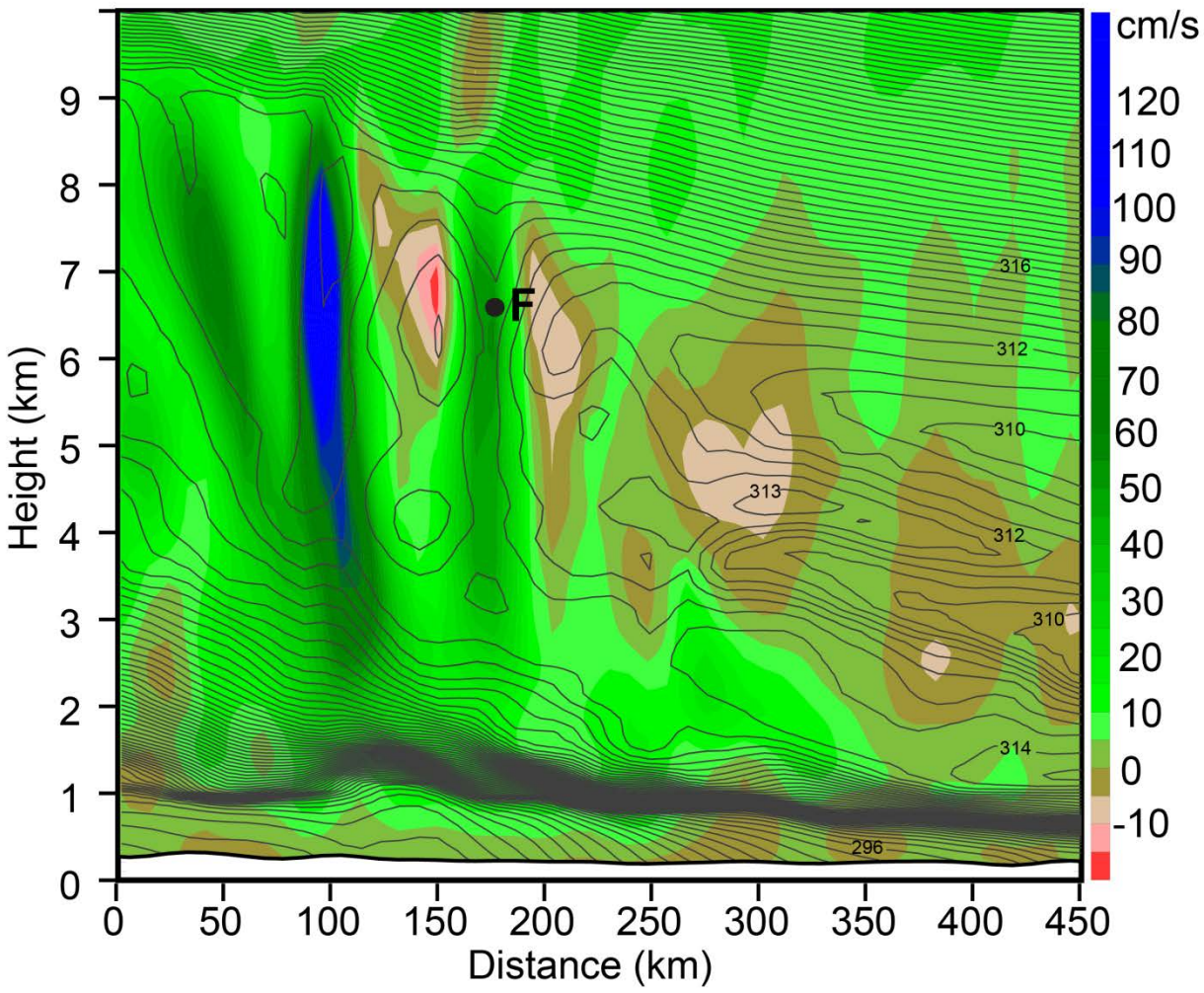

Figure 3.14: Simulated vertical velocity (colors) and equivalent potential temperature (contours) valid at 0300 UTC on 9 December 2009. Black dot is Point F, the release point for the trajectory in Figure 3.15.

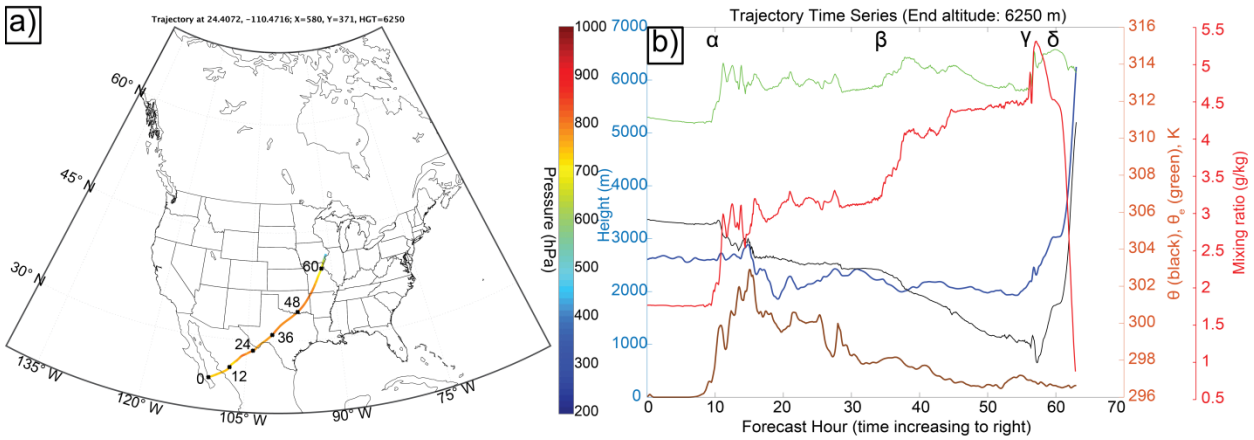

Figure 3.15: As in Figure 3.12, but for a backwards trajectory within the convective cell released at Point F in Figure 3.14.

4) Conclusions

This dissertation has presented the results of research examining the structure and distribution of convection and vertical air velocities in the comma-head region. The results of a numerical simulation were used to examine how air arrives in the comma-head and forms the layer of potential instability that allows elevated convection to form on the warm (equatorward) side of the comma-head.

Analysis of WCR data from three separate cyclones using methods presented herein shows that there are two main regions with convective vertical air motions (air motions exceeding 1 m s^{-1}). The first is in the generating cells atop the stratiform region on the poleward side of the comma-head, where widespread precipitation falls through a stable atmosphere. Atop this stable stratiform precipitation, generating cells are present with vertical air motions of 1-2 m s^{-1} and horizontal and vertical scales of 1-2 km. These generating cells were ubiquitous, observed in all three cyclones atop stratiform precipitation, and were even observed atop shallow stratiform precipitation located in the dry slot of one of the storms. Beneath the generating cells in the stable air, distributions of vertical air velocities are narrow, with about 0.5 m s^{-1} width in the distributions, consistent with an ensemble of particles falling at their terminal velocities.

On the equatorward side of the comma-head in the convective region, larger vertical velocities were measured, with one cell in the 8-9 December 2009 cyclone having velocities up to 7 m s^{-1}, and a 4 km deep region of convective vertical air velocities, both upwards and downwards. Convective cells were also present in the 2-3 December 2009 cyclone, with smaller convective vertical velocities on the order of 1-3 m s^{-1}, instead of the 1-7 m s^{-1} present in the 8-9 December 2009 convective cells. In both of these cases, the velocities measured in the 2-4 km layer beneath the elevated boundary had a spread of 0.5-0.75 m s^{-1}, which is representative of an

ensemble of particles falling at their terminal velocities through a stable layer. These elevated convective cells and the cloud-top generating cells were the only regions with convective vertical velocities in the cyclone.

The third chapter of this dissertation addressed the question of how the distribution and generation of potential instability in the comma-head region develops. A WRF simulation with convection permitting spatial and temporal resolution was described that was designed to examine this question. This simulation of the 8-9 December 2009 cyclone captured the synoptic environment adequately, and produced both potential instability, with MUCAPE values up to 93 J kg^{-1}, and elevated convection with vertical velocities in excess of 1 m s^{-1} on the equatorward side of the cyclone's comma-head, consistent with the observations presented in Chapter 2.

Trajectory analyses were presented, with backward trajectories released in regions where the model diagnosed potential instability. Cross-sections of θ_e across the simulated storm's comma-head revealed that the potentially unstable air above the frontal boundary consisted of 5 distinct layers, and these layers were consistently present on cross-sections across the region of elevated MUCAPE. These layers had air that originated in the same geographic regions regardless of the cross-sections or the time period when elevated convection was observed in the actual system. Air from the base of the unstable layer was sourced from the lower atmosphere near Baja California, while the top layer was sourced 5000 km away at high elevation in northwestern Canada.

All of the trajectories in the potentially unstable layer originated over continental Mexico, over the Pacific Ocean, or the northwestern part of Canada. Air over the Pacific in particular was important for the bottom three layers of the potential instability. Notably absent from the

potentially unstable layer was air from the Gulf of Mexico or over the central Plains. This air was confined to the stable layer below the elevated frontal boundary.

The trajectories showed a consistent behavior where both θ and θ_e decreased at a rate of 1 to 2 K per day outside of mountainous regions or cloudy regions. This behavior is consistent with the rate of cooling in the atmosphere due to longwave radiational cooling. Air was not found to move along adiabatic surfaces in the atmosphere, but rather cooled with time, absent other diabatic effects. The thermodynamic properties of air along trajectories also were significantly impacted by topography, altering the θ and θ_e value of parcels, either through mechanical lifting near the terrain level or turbulent mixing aloft.

The production of potential instability was done associated with the initial thermodynamic properties of air in one source region, but rather by the juxtaposition of air from vastly different sources into a potentially unstable layer. In the process of arriving at the comma-head region, air underwent diabatic changes to thermodynamic properties. Once the air arrived in the comma-head region and combined to produce a potentially unstable profile, convective cells formed. These cells had measured updrafts of more than 1 m s^{-1} and transported air from the base to the top of the potentially unstable layer.

Future research building on the work presented here should expand the number of cyclones analyzed to test the robustness of the results, both from the radar observations of vertical velocities and the modeling of potential instability.

References

American Meteorological Society, cited 2013: "Alberta clipper." Glossary of Meteorology. [Available online at http://glossary.ametsoc.org/wiki/Alberta_clipper]

American Meteorological Society, cited 2013: "generating cell." Glossary of Meteorology. [Available online at http://glossary.ametsoc.org/wiki/generating_cell]

Benjamin, S. G., Brian D. Jamison, William R. Moninger, Susan R. Sahm, Barry E. Schwartz, Thomas W. Schlatter, 2010: Relative short-range forecast impact from aircraft, profiler, radiosonde, VAD, GPS-PW, METAR, and mesonet observations via the RUC hourly assimilation cycle. *Mon. Wea. Rev.*, **138**, 1319–1343.

Bergeron, T., 1950: Über der mechanismum der ausgeibigen Niederschläge. *Ber. Dtsch. Wettterdienstes*, **12**, 225-232.

Bjerknes, V. F. (1910), Synoptical representation of atmospheric motions. *Quart. J. Roy. Meteor. Soc.*, **36**: 267–286

Brown, S. R., 1970: Terminal velocities of ice crystals. *Colorado State University Atm. Sci. Paper 170*.

Browning, K. A., Hardman, M. E., Harrold, T. W. and Pardoe, C. W. (1973), The structure of rainbands within a mid-latitude depression. *Quart. J. Roy. Meteor. Soc.*, **99**, 215–231.

Browning, K.A., 1983: Air motion and precipitation growth in a major snowstorm. *Quart. J. Roy. Met. Soc*., **109**, 225-242.

Browning, K. A., 2005: Observational synthesis of mesoscale structures within an explosively developing cyclone. *Quart. J. Roy. Meteor. Soc.*, **131**, 603-623.

Carbone, R., and A.R. Bohne, 1975: Cellular snow generation—a doppler radar study. *J. Atmos. Sci.*, **32**, 1384–1394.

Carlson, T. N. 1980: Airflow through midlatitude cyclones and the comma cloud pattern. *Mon. Wea. Rev.*, **108**, 1498–1509

Cavallo, S. M., J. Dudhia, and C. Snyder, 2010: A Multilayer Upper-Boundary Condition for Longwave Radiative Flux to Correct Temperature Biases in a Mesoscale Model. *Mon. Wea. Rev.*, **139**, 1952-1959

Colman, B. R., 1990: Thunderstorms above frontal surfaces in environments without positive CAPE. Part I: A climatology. *Mon. Wea. Rev.*, **118**, 1103–1121.

Cronce M., R. M. Rauber, K. R. Knupp, B. F. Jewett, J. T. Walters, and D. Phillips, 2007: Vertical motions in precipitation bands in three winter cyclones, *J. Appl. Meteor. and Clim.*, **46**, 1523-1543.

Cunningham, J. G. and S. E. Yuter, 2013: Atmospheric characteristics of cool-season intermittent precipitation near Portland, Oregon. *Mon. Wea. Rev.*, Mon. Wea. Rev., **142**, 1738–1757

Curran, J. T., and A. D. Pearson, 1971: Proximity soundings for thunderstorms with snow. Preprints, *Seventh Conf. on Severe Local Storms*, Kansas City, MO, Amer. Meteor. Soc., 118–119.

Davis, C. I., 1974: The ice nucleating characteristics of various AgI aerosols. Ph.D. diss, Univ. of Wyoming.

Douglas, R. H., K. L. S. Gunn, J. S. Marshall, 1957: Pattern in the vertical of snow generation. *J. Meteor*., **14**, 95–114.

Draxler, R.R., and G.D. Hess, 1998: An overview of the HYSPLIT_4 modeling system of trajectories, dispersion, and deposition. *Aust. Meteor. Mag.*, **47**, 295-308.

Fuhrmann, C. M. and C. E. Konrad II, 2013: A trajectory approach to analyzing the ingredients associated with heavy winter storms in central North Carolina. *Wea. Forecasting*, **28**, 647–667

Grim, J. A., R. M. Rauber, M. K. Ramamurthy, B. F. Jewett and M. Han, 2007: High resolution observations of the trowal/warm frontal region of two continental winter cyclones *Mon. Wea. Rev*., **135**, 1629–1646.

Gunn, K. L. S., M. P. Langleben, A. S. Dennis, B. A. Power, 1954: Radar evidence of a generating level for snow. *J. Meteor*., **11**, 20–26.

Halcomb, C.E., and P.S. Market, 2003. Forcing, instability, and equivalent potential vorticity in a Midwestern U.S. convective snowstorm. *Meteor. Apps*. , **10** , 273- 280.

Han, M., R. M. Rauber, M. K. Ramamurthy, B. F. Jewett and J. A. Grim, 2007: Mesoscale dynamics of the trowal and warm frontal regions of two continental winter cyclones. *Mon. Wea. Rev*., **135**, 1647–1670.

Herzegh P. H., and P. V. Hobbs, 1980: The mesoscale and microscale structure and organization of clouds and precipitation in midlatitude cyclones. II: warm frontal clouds. *J. Atmos. Sci*., **37**, 597-611.

Hobbs, P.V., and J.D. Locatelli, 1978: Rainbands, precipitation cores and generating cells in a cyclonic storm. *J. Atmos. Sci.*, **35**, 230–241.

Holle, R. L., and J. V. Cortinas Jr., 1998: Thunderstorms observed at surface temperatures near and below freezing across North America. Preprints, *19th Conf. on Severe Local Storms,* Minneapolis, MN, Amer. Meteor. Soc., 705–708.

Houze, R. A., Jr., S. A. Rutledge, T. J. Matejka, and P. V. Hobbs, 1981: The mesoscale and microscale structure and organization of clouds and precipitation in midlatitude cyclones. III: Air motions and precipitation growth in a warm frontal rainband. *J. Atmos. Sci*., **38**, 639-649.

Hunter, S. M., S. J. Underwood, R. L. Holle, and T. L. Mote, 2001: Winter lightning and heavy frozen precipitation in the southeast United States. *Wea. Forecasting*, **16**, 478–490.

Iacono, M.J., Mlawer, E.J., Clough, S.A. and Morcrette, J., 2000. Impact of an improved longwave radiation model, RRTM, on the energy budget and thermodynamic properties of the NCAR community climate model, CCM3. *Journal of Geophysical Research 105*

Jackson, R.C., G.M. McFarquhar, J. Stith, M. Beals, J. Jensen, W.A. Cooper, R. Shaw, J. Fugal, and A. Korolev, 2014: An assessment of the impact of shattered artifacts and artifact removal techniques for 2D cloud probe data. *J. Atmos. Ocean. Tech.*, in press.

Kajikawa, M., 1972: Measurement of falling velocity of individual snow crystals. *J. Met. Soc. Japan*, **50**, 577-584.

Kain, J. S., and J. M. Fritsch, 1990: A one-dimensional entraining/detraining plume model and its application in convective parameterization. *J. Atmos. Sci*., **47**, 2784–2802.

Keeler, J. M., B. F. Jewett, R. M. Rauber, G. M. McFarquhar, R. M. Rasmussen, L. Xue, C. Liu, and G. Thompson, 2016a: Dynamics of cloud-top generating cells in winter cyclones. Part I: idealized simulations in the context of field observations. *J. Atmos. Sci.*, **73**, 1507–1527.

Langleben, M. P., 1956: The plan pattern of snow echoes at the generating level. *J. Meteor.*, **13**, 554–560.

Leon, D., G. Vali, M. Lothon, 2006: Dual-doppler analysis in a single plane from an airborne platform. *J. Atmos. Oceanic Technol.*, **23**, 3–22.

Locatelli, J. D., and P. V. Hobbs, 1974: Fallspeeds and masses of solid precipitation particles. *J. Geophys. Res.*, **79,** 2185–2197.

Marshall, J.S., 1953: Precipitation trajectories and patterns. *J. Atmos. Sci*., **10**, 25–29.

Martin, J. E., 1998b: The structure and evolution of a continental winter cyclone. Part II: Frontal forcing of an extreme snow event. *Mon Wea. Rev*., **126**, 329-348.

Market, P. S., C. E. Halcomb, and R. L. Ebert, 2002: A climatology of thundersnow events over the contiguous United States. *Wea. Forecasting*, **17**, 1290–1295.

Market, P. S., K. Crandall, and R. Rauber, 2012: High-resolution rawinsonde observations of the cold-sector precipitation regions in transient mid-latitude extratropical cyclones. *Natl. Wea. Dig.*, **36**, 3–8

Moore, J. T., and P. D. Blakley, 1988: The role of frontogenetical forcing and conditional symmetric instability in the Midwest snowstorm of 30–31 January 1982. *Mon. Wea. Rev.*, **116**, 2155–2171.

Moore, J. T., C. E. Graves, S. Ng, and J. L. Smith, 2005: A Process-Oriented Methodology Toward Understanding the Organization of an Extensive Mesoscale Snowband: A Diagnostic Case Study of 4–5 December 1999. Wea. Forecasting, **20**, 35–50

Nicosia, D. J., and R. H. Grumm, 1999: Mesoscale band formation in three major northeastern United States snowstorms. *Wea. Forecasting*, **14**, 346-368.

Novak, D. R., Brian A. Colle, Sandra E. Yuter, 2008: High-resolution observations and model simulations of the life cycle of an intense mesoscale snowband over the northeastern United States. *Mon. Wea. Rev.*, **136**, 1433–1456.

Novak, D. R., B. A. Colle, and R. McTaggart-Cowan, 2009: The role of moist processes in the formation and evolution of mesoscale snowbands within the comma head of northeast U.S. cyclones. Mon. Wea. Rev., **137**, 2662–2686.

Novak, D. R., B. A. Colle, and A. R. Aiyyer, 2010: Evolution of mesoscale precipitation band environments within the comma head of northeast U.S. cyclones. Mon. Wea. Rev., **138**, 2354–2374.

Pfahl, S., Madonna, E., Boettcher, M., Joos, H., and Wernli, H. 2014: Warm conveyor belts in the ERA-Interim data set (1979–2010). Part II: Moisture origin and relevance for precipitation, *J. Climate*, 27, 27–40.

Rosenow, A. R., D. M. Plummer, R. M. Rauber, G. M. McFarquhar, B. F. Jewett, D. Leon, and J. M. Keeler, 2014: Vertical motions within generating cells and elevated convection in the comma head of winter cyclones. *J. Atmos. Sci.*, **71**, 1538–1558. ©American Meteorological Society. Used with permission.

Rasp, S., T. Selz, and G. C. Craig, 2016: Convective and slantwise trajectory ascent in convection-permitting simulations of midlatitude cyclones. *Mon. Wea. Rev*., **144**, 3961–3976

Rauber, R. M., J. Wegman, D. M. Plummer, A. A. Rosenow, M. Peterson, G. M. McFarquhar, B. F. Jewett, D. Leon, P. S. Market, K. R. Knupp, J. M. Keeler, and S. Battaglia, 2014: Stability and charging characteristics of the comma head region of continental winter cyclones. *J. Atmos. Sci., J. Atmos. Sci.*, **71**, 1559–1582.

Rauber R. M., D. M. Plummer, M. K. Macomber, A. A. Rosenow, G. M. McFarquhar, B. F. Jewett, D. Leon, N. Owens, and J. M. Keeler, 2015: The Role of Cloud-Top Generating Cells and Boundary Layer Circulations in the Finescale Radar Structure of a Winter Cyclone over the Great Lakes. *Mon. Wea. Rev*., **143**, 2291–2318.

Reed, R. J., 1955: A study of a characteristic type of upper-level frontogenesis. *J. Meteor*., **12**, 226 – 237.

Reed, R. J., and F. Sanders, 1953: An investigation of the development of a mid-tropospheric frontal zone and its associated vorticity field. *J. Meteor*., **10**, 338-349.

Rutledge S. A., and P. V. Hobbs, 1983: The mesoscale and microscale structure and organization of clouds and precipitation in midlatitude cyclones. A model for the seeder-feeder process in warm frontal rainbands. *J. Atmos. Sci.*, **40**, 1185-1206.

Schultz, D. M., and C. F. Mass, 1993: The Occlusion Process in a Midlatitude Cyclone over Land. Mon. Wea. Rev., 121, 918–940

Schultz, D. M. 2001: Reexamining the cold conveyor belt. *Mon. Wea. Rev*., **129**, 2205–2225.

Sienkiewicz, J. M., J. D. Locatelli, P. V. Hobbs, and B. Geerts, 1989: Organization and structure of clouds and precipitation on the mid-Atlantic coast of the United States. Part II: The mesoscale and microscale structures of some frontal rainbands. *J. Atmos. Sci*., **46**, 1349-1364.

Skamarock, W. C., and Coauthors, 2008: *A Description of the Advanced Research WRF Version 3*. NCAR Technical Note NCAR/TN-475+STR

Stark, D., B. A. Colle, and S. E. Yuter, 2013: Observed microphysical evolution for two east coast winter storms and the associated snow bands. *Mon. Wea. Rev.*, **141**, 2037-2057.

Stoelinga, M. T., 2009: A users' guide to RIP version 4.5: A program for visualizing mesoscale model output. [Available online at http://www.mmm.ucar.edu/wrf/users/docs/ripug.htm.]

Syrett, W.J., B.A. Albrecht, and E.E. Clothiaux, 1995: Vertical cloud structure in a midlatitude cyclone from a 94-GHz Radar. *Mon. Wea. Rev.*, **123**, 3393–3407.

Thompson, G., P. R. Field, R. M. Rasmussen, and W. D. Hall, 2008: Explicit forecasts of winter precipitation using an improved bulk microphysics scheme. Part II: implementation of a new snow parameterization. *Mon. Wea. Rev.*, **136**, 5095–5115

Uccellini, L. W., 1976: Operational diagnostic applications of isentropic analysis. *Natl. Wea. Dig.*, **1**, 4-12

Wang Z., J. French, G. Vali, P. Wechsler, S. Haimov, A. Rodi, M. Deng, D. Leon, J. Snider, and L. Peng and A. L. Pazmany, 2012: Single aircraft integration of remote sensing and in-situ sampling for the study of cloud microphysics and dynamics. *Bull. Amer. Meteor. Soc.*, **93**, 653-668.

Wernli, B. H. and Davies, H. C. (1997), A lagrangian-based analysis of extratropical cyclones. I: The method and some applications. *Quart. J. Roy. Meteor. Soc.*, **123**: 467–489.

Wexler, R., 1955: Radar analysis of precipitation streamers observed 25 February 1954. *J. Atmos. Sci.*, **12**, 391–393.

Wexler, R., and D. Atlas, 1959: Precipitation generating cells. *J. Atmos. Sci.*, **16**, 327–332

Wiesmueller, J. L.,and S. M. Zubrick, 1998: Evaluation and application of conditional symmetric instability, equivalent potential vorticity, and frontogenetic forcing in an operational forecast environment. *Wea. Forecasting*, **13**, 84–101.

Yuter, S. E., and R. A. Houze, 1995: Three-dimensional kinematic and microphysical evolution of Florida cumulonimbus. Part II: frequency distributions of vertical velocity, reflectivity, and differential reflectivity. *Mon. Wea. Rev.*, **123**, 1941–1963.

Zishka, K. M., P. J. Smith, 1980: The climatology of cyclones and anticyclones over North America and surrounding ocean environs for January and July, 1950–77. *Mon. Wea. Rev.*, **108**, 387–401.